• Nanostructures for few molecules detection and characterization

www.polito.it

enzo.difabrizio@polito.it

Pavia January 18th 2024 Seminar at San Matteo

Let me first thank people at PoliTo Group and collaborators

Tania Limongi

Bruno Torre

Monica Marini

Marco Allione

Francesca Legittimo

Francesca Suso

Fabrizio Pirri

Carlo Ricciardi

Laura Fabris

Elena Simone

Research lines

The essence of Nanostructure research

design, fabricate, measure and apply nano inspired structures and devices for developing methods and techniques for interdisciplinary problems

Delivering of energy at Nanoscale

Single molecule study & detection

Novel methods & devices for cellomics

Imaging, scaffolding, cancer study

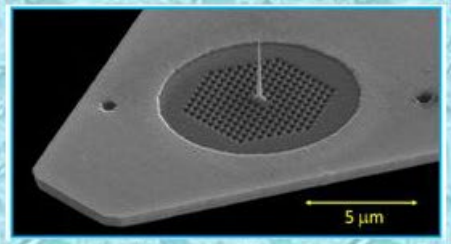

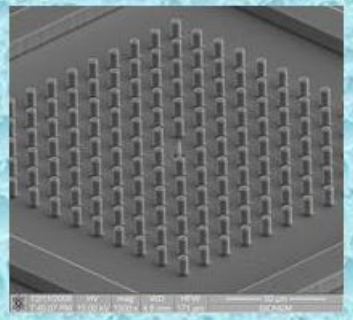

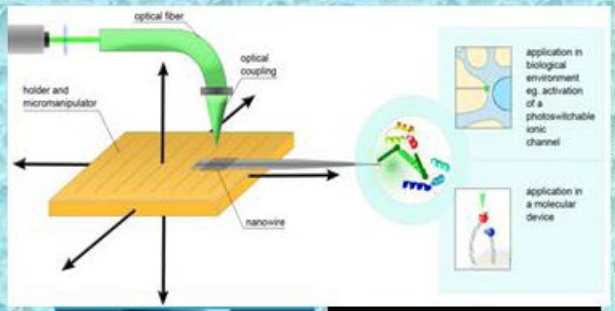

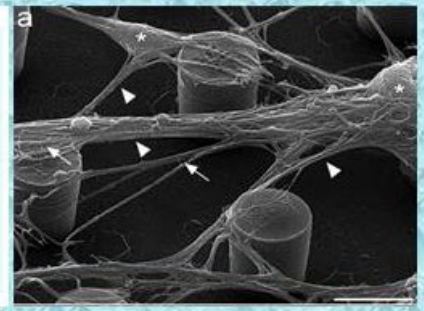

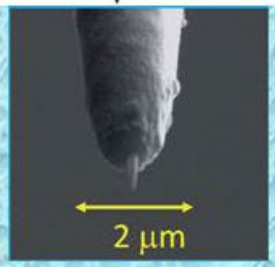

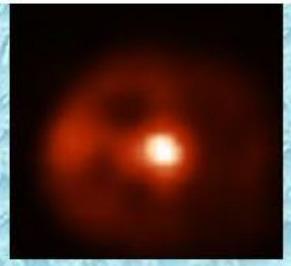

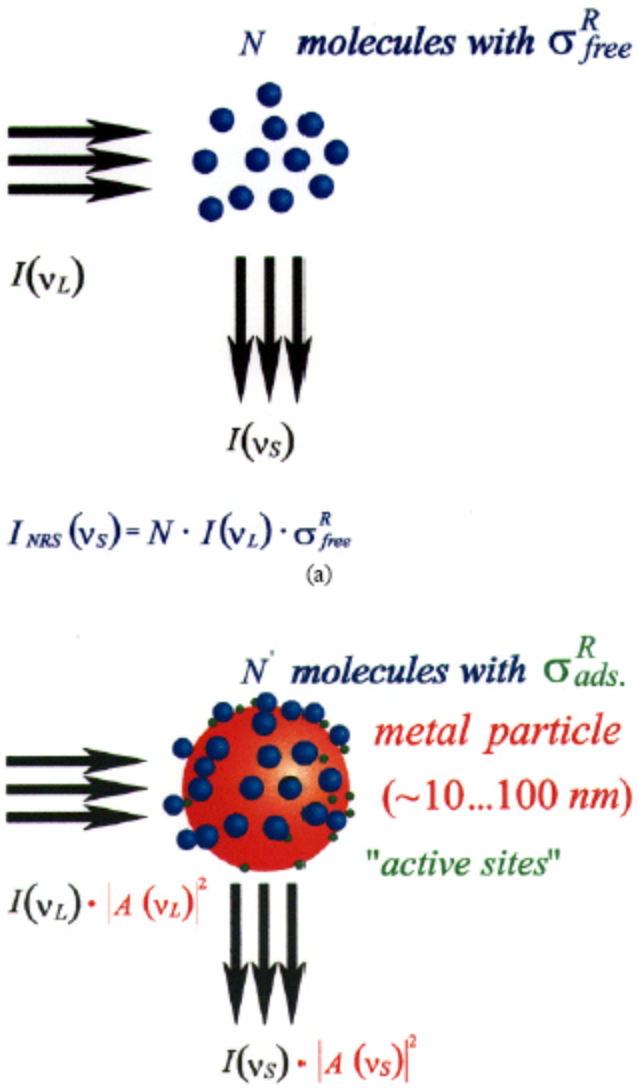

Figure 1. Comparison of 'normal' (a) and surface-enhanced (b) Raman scattering (for an explanation see text).

SERS and nanoparticles

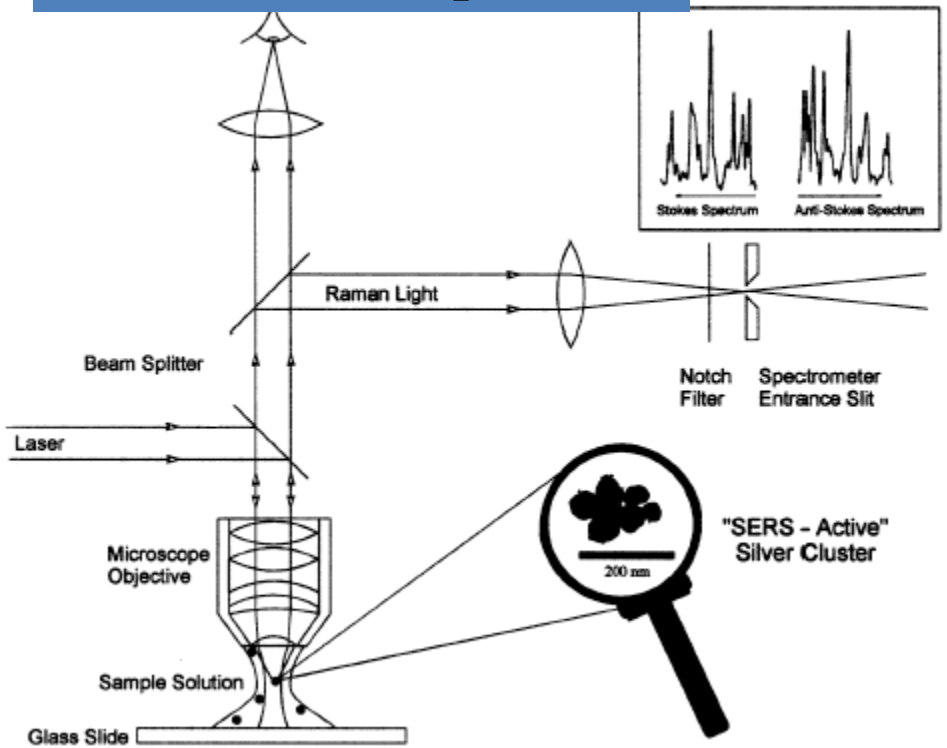

Local field depends mainly on:

1) The size and shape of metal nanoparticles (about $\lambda/10$)
1) The distance between metal nanoparticles (about $\lambda/100$)

(Both difficult to control with colloidal nanoparticle)

Adiabatic Nanofocusing : Tapered Nanoplasmonic Waveguides

Optic limit $\Delta x = 0.61\lambda/NA$ **electromagnetic nature** of the energy carrier medium, (photon).
Plasmonic limit $SPP_{SkinDepth}$ **electromechanical nature** of the energy carrier medium, (SPP).

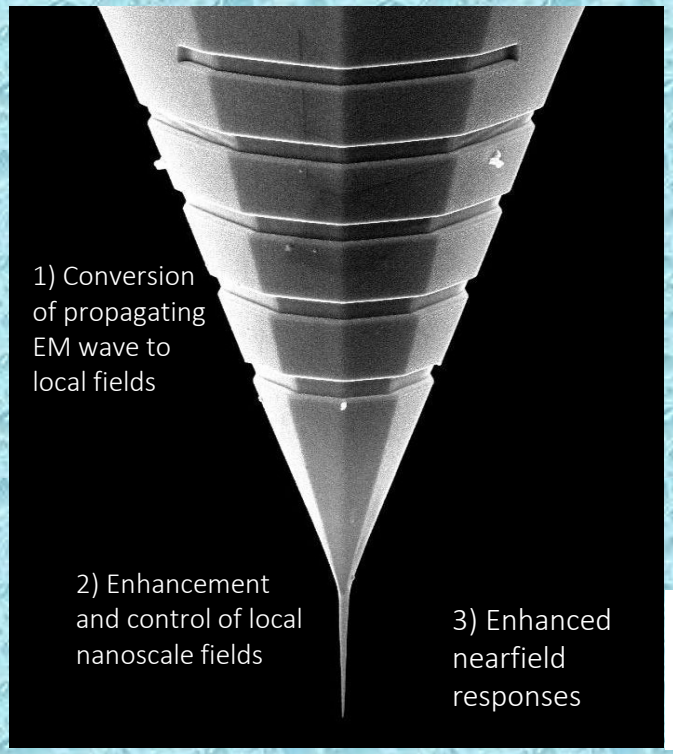

Mark Stockman, *Nanofocusing of Optical Energy in Tapered Plasmonic Waveguides* PRL , Vol.93, 137404, (**2004**)

F. De Angelis et al., Nanoscale chemical mapping using three-dimensional adiabatic compression of surface plasmon polaritons, Nat. Nanotech, 5, 67-72 (**2010**)

L. Novotny *et al.*, *NearField Optical Microscopy and Spectroscopy with Pointed Probes*, Annual Rev. Phys. Chem. 57, 303-331 (**2006**)

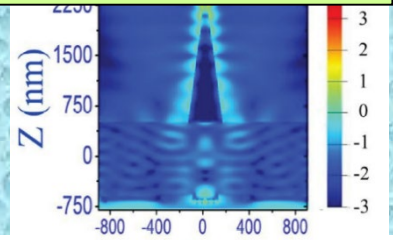

$$n(R) \approx \frac{1}{k_0 R}\sqrt{-\frac{2\varepsilon_d}{\varepsilon_m}}\left[\ln\sqrt{-\frac{4\varepsilon_m}{\varepsilon_d}} - \gamma\right]^{-1},$$

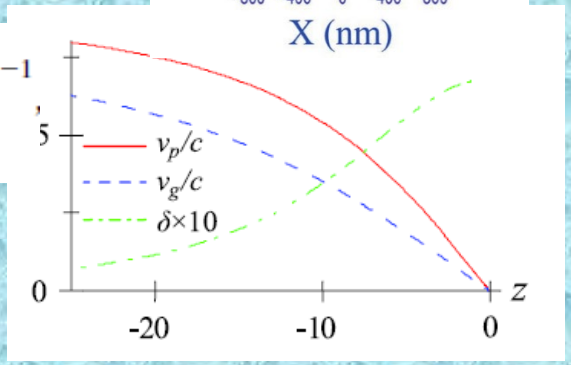

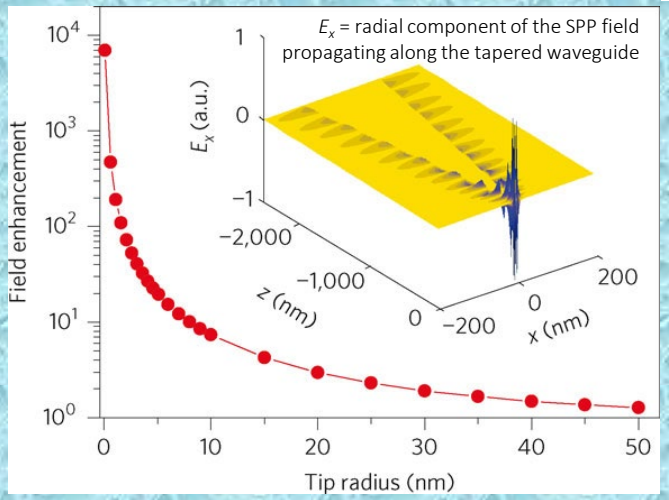

Notice also that $\boldsymbol{k}=n\boldsymbol{k}_0$

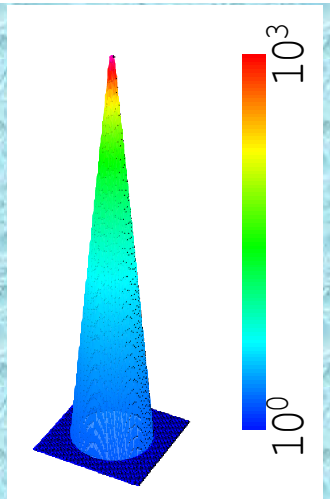

Phase velocity of SPP

Group velocity of SPP

Adiabatic parameter (scaled by 10)

SPP adiabatic compression simulation of plasmon polariton

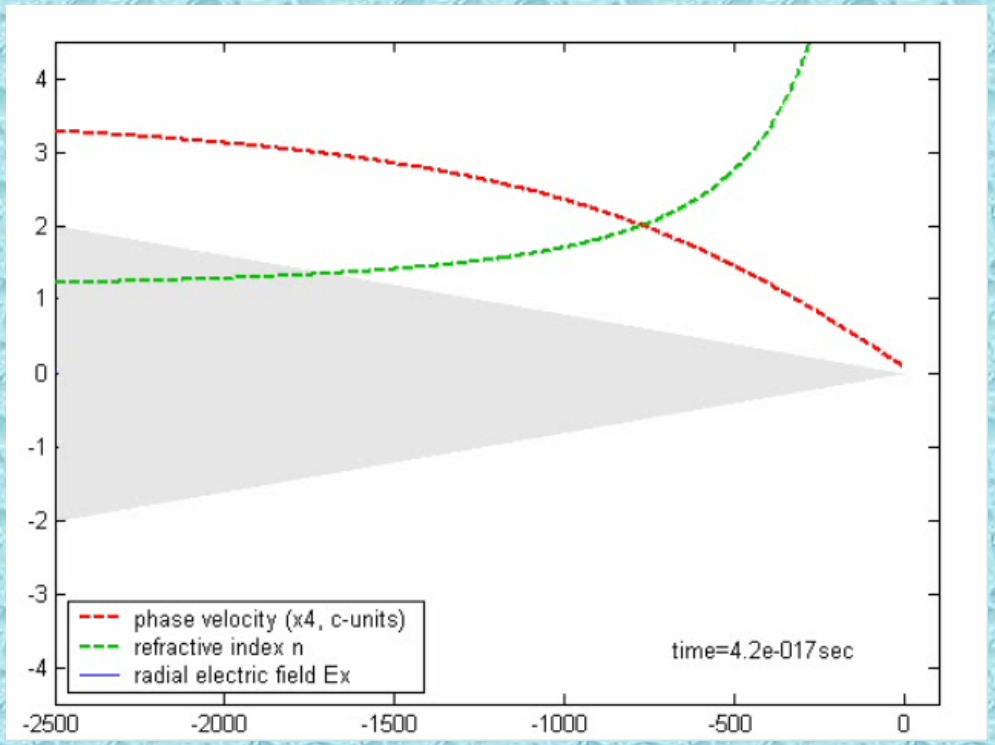

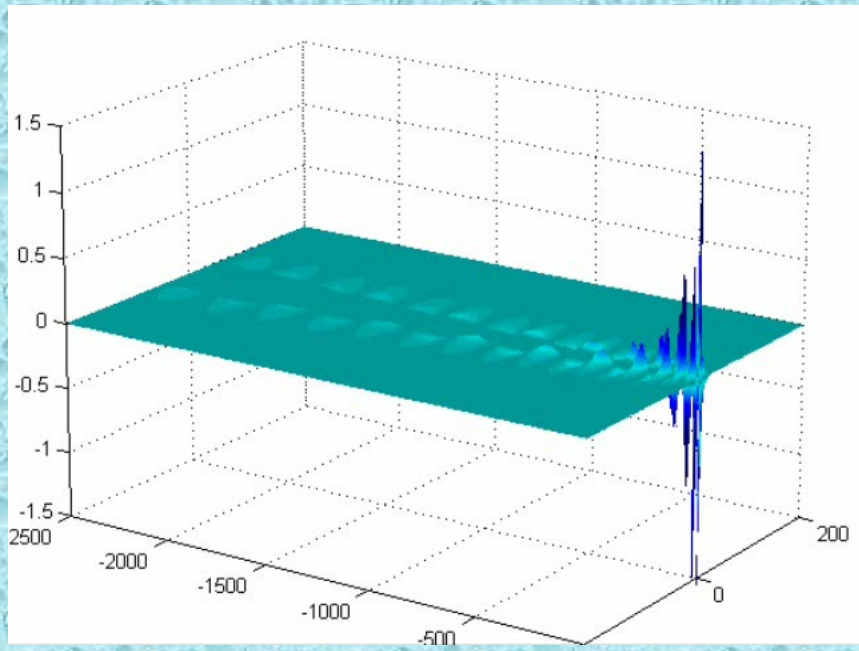

SPP conversion to hot electrons

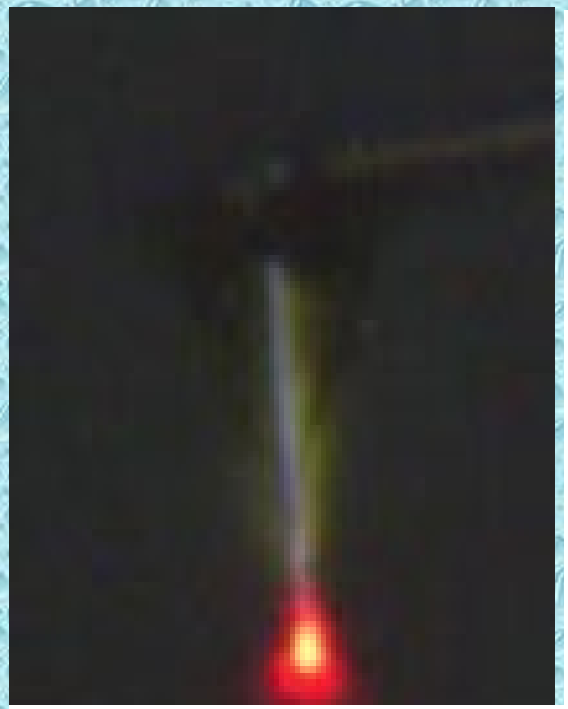

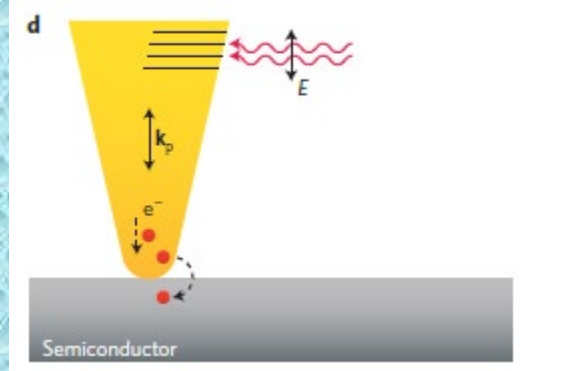

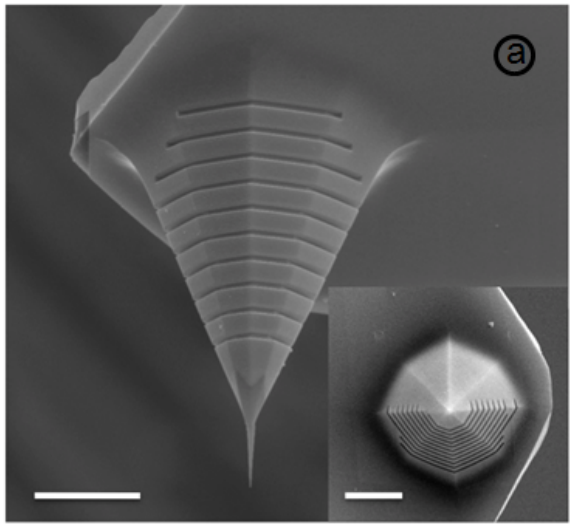

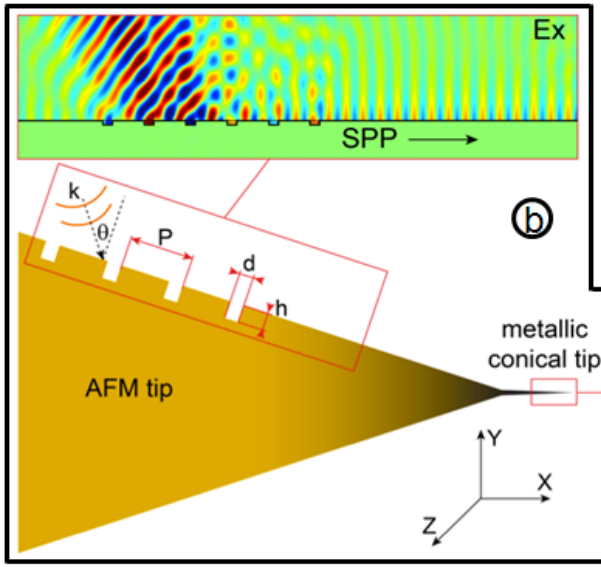

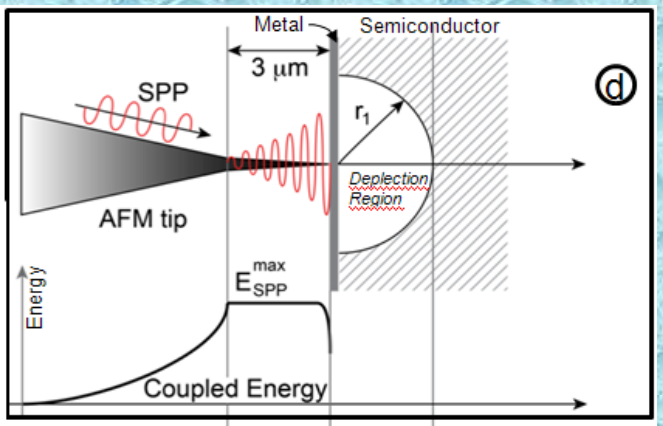

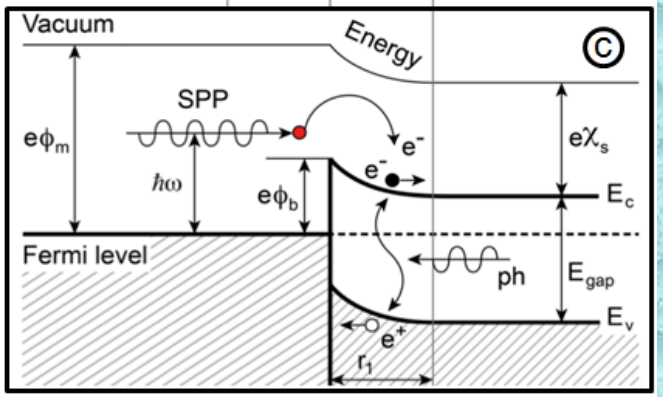

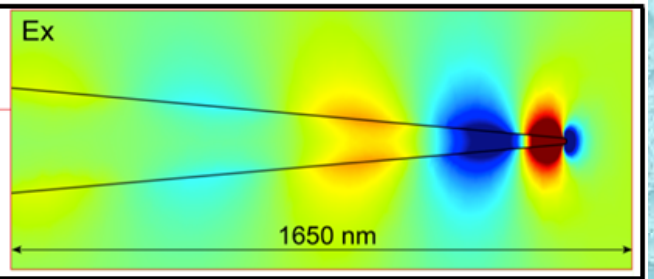

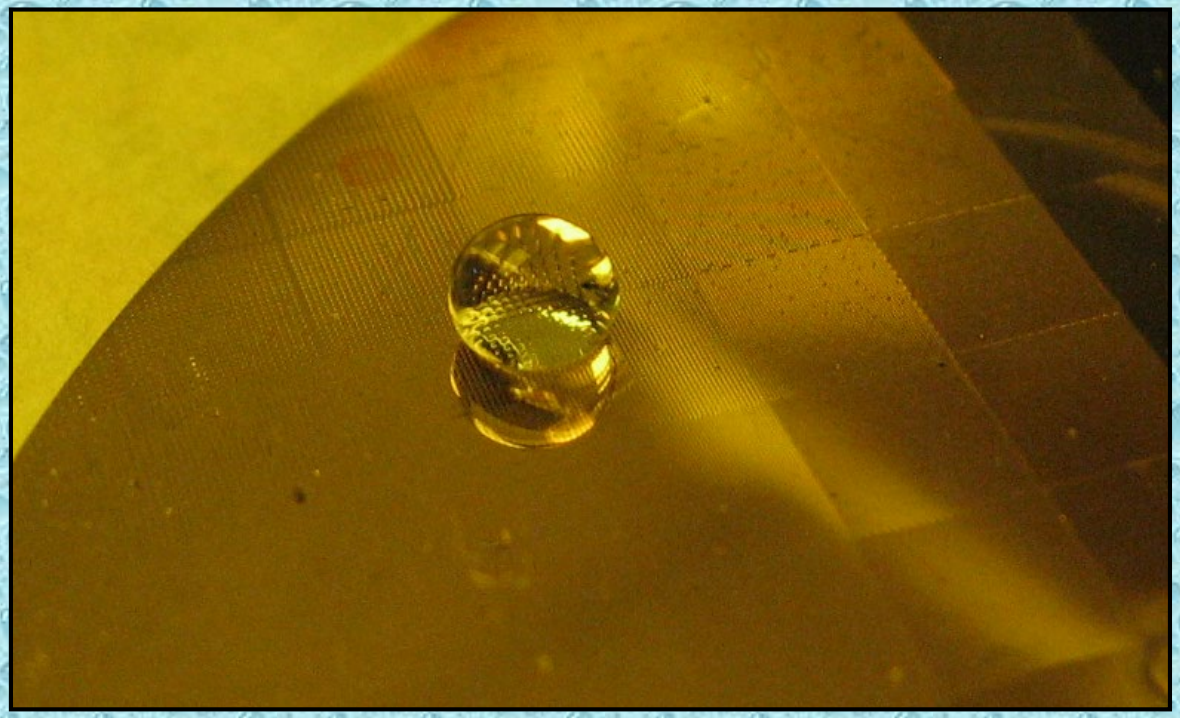

SuperHydrophobic Surfaces
Biomedical Applications

Diffusion limits

NANO LETTERS

2005
Vol. 5, No. 4
803−807

Detection Limits for Nanoscale Biosensors

Paul E. Sheehan* and Lloyd J. Whitman

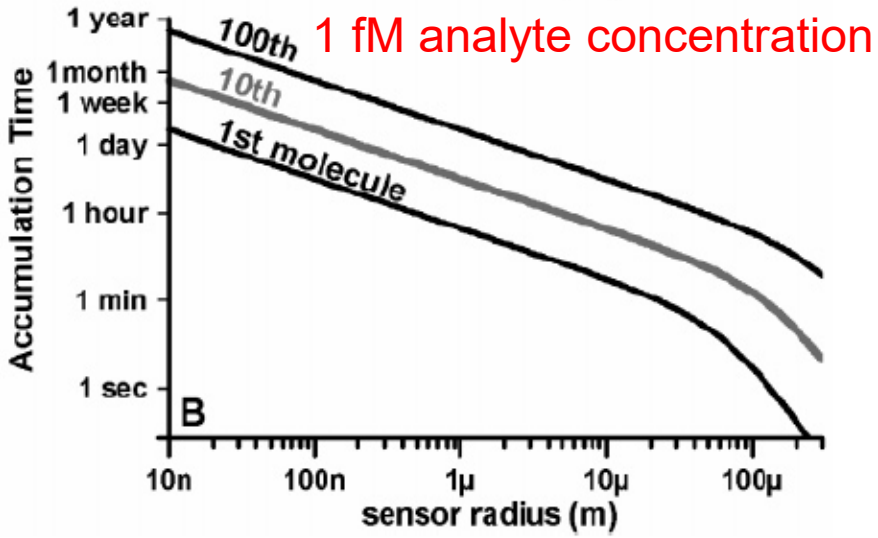

Figure 1. (A) Time required to accumulate one or 10 analyte molecules via static diffusion onto a 200 μm-diameter hemisphere for a diffusion constant of 150 $\mu m^2\ s^{-1}$, characteristic of single-stranded DNA approximately 20 bases long. After one minute, a few molecules can be expected on the sensor for a sample concentration of 1 fM. The inset shows the sensor geometry. (B) Time required for this sensor to accumulate 1, 10, and 100 molecules when submerged in a semi-infinite 1 fM solution. For radii smaller than 10 μm the required time varies linearly with the radius.

The lotus effect

Natural systems

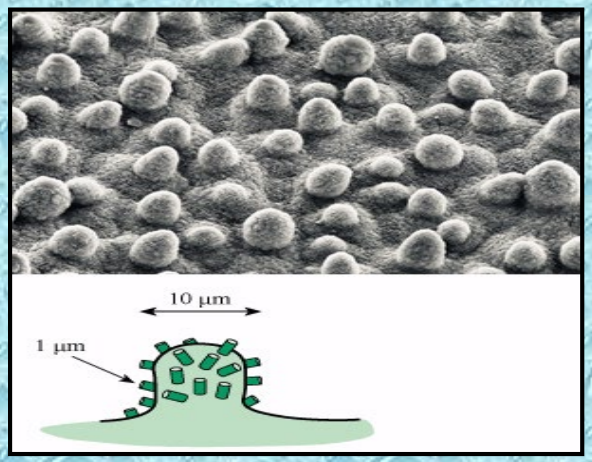

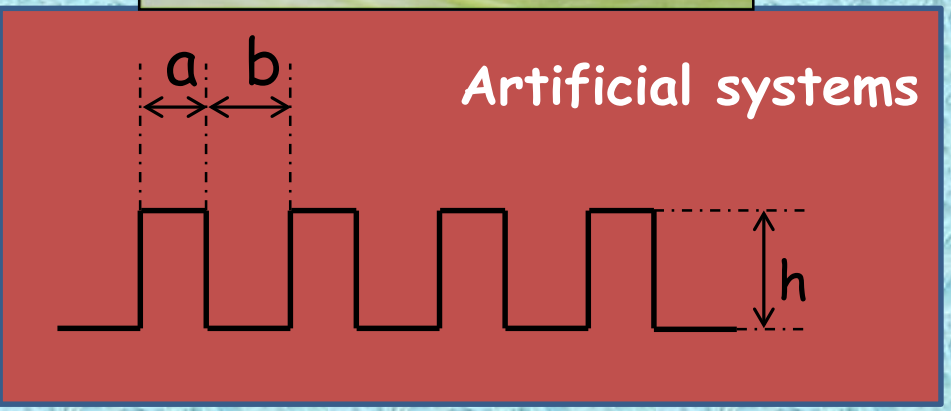

Artificial systems

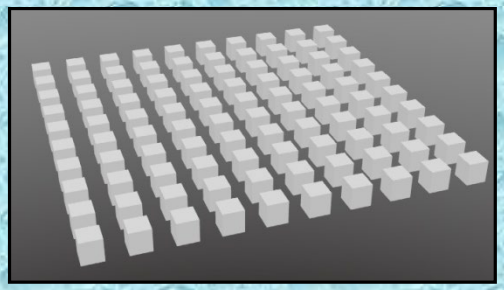

Total surface area to total projectet surface area

$$r = \frac{4ah + (a+b)^2}{(a+b)^2}$$

Total pillar surface area to total projectet surface area

$$\Phi = \frac{a^2}{(a+b)^2}$$

can we avoid the diffiusion limit?
SuperHydrophobicity for analyte Concentration

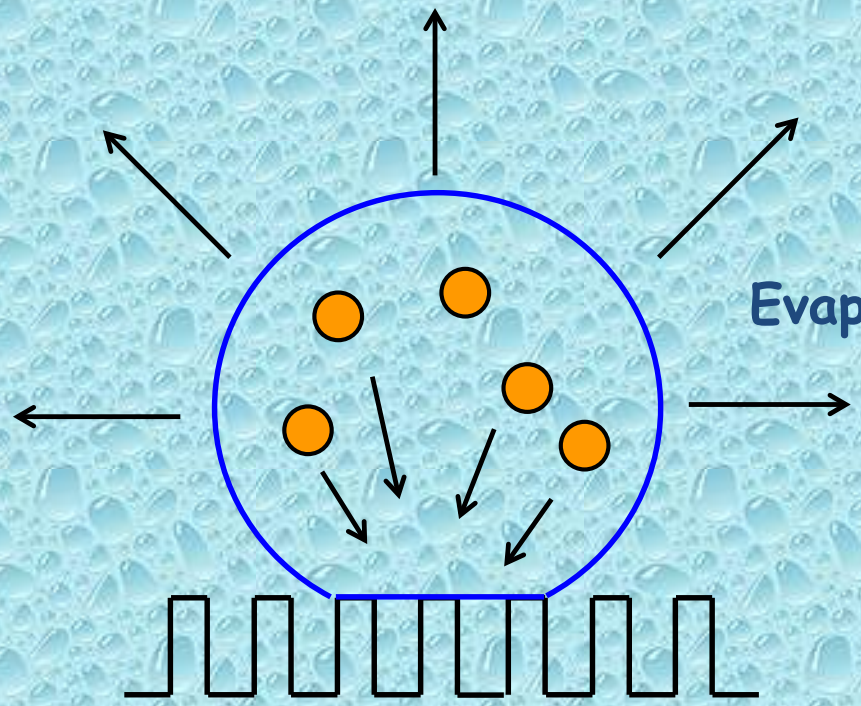

Evaporation concentration and localization

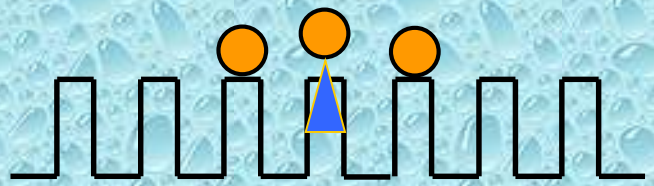

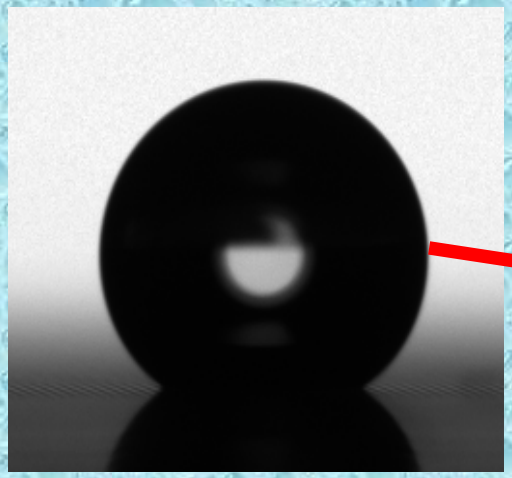

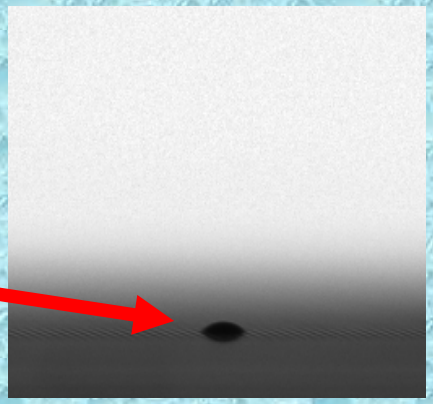

Artificial lotus effect: micropatterned surface

Photolithography combined with Deep RIE

- Full controllable size
- High aspect ratio (up to 20 or more)
- Both rigid and flexible substrates

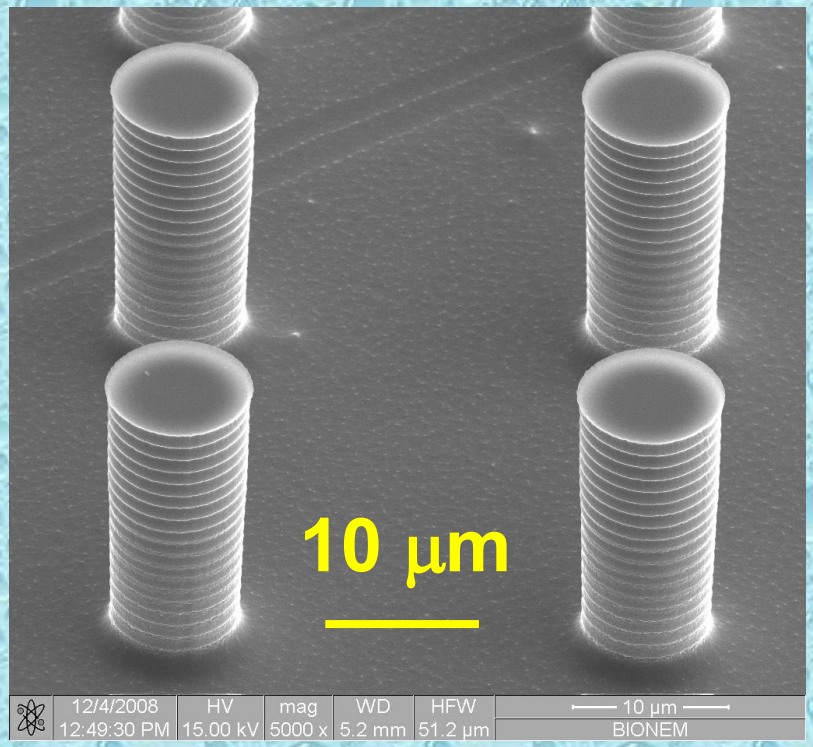

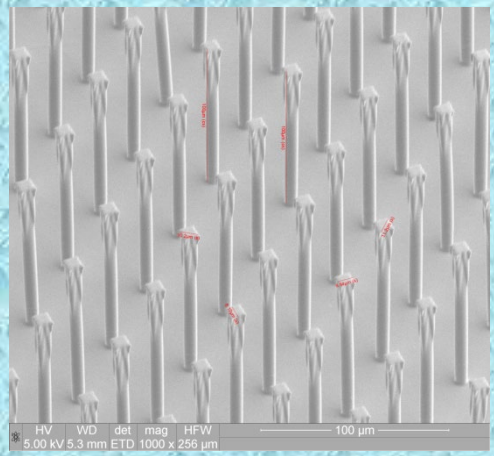

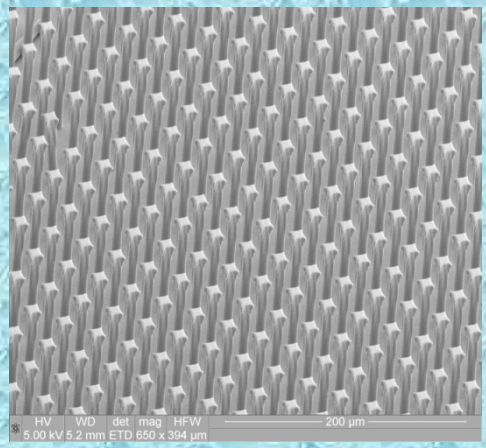

Non periodic patterning of SHSs

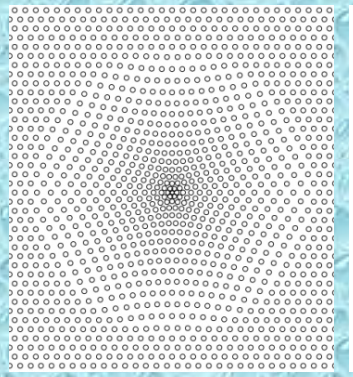

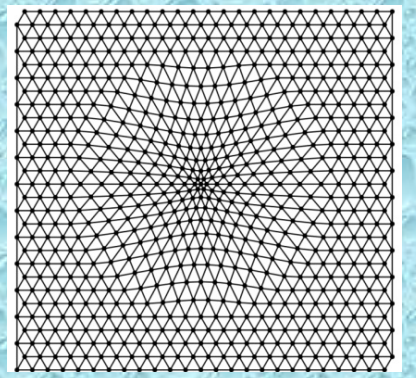

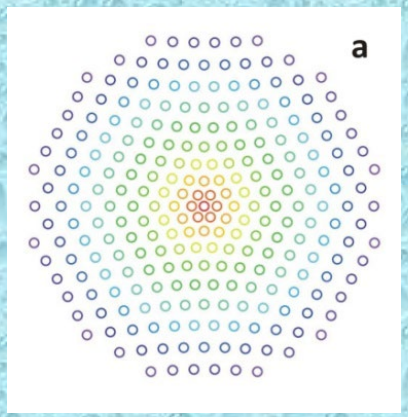

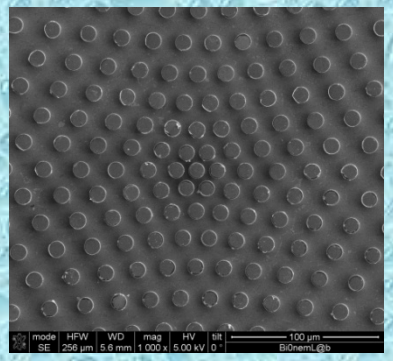

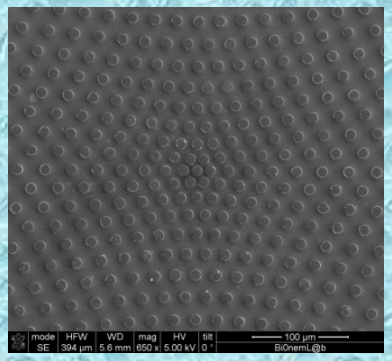

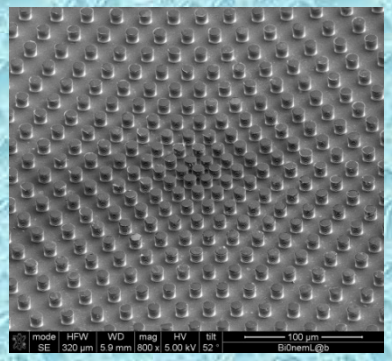

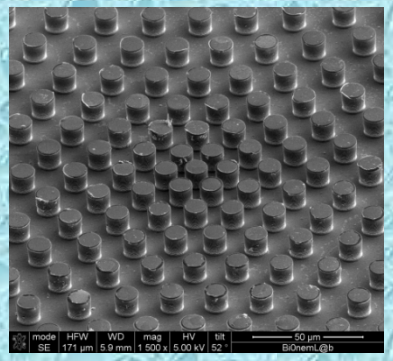

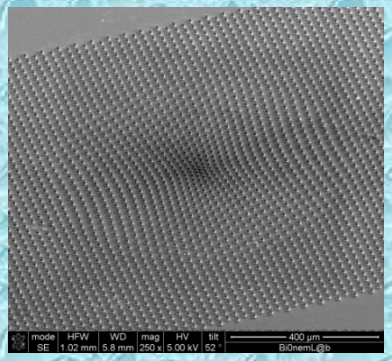

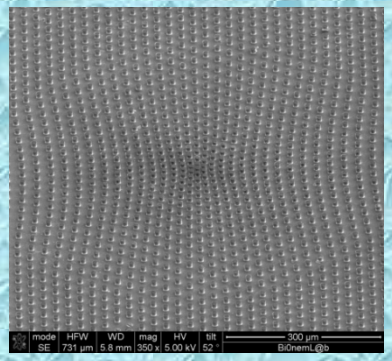

Gradients of wettability can be artificially introduced in the pattern of pillars

This is practically done realizing a **non-periodic array of micropillars**, that is, a distribution where the pitch p between the pillars is not constant, and it would instead smoothly make a transition from an external region, where p is large, to an inner region, where p is small

A non uniform profile of pillars can be obtained using a mathematical operation called contraction

Different geometries of superhydrophobic substrates

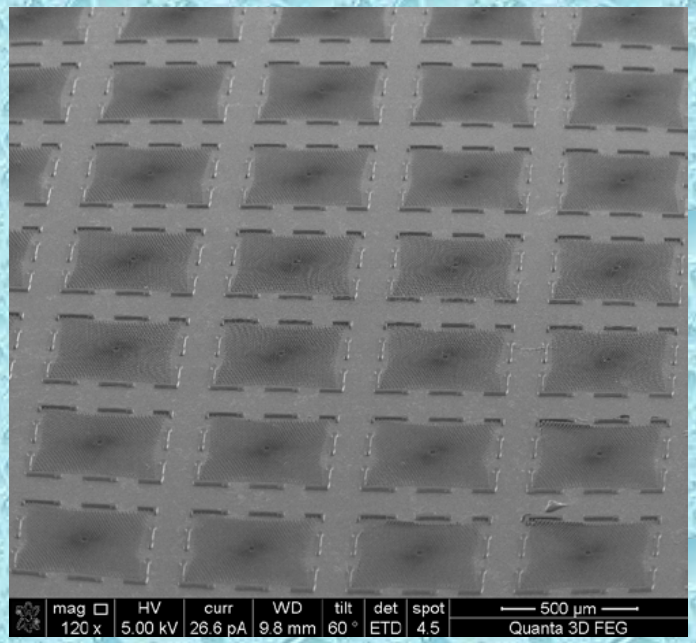

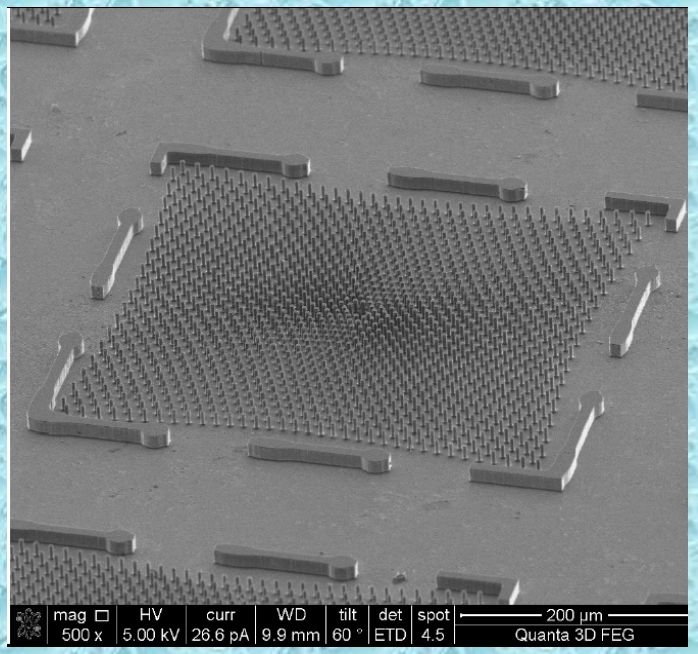

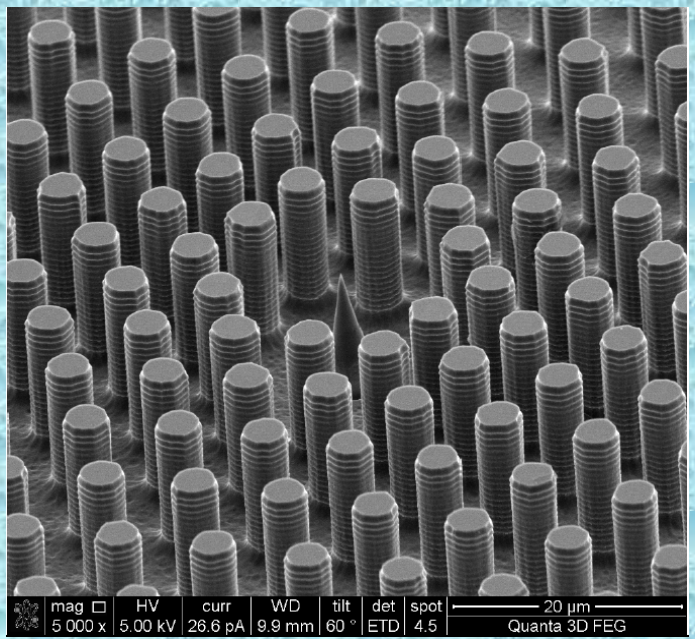

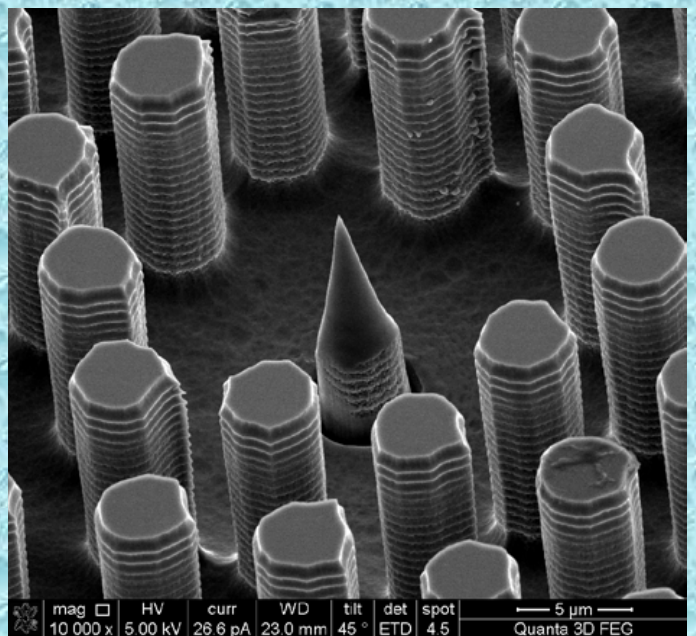

Different geometries of superhydrophobic substrates for TEM investigation

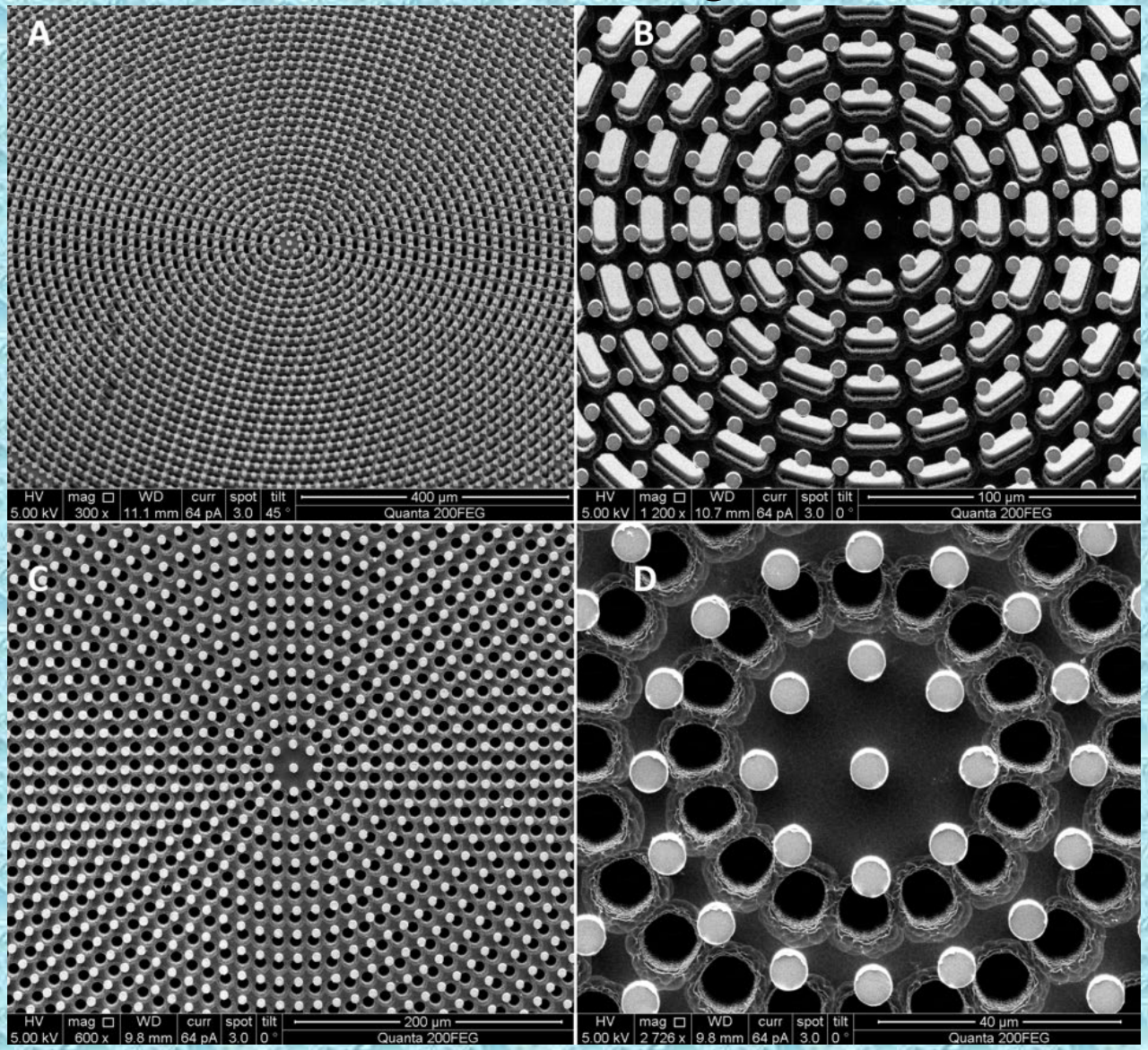

Artificial lotus effect: micropatterned surface

Evaporation of 10 μl of water in few minutes

Contact angle about 160°

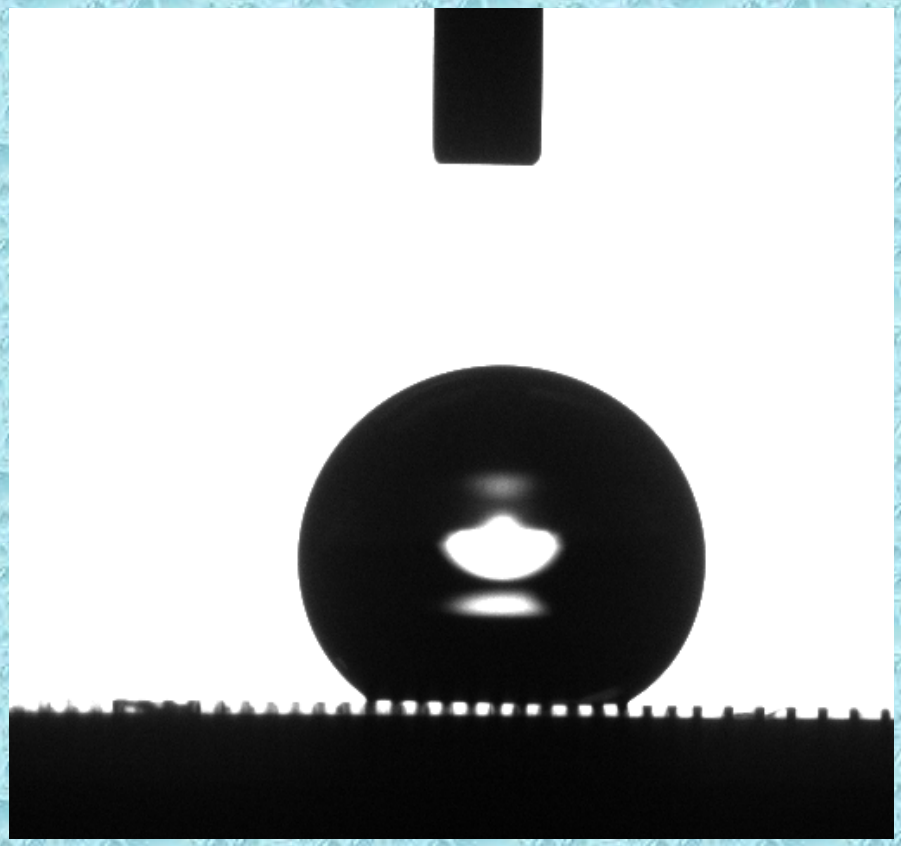

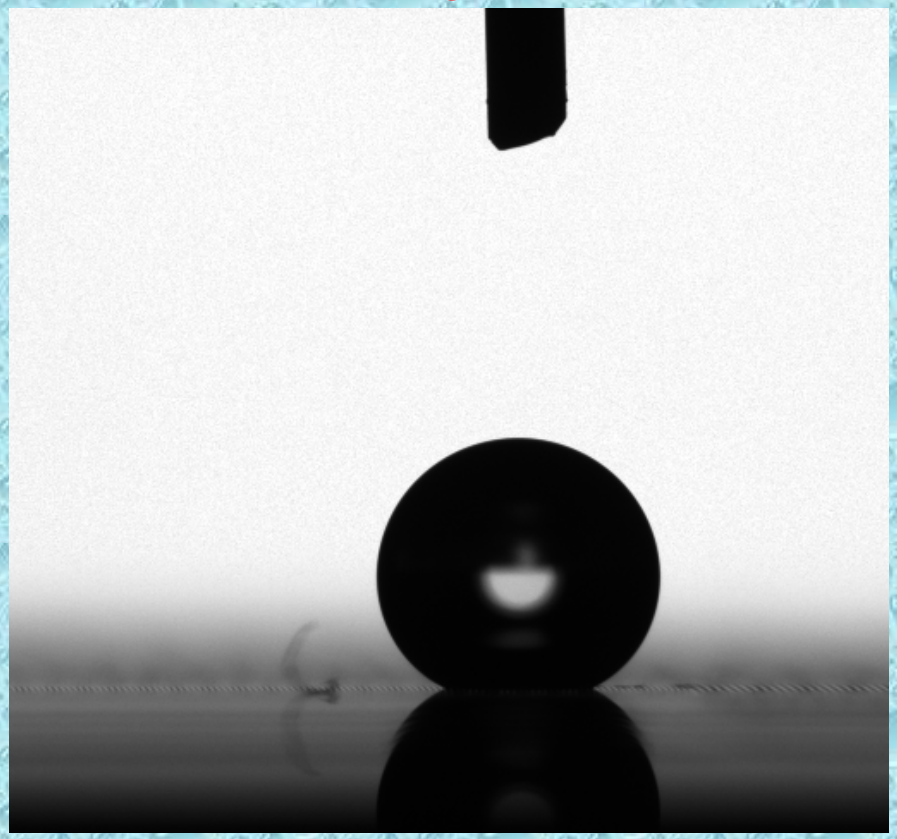

Devices to overcame the diffusion limit: attomolar detection

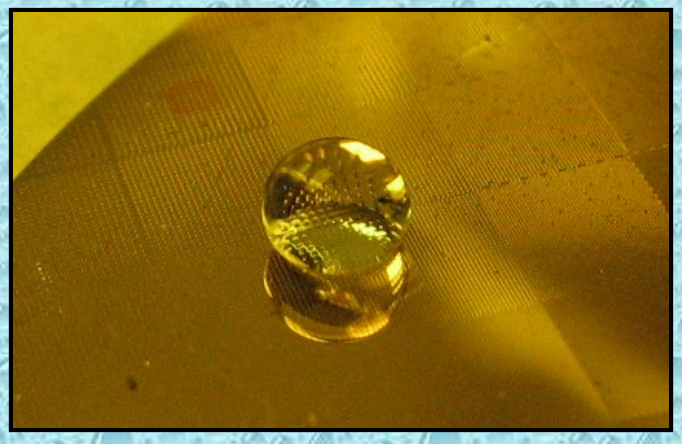

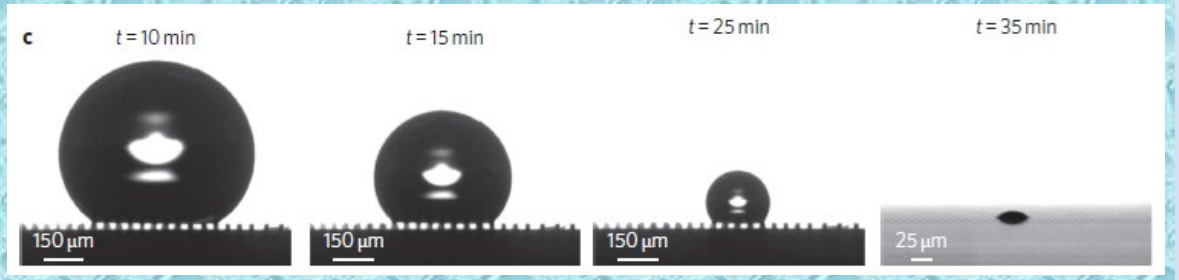

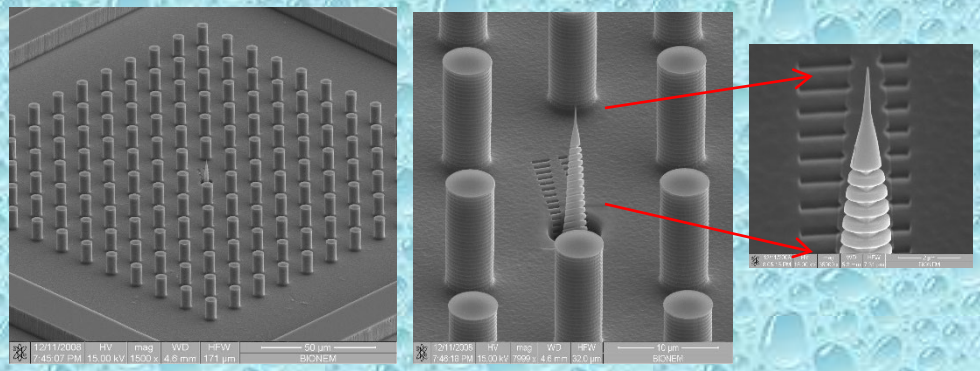

- Single/few molecule detection from highly diluted solution
- Combination with enhanced spectroscopy
- Wide area and chip cost effective for mass production scalability

Plasmonics and Raman measurements (10 AttoMol of lysozime)

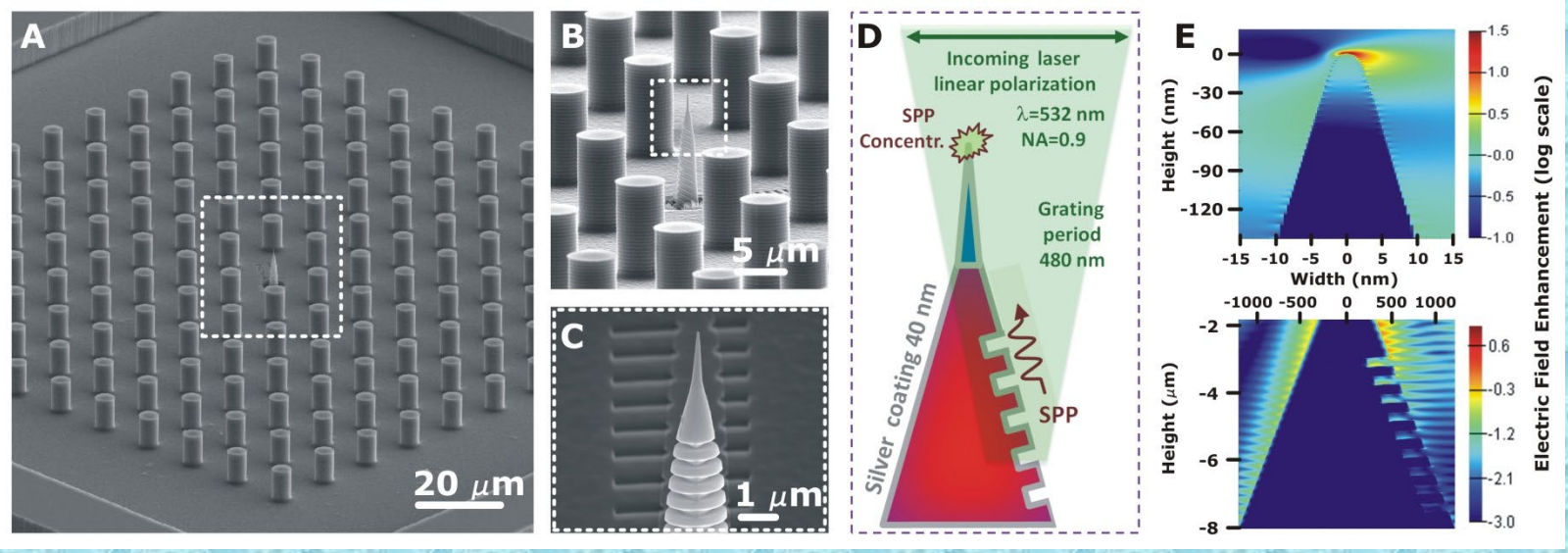

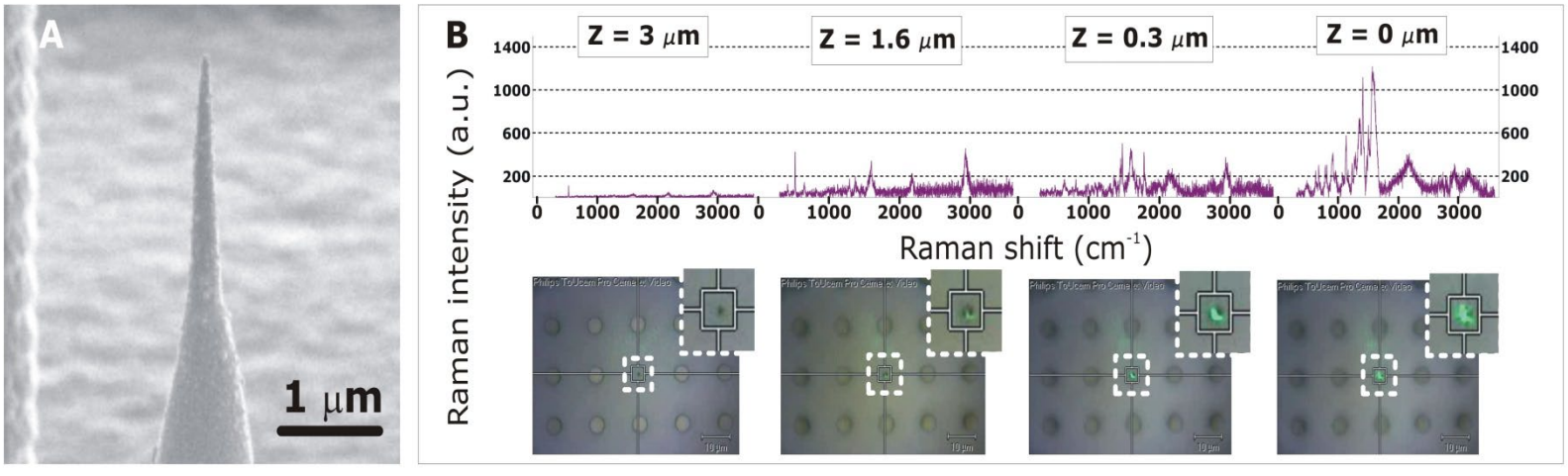

Selected results #3

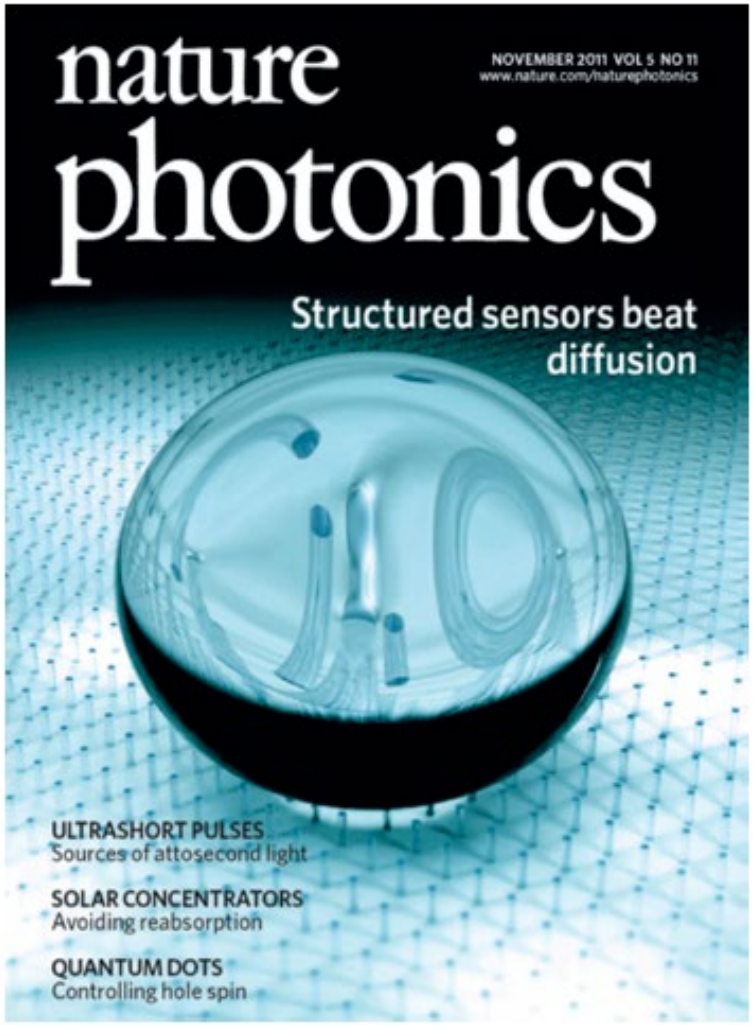

SENSORS

Bypassing the diffusion limit

The detection of ultralow concentrations of molecules using nanoscale optical sensors is hindered by the difficulty in bringing the two into contact, where diffusion acts on impractical timescales. Fortunately, introducing plasmonic structures to super-hydrophobic surfaces may offer a way around this problem.

Jiangang Zhu, Şahin Kaya Özdemir and Lan Yang

The ability to perform sensing measurements at femto- or attomolar sample concentrations with single-molecule resolution is an outstanding achievement in the field of biosensors. The past decade has seen tremendous progress in the development of micro- and nanoscale sensors with impressive performance. Detection limits down to the single-molecule level have been achieved, with potential applications ranging from the early diagnosis of disease to the fast sequencing of genomes. However, in practical applications, transporting target molecules and particles in extremely dilute solutions to these tiny sensors is a significant challenge that often involves impractical timescales.

The physics of diffusion governs the random movement of molecules in a solution and their binding kinetics to the sensor. At ultralow concentrations it takes an unacceptably long amount of time for a molecule to diffuse to the sensor for detection, which may render the sensor impractical[1]. Scientists are now attempting to minimize the time taken for target molecules to bind to such sensors. Exploiting both electrostatics and near-optimal sensor geometry and sample flow, enhancement factors of 100 (relative to pure diffusion) have been demonstrated[2].

Now, writing in *Nature Photonics*, De Angelis *et al.* report a scheme for efficiently delivering molecules in femto/attomolar solutions to a nanoscale plasmonic sensor[3]. Their novel technique involves the integration of plasmonic structures into super-hydrophobic surfaces[4]. Hydrophobic materials repel water — a well-known example being the lotus leaf, on which water droplets form quasi-spheres that do not wet the surface[5]. Inspired by this 'lotus effect', researchers developed super-hydrophobic surfaces that mimic the morphology of the lotus leaf using techniques such as nanopatterning, polymer coating, plasma etching and the electrochemical assembly of nanoparticles[6–8].

De Angelis *et al.* created such a super-hydrophobic surface from arrays of silicon micropillars (Fig. 1). They optimized the size, periodicity and aspect ratio of the pillars to enable a large contact angle (>150°) and low-friction forces that

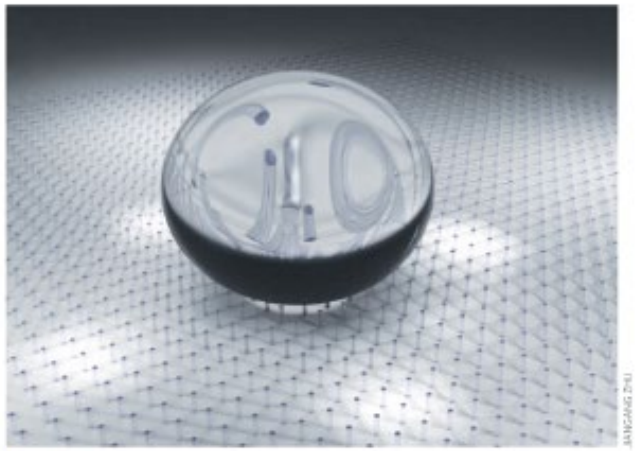

Figure 1 | A water droplet containing molecules at ultralow concentrations on a super-hydrophobic surface made of silicon micropillars.

Superhydrophobic Manipulation for imaging

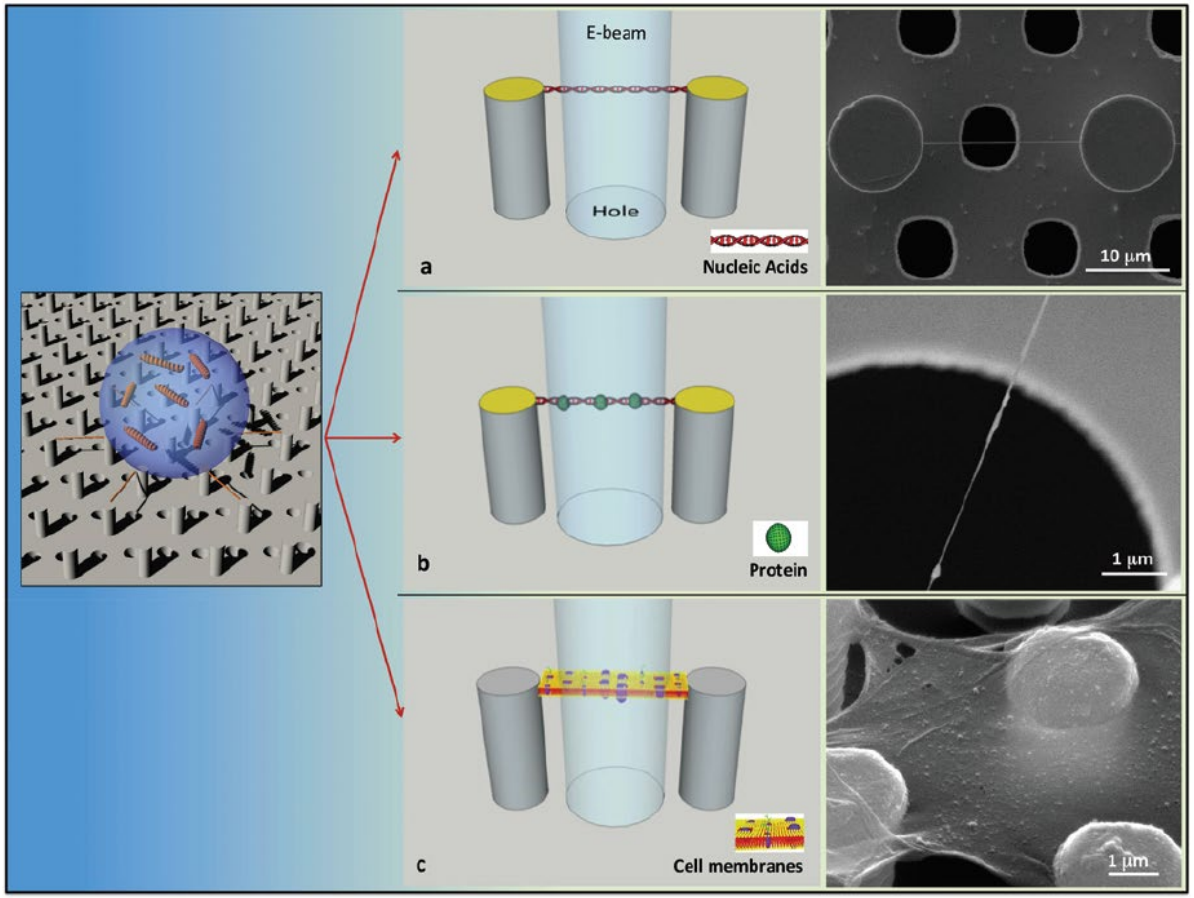

Fig. 1 General scheme and results of the evaporation process. On the left, the deposition of a droplet containing the sample of interest on a super-hydrophobic micro-patterned device is shown. (a, c) After the subsequent evaporation step, the three samples (a, DNA; b, DNA–protein complex; c, plasma membrane patch) are suspended between adjacent μ-pillars. On the right, the respective SEM pictures are reported.

Combination of Plasmonics and hydrophobic surfaces

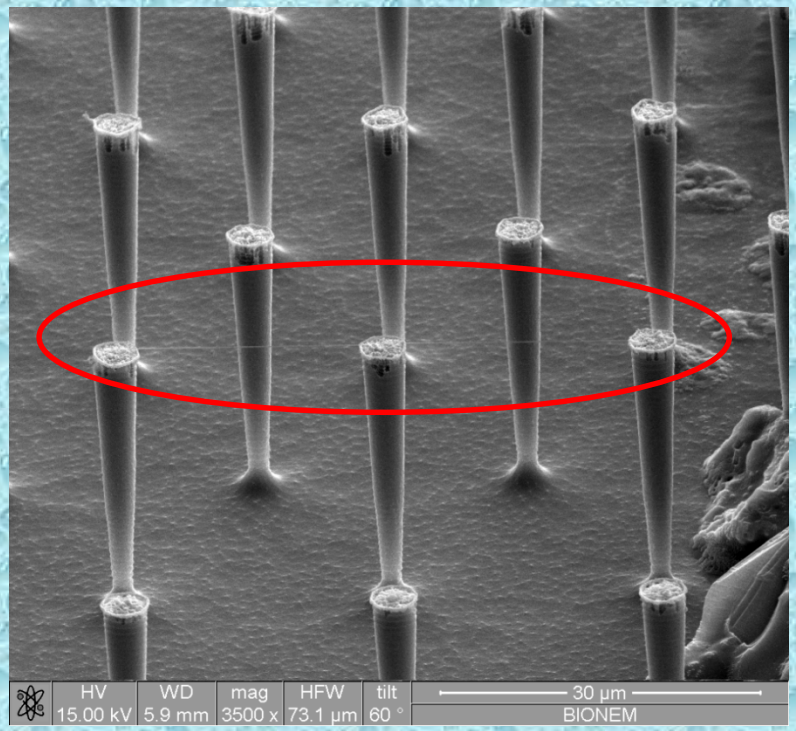

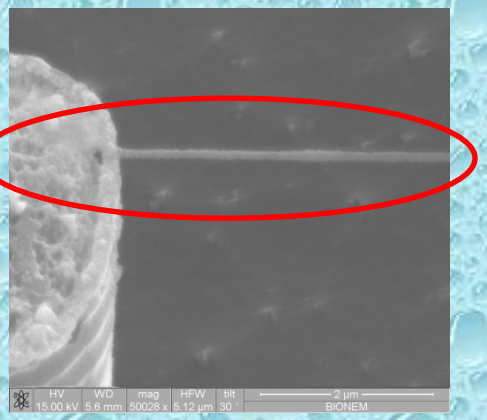

Single λ DNA molecule

Starting concentration: 10^{-17} M

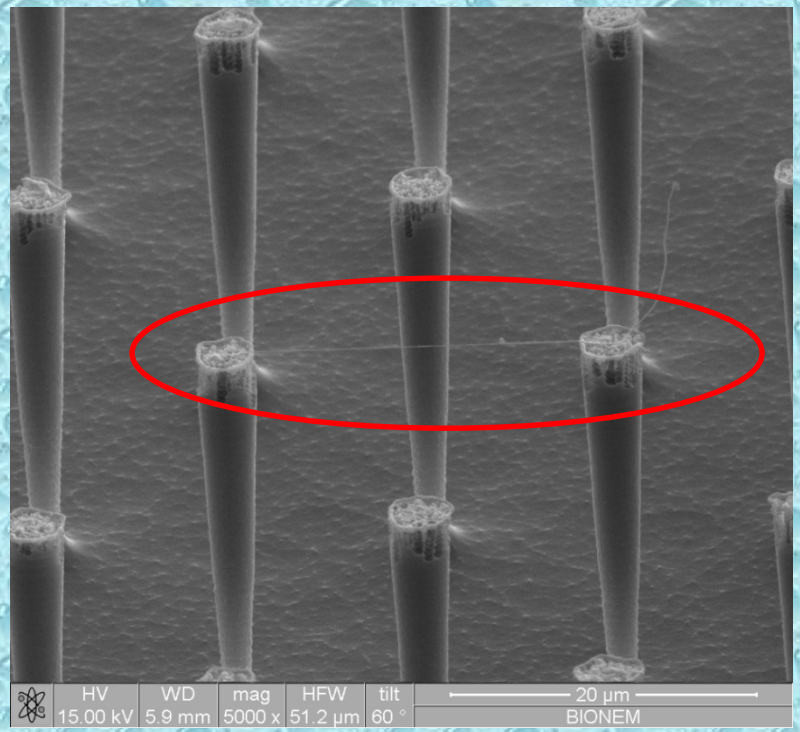

Fluorescence of single λ DNA molecule

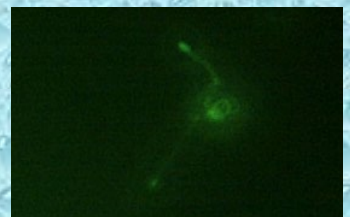

DNA Networking

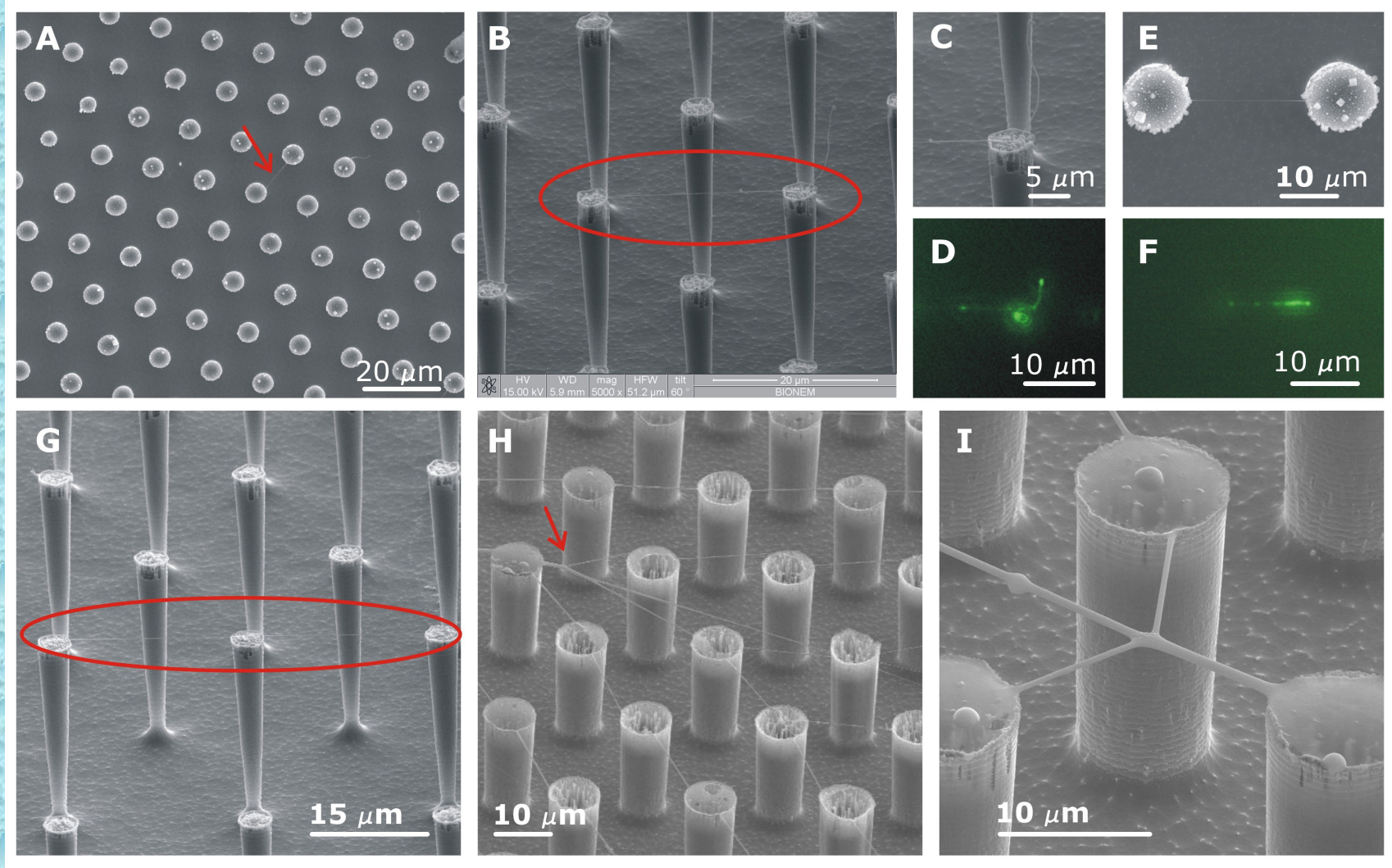

Super-hydrophobic devices for direct imaging

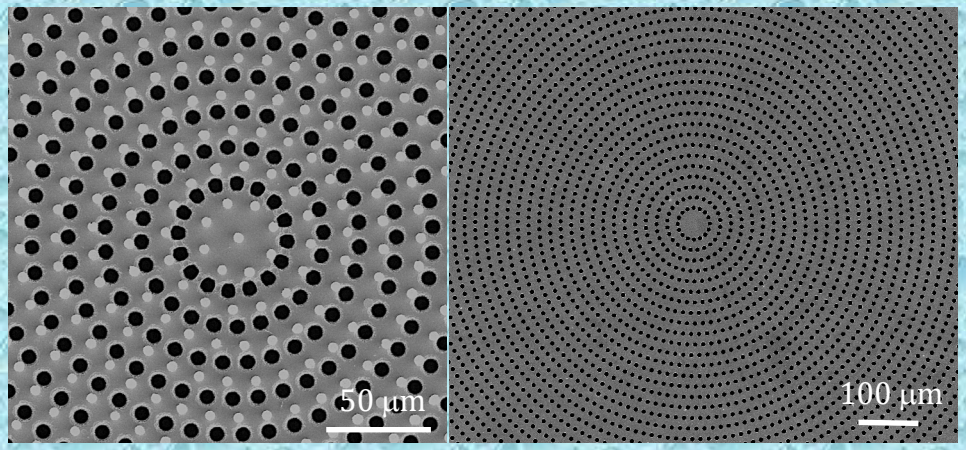

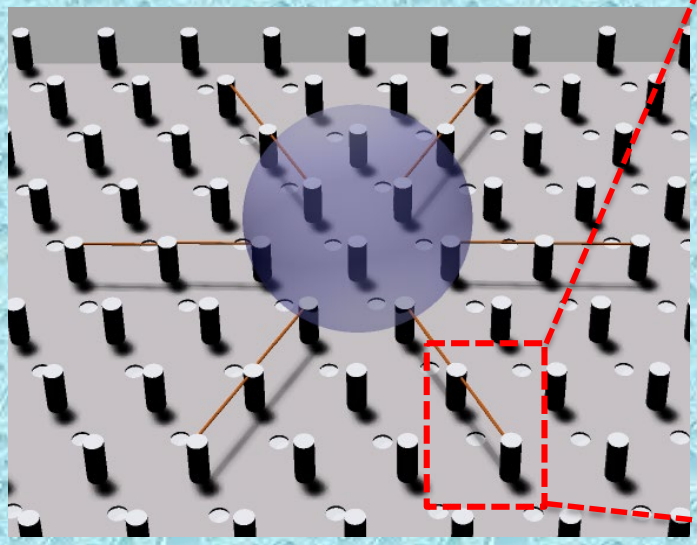

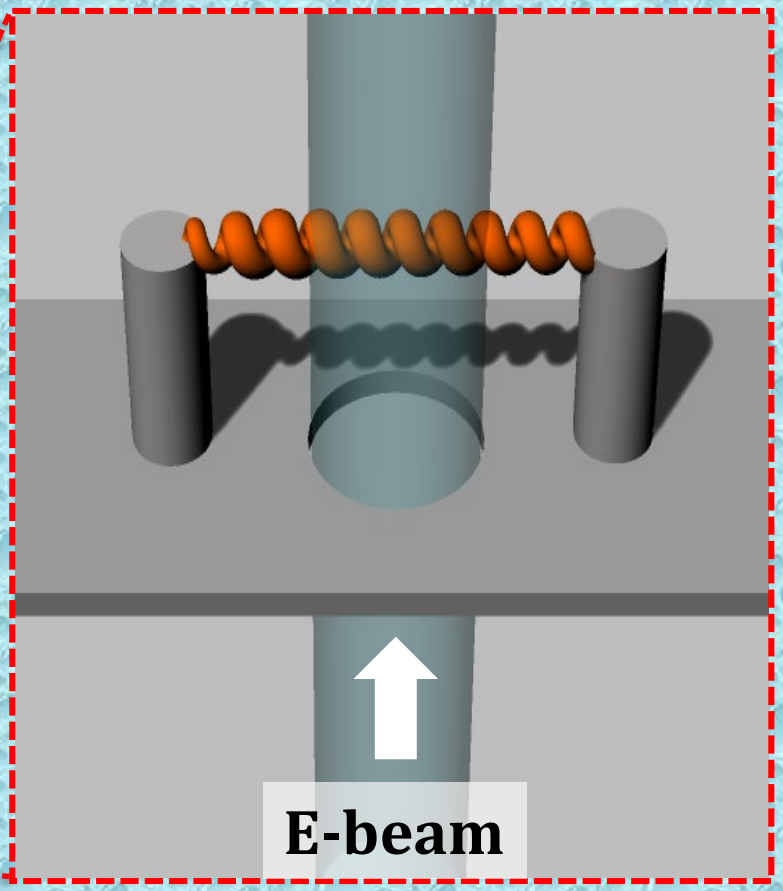

TEM background free suspended DNA

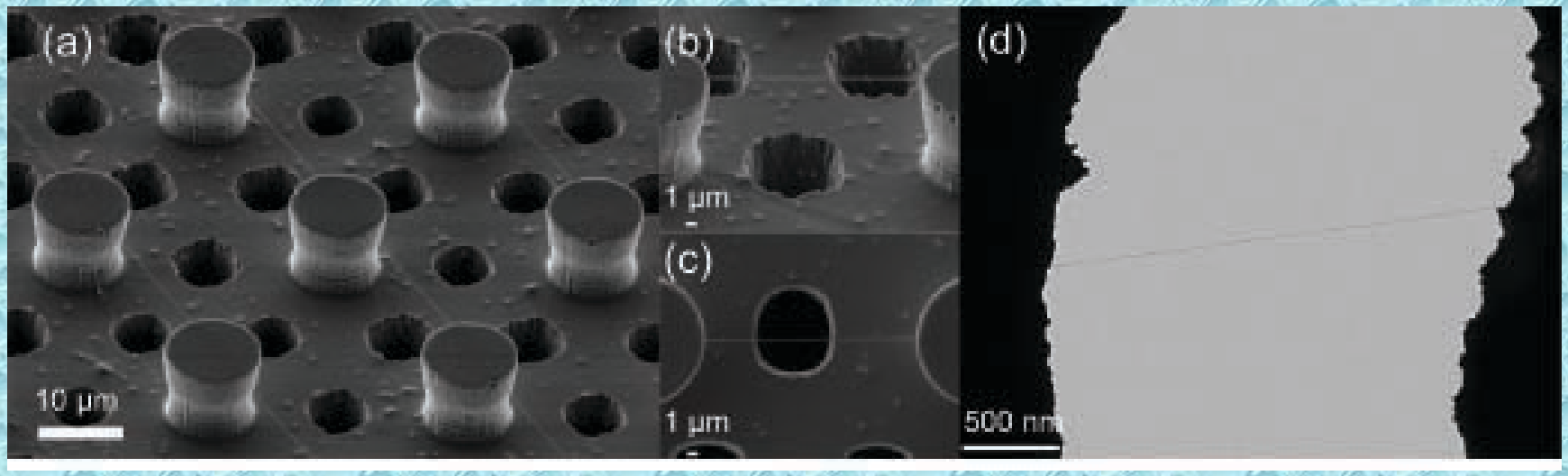

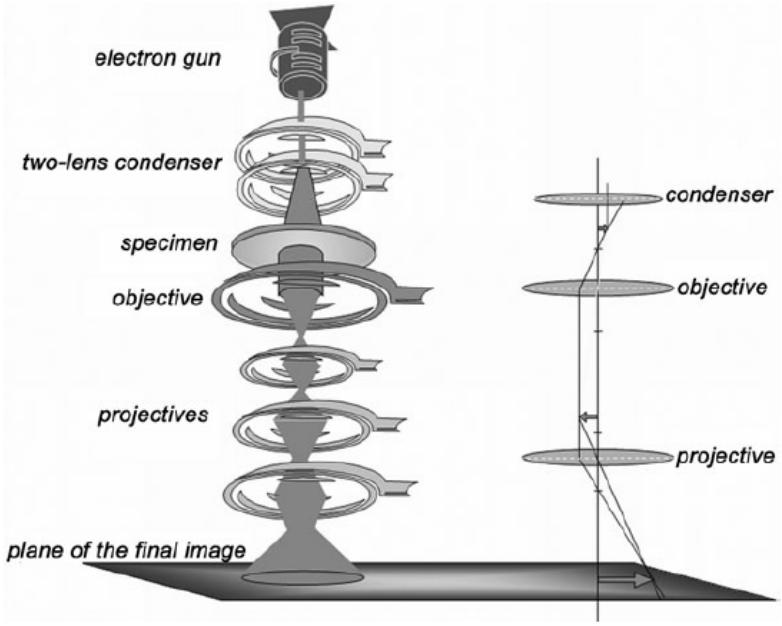

Fig. 2.14 Comparison between light optical microscope (*right*) and transmission electron microscope (*left*)

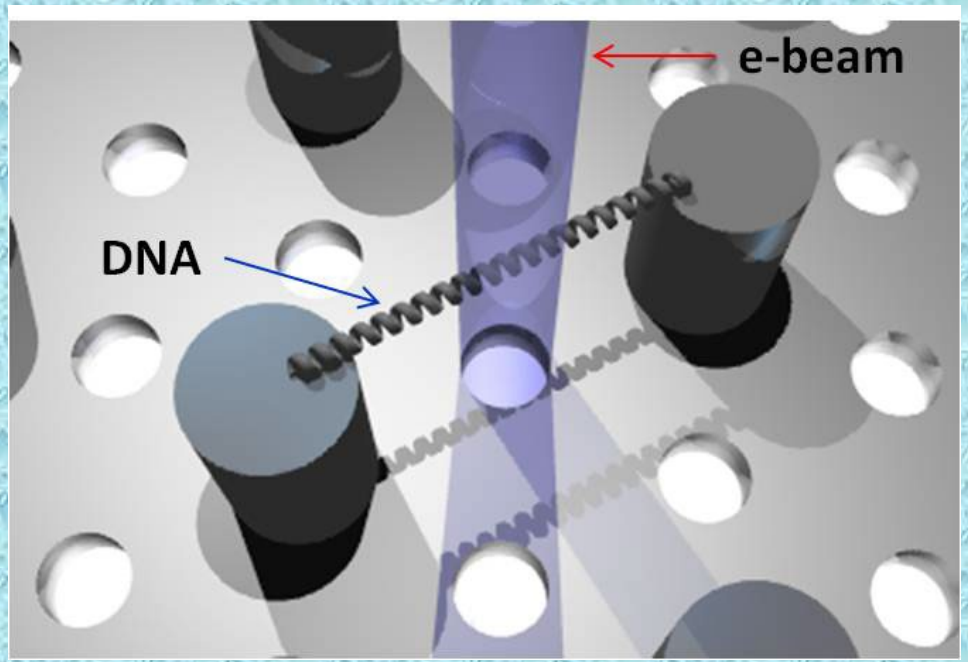

NANO LETTERS
Letter
pubs.acs.org/NanoLett

Direct Imaging of DNA Fibers: The Visage of Double Helix

Francesco Gentile,[†,‡] Manola Moretti,[†] Tania Limongi,[†,§] Andrea Falqui,[⊥] Giovanni Bertoni,[⊥,∥] Alice Scarpellini,[⊥] Stefania Santoriello,[†] Luca Maragliano,[§] Remo Proietti Zaccaria,[†] and Enzo di Fabrizio[†,‡,*]

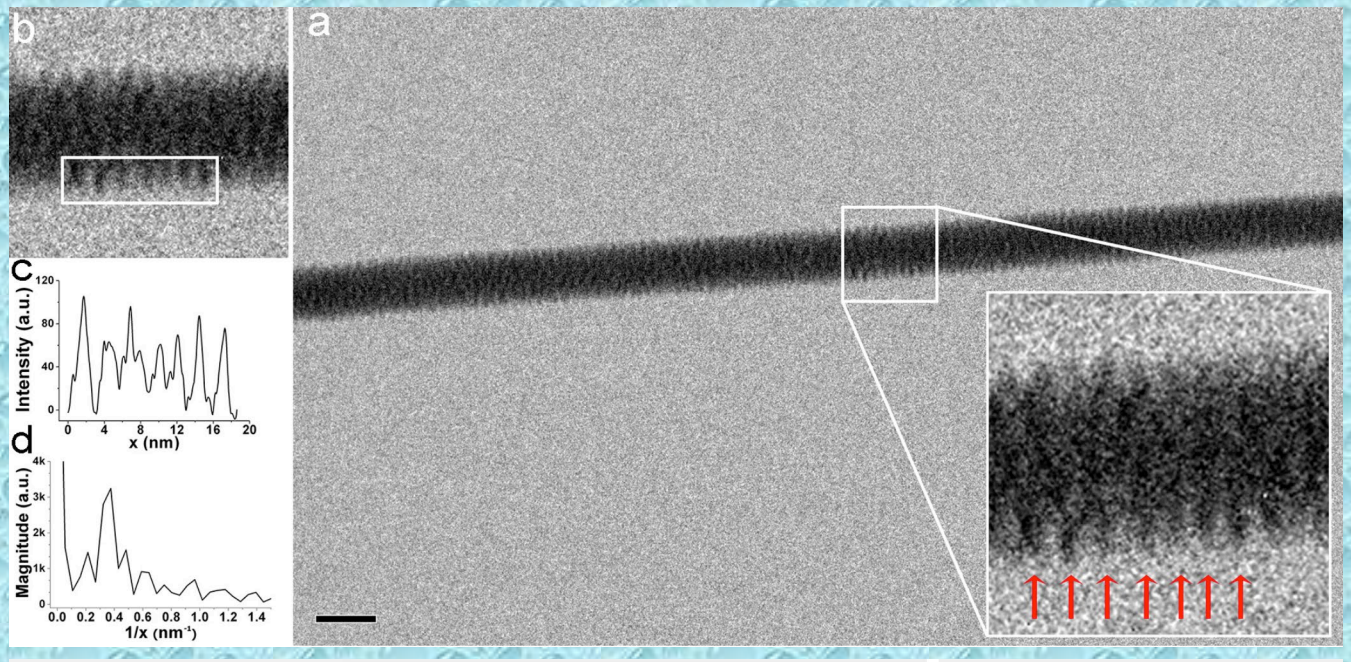

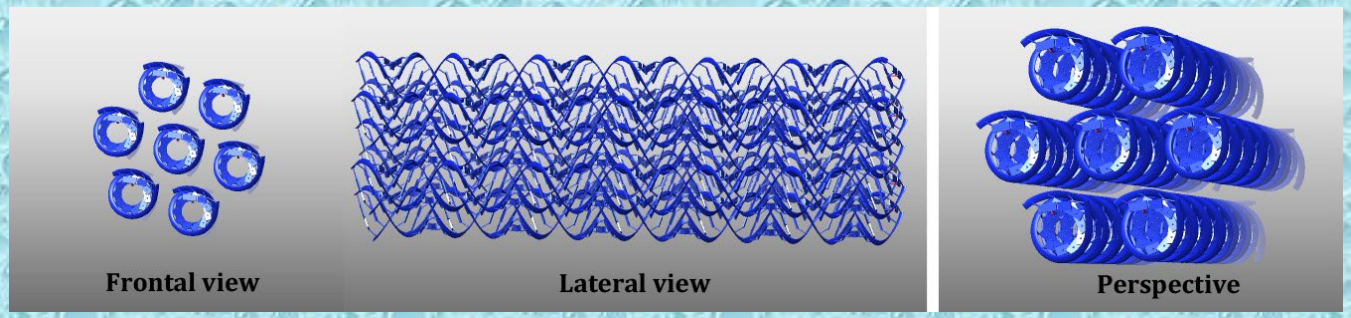

JEOL JEM-1011 TEM

Acc. voltage: 100 keV
Dose: 500 $e^-/Å^2s$
Acquisition time: 2 s

Pitch: 2.7 nm
A-DNA

6+1 geometry

RESEARCH ARTICLE | BIOMATERIALS

The structure of DNA by direct imaging

Monica Marini[1], Andrea Falqui[2], Manola Moretti[1], Tania Limongi[1], Marco Allione[1], Alessandro Genovese[2], Sergei Lopatin[3], Luca Tirinato[1], Gobind Das[1], Bruno Torre[1], Andrea Giugni[1], Francesco Gentile[4,*], Patrizio Candeloro[4] and Enzo Di Fabrizio[1,4,†]

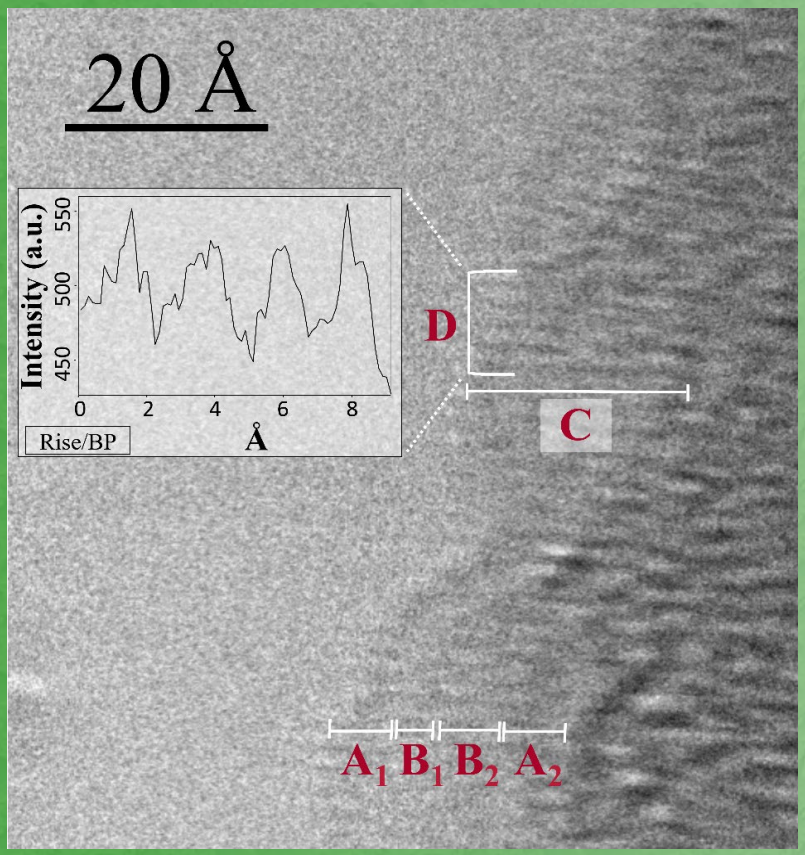

A-DNA Metrology	(Å)
Diameter (C)	21.2
Rise/BP along axis (D)	2.5
Phosphate+Sugar (Backbone A_1)	5.1
Purine Base (B_1)	3.6
Pyrimidine Base (B_2)	5.2
Phosphate+Sugar (Backbone A_2)	5
Bases Length (B_1+B_2+bases interdistance)	11.3

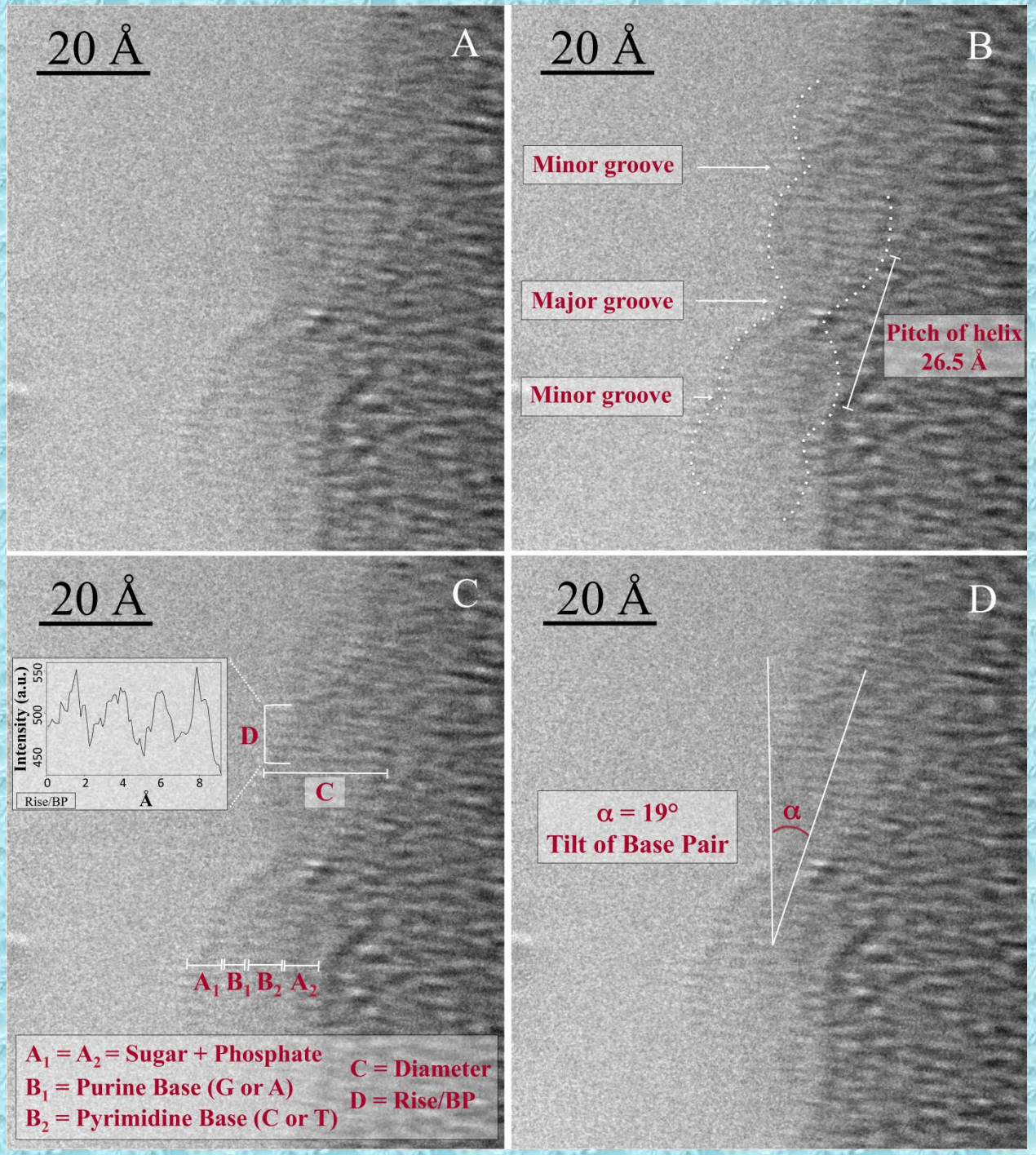
20 Å
A
20 Å
B
Minor groove
Major groove
Minor groove
Pitch of helix
26.5 Å
20 Å
C
Intensity (a.u.)
550
500
450
0
2
4
6
8
Å
Rise/BP
D
C
A1 B1 B2 A2
A1 = A2 = Sugar + Phosphate
B1 = Purine Base (G or A)
B2 = Pyrimidine Base (C or T)
C = Diameter
D = Rise/BP
20 Å
D
α = 19°
Tilt of Base Pair
α

Single molecule dsDNA metrology

Research paper
Microelectronic Engineering 187–188 (2018) 39–42

Suspended DNA structural characterization by TEM diffraction

Monica Marini [a,*], Marco Allione [a], Sergei Lopatin [b], Manola Moretti [a], Andrea Giugni [a], Bruno Torre [a], Enzo di Fabrizio [a]

[a] SMILEs Lab, PSE Division, King Abdullah University of Science and Technology (KAUST), Thuwal 23955-6900, Saudi Arabia
[b] Imaging and Characterization Core Lab, King Abdullah University of Science and Technology (KAUST), Thuwal 23955-6900, Saudi Arabia

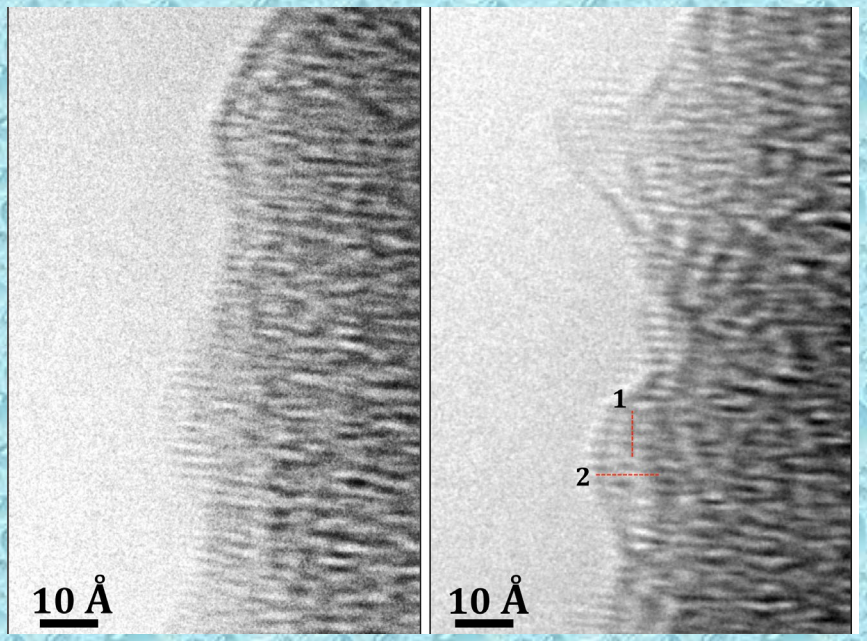

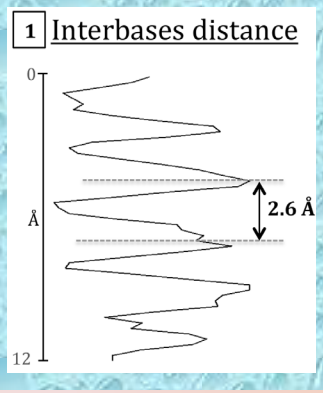

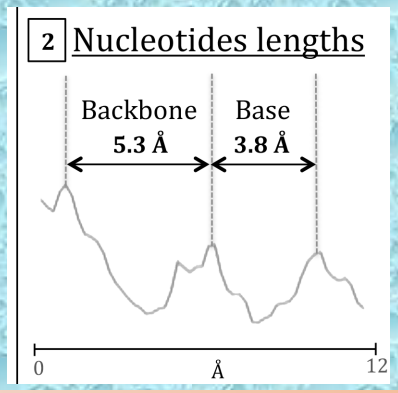

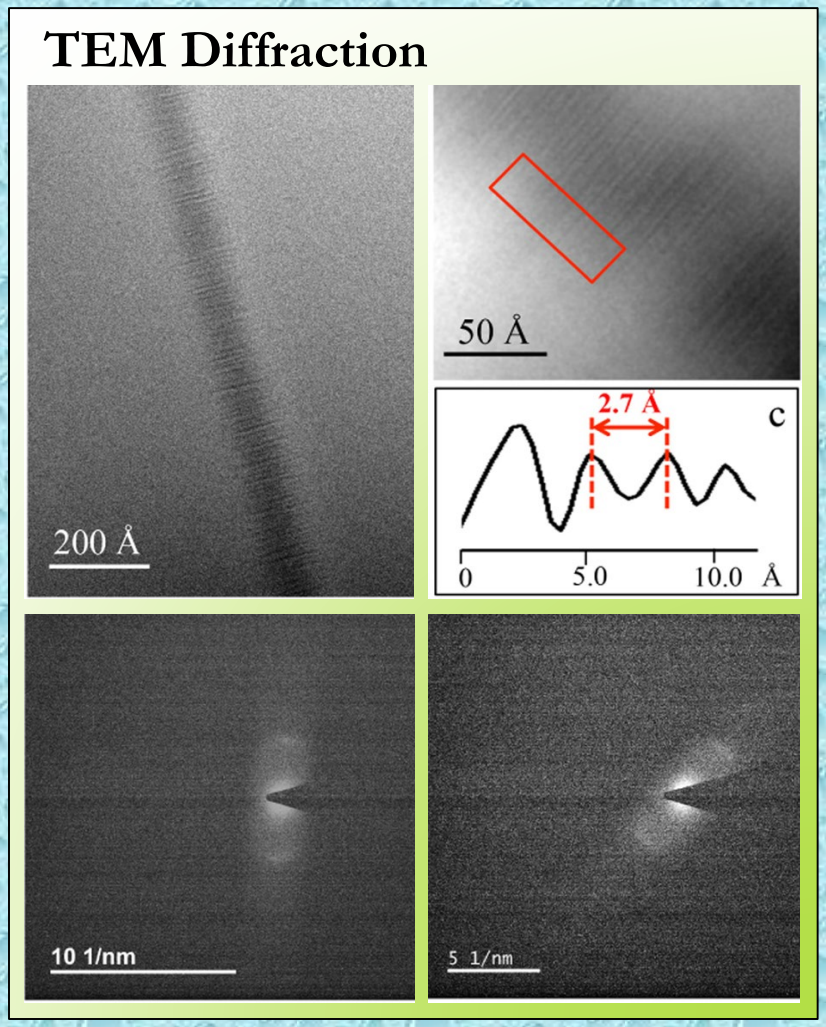

twist of the A-T couple of bases

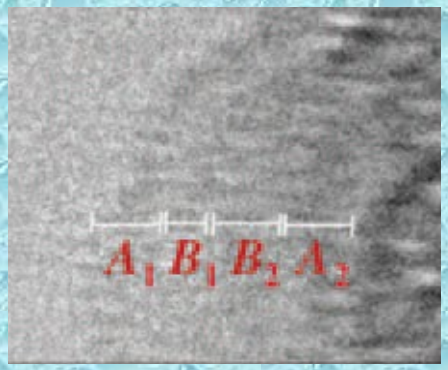

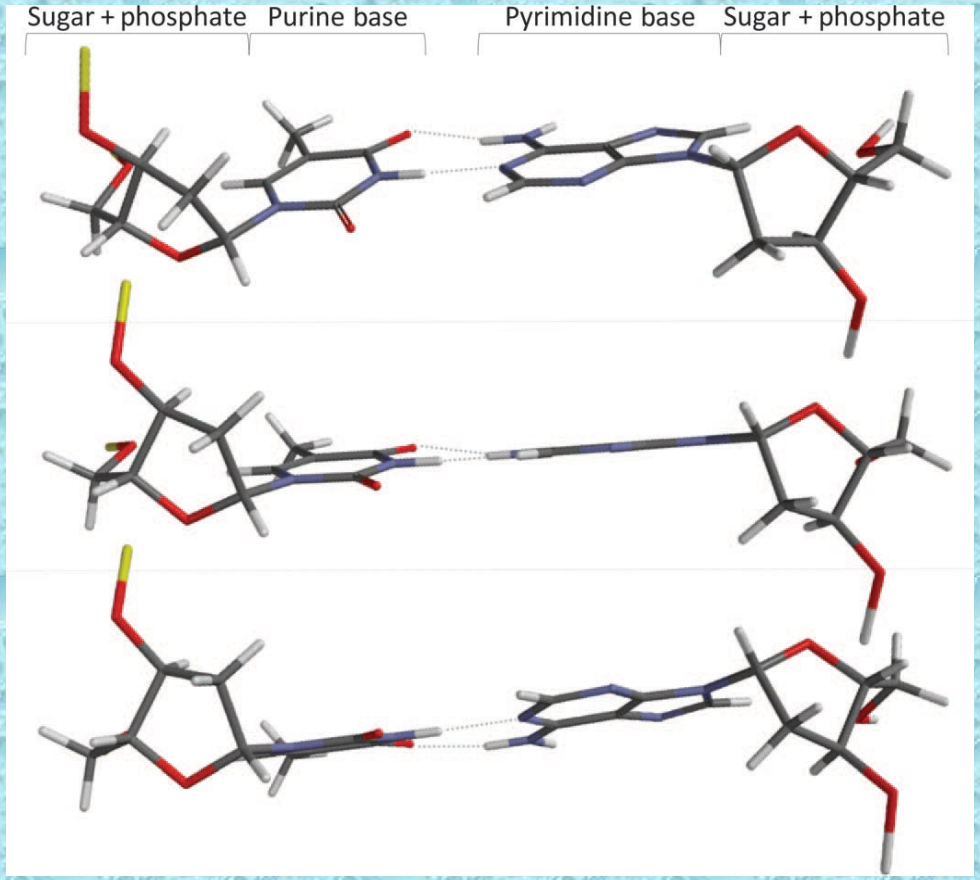

Fig. 2. Base propeller twist. A representative image of simulating different

Selected results #5

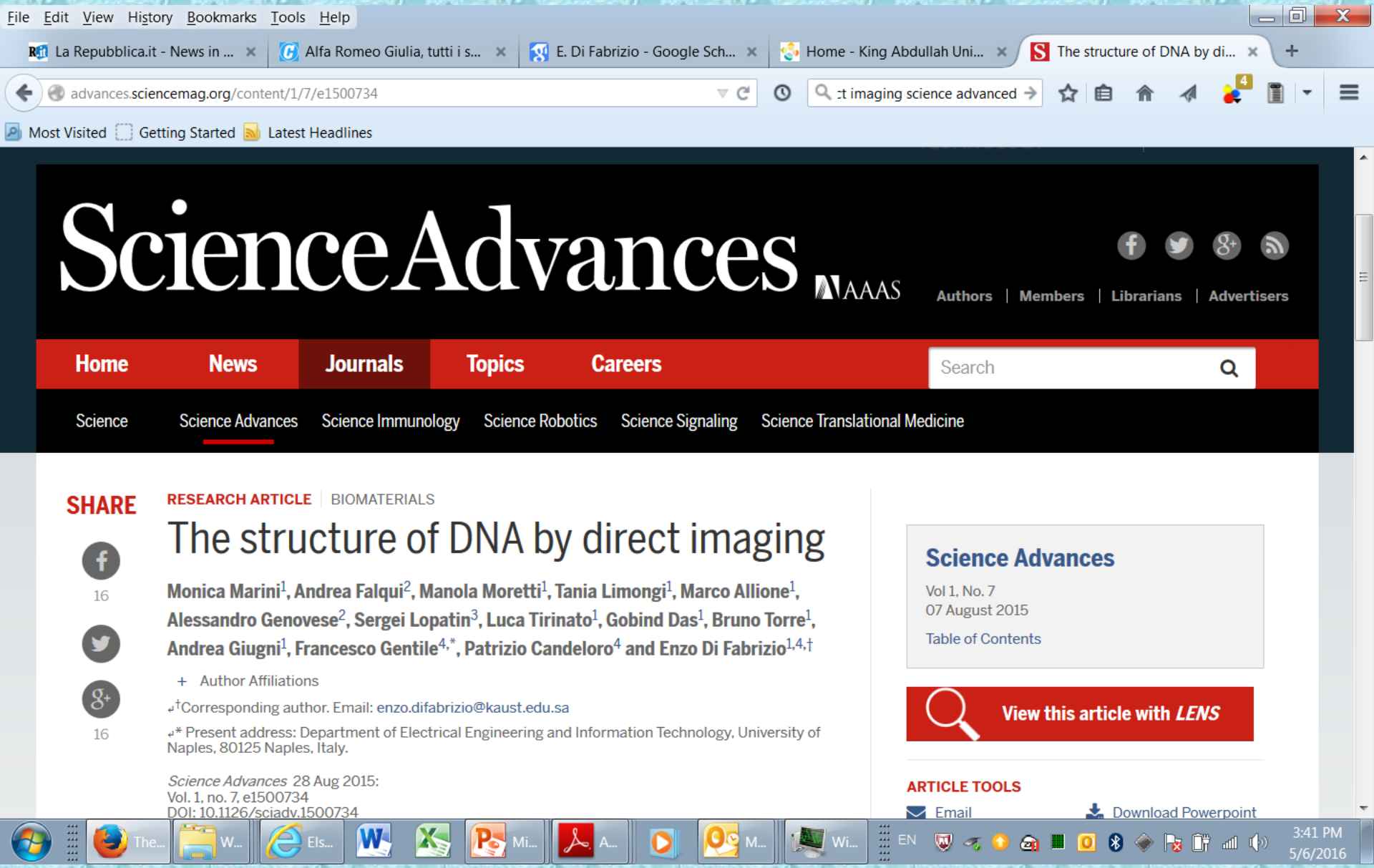

File Edit View History Bookmarks Tools Help

La Repubblica.it - News in ... | Alfa Romeo Giulia, tutti i s... | E. Di Fabrizio - Google Sch... | Home - King Abdullah Uni... | The structure of DNA by di...

advances.sciencemag.org/content/1/7/e1500734

:t imaging science advanced

Most Visited | Getting Started | Latest Headlines

Science Advances AAAS

Authors | Members | Librarians | Advertisers

Home | News | Journals | Topics | Careers | Search

Science | Science Advances | Science Immunology | Science Robotics | Science Signaling | Science Translational Medicine

SHARE

16

16

RESEARCH ARTICLE | BIOMATERIALS

The structure of DNA by direct imaging

Monica Marini[1], Andrea Falqui[2], Manola Moretti[1], Tania Limongi[1], Marco Allione[1], Alessandro Genovese[2], Sergei Lopatin[3], Luca Tirinato[1], Gobind Das[1], Bruno Torre[1], Andrea Giugni[1], Francesco Gentile[4,*], Patrizio Candeloro[4] and Enzo Di Fabrizio[1,4,†]

+ Author Affiliations

†Corresponding author. Email: enzo.difabrizio@kaust.edu.sa

* Present address: Department of Electrical Engineering and Information Technology, University of Naples, 80125 Naples, Italy.

Science Advances 28 Aug 2015:
Vol. 1, no. 7, e1500734
DOI: 10.1126/sciadv.1500734

Science Advances
Vol 1, No. 7
07 August 2015
Table of Contents

View this article with *LENS*

ARTICLE TOOLS
Email | Download Powerpoint

3:41 PM
5/6/2016

DNA mechanical characterization: Laser Doppler Vibrometer 1/2

nature COMMUNICATIONS

Nanomechanical DNA resonators for sensing and structural analysis of DNA-ligand complexes

Stefano Stassi*, Monica Marini*, Marco Allione, Sergei Lopatin, Domenico Marson, Erik Laurini, Sabrina Pricl, Candido Fabrizio Pirri, Carlo Ricciardi ✉ & Enzo Di Fabrizio ✉

Nature Communications **10**, Article number: 1690 (2019)

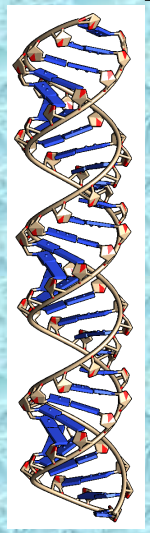

dsDNA

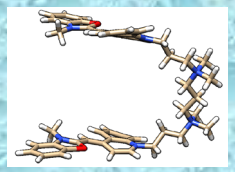

Bis-intercalators

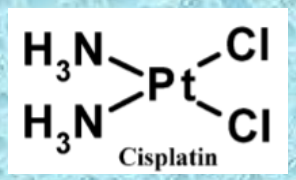

Chemotherapeutics

NON covalent interaction

Covalent interaction

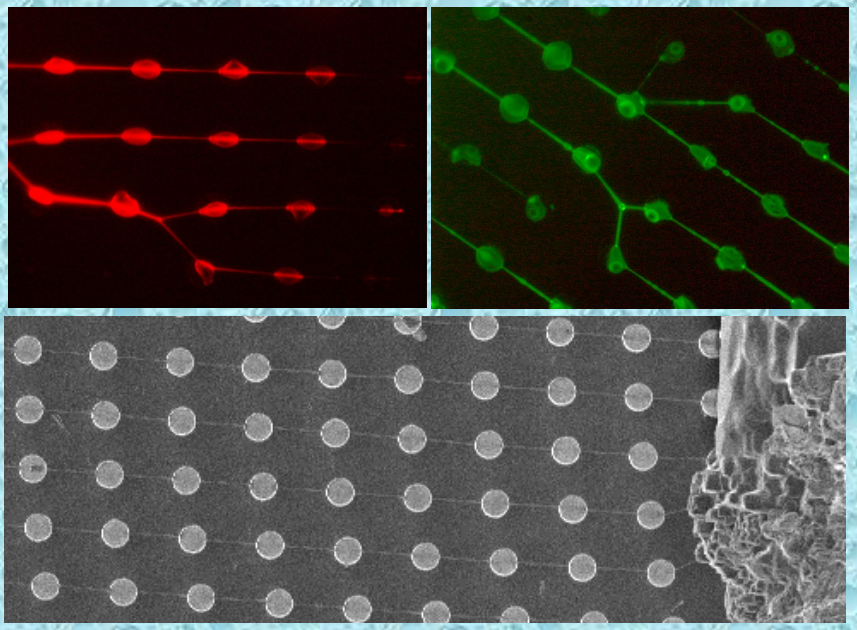

DNA nanomechanical resonator 2/2

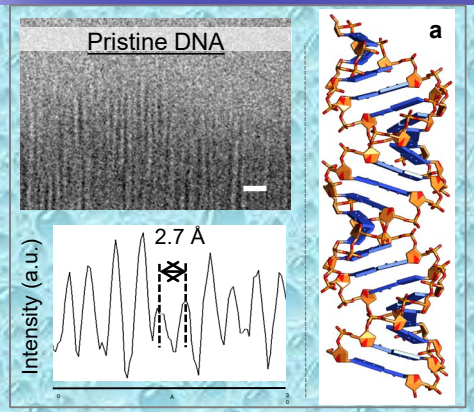

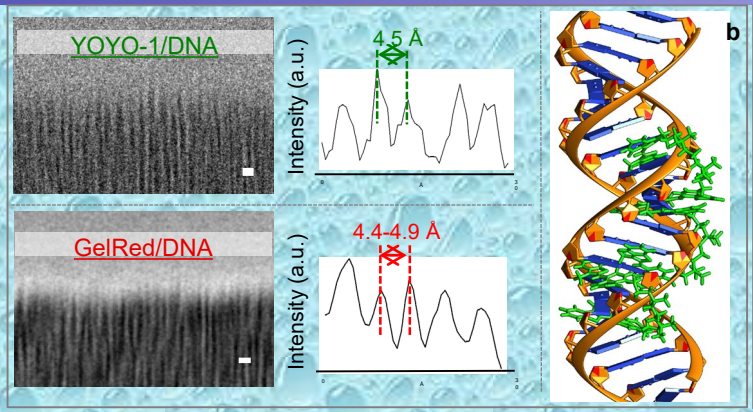

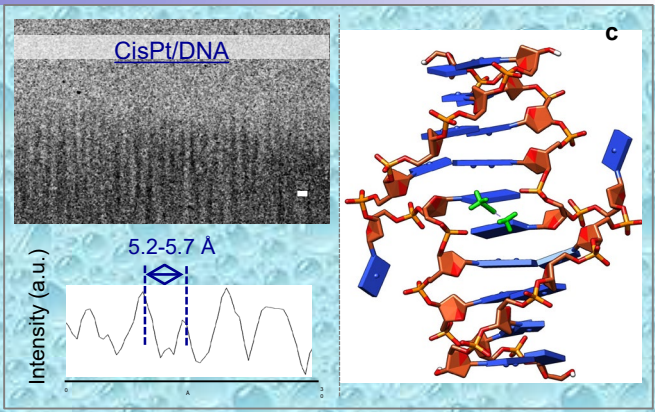

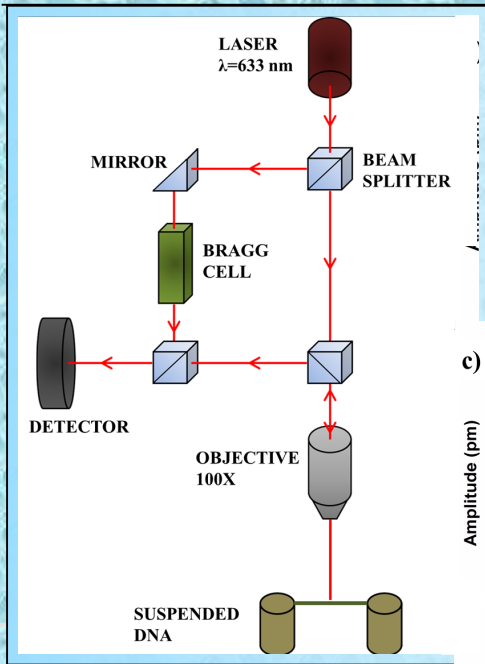

- Optical system to study the Resonance freq./i.e. mechanical properties of the bundles
- Measurements in air
- Young's modulus

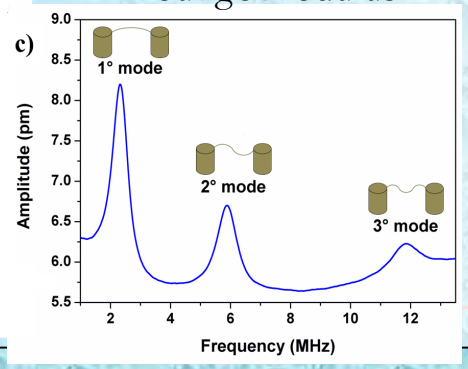

Saturation levels

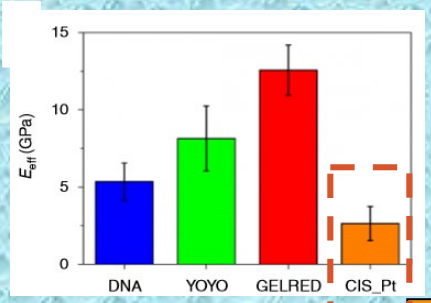

CisPt titration

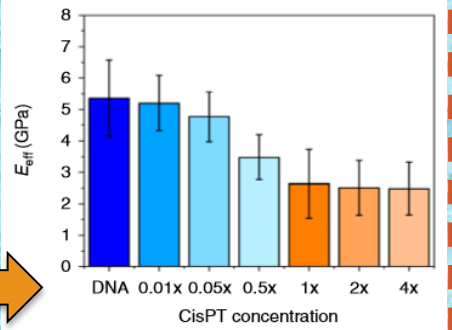

Molecular Dynamics

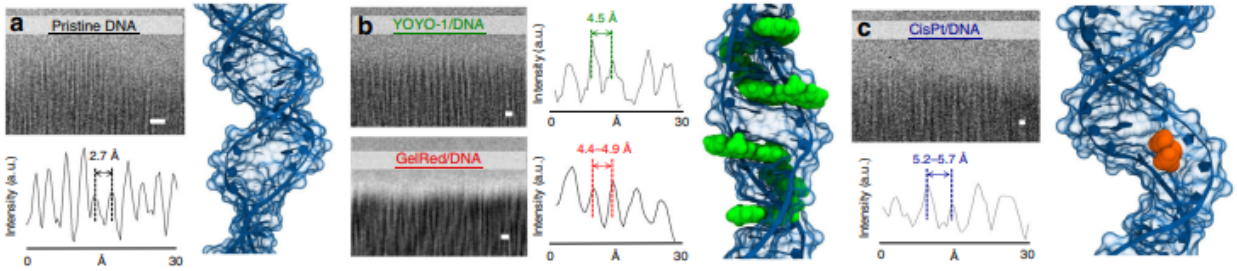

Fig. 2 HRTEM images, related metrology, and schemes. Interbase distance details of a pristine DNA bundle (**a**), DNA bundle with bis-intercalators (**b**), and DNA with CisPt adducts (**c**). The DNA interbase distance changes from 2.7 Å in the pristine DNA conformation to ~4.5 Å and 5.2 Å in the DNA altered by the presence of intercalant molecules or CisPt, respectively. The scale bars correspond to 10 Å. Notice that for panels **b** and **c**, the models are just an indication of the action of each intercalant molecule and the changes of the periods are not reported

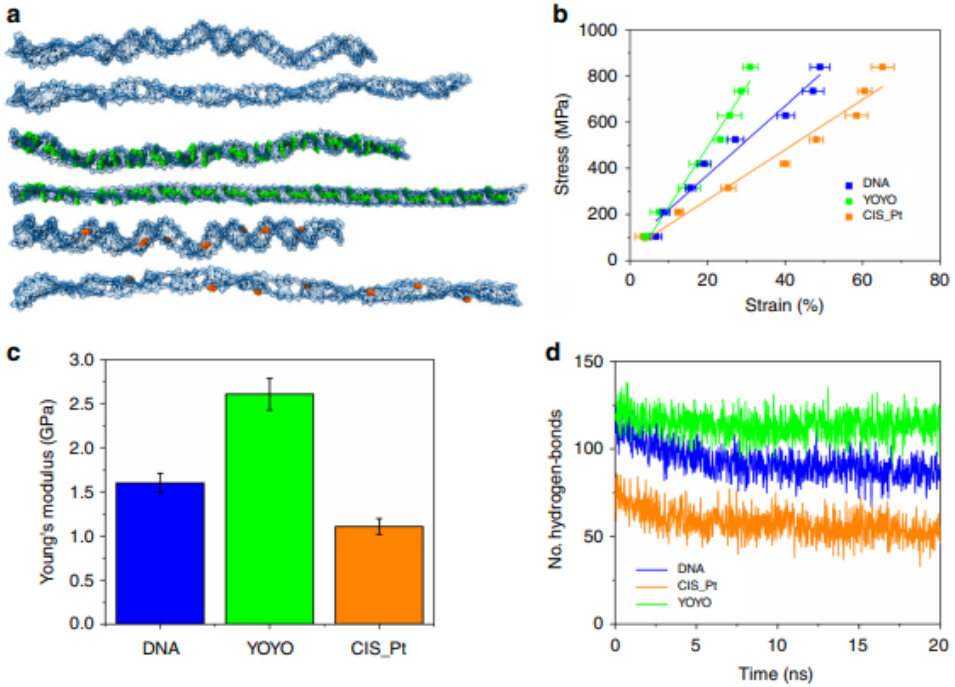

Fig. 3 SMD simulations of pristine DNA and DNA intercalated with YOYO-1 and CisPt. **a** Simulated conformational structures of the bare DNA (top), DNA intercalated with YOYO-1 (center), and CisPt (bottom) under uniaxial stretching deformation. In each figure, the first corresponds to the initial structure, while the second represents the final conformation reached at the maximum simulated strain. **b** Stress–strain curve of the unidirectional traction applied to the DNA (blue), DNA/YOYO-1 (green), and DNA/CisPt (orange) systems. The Young's moduli (E_{SMD}) for each complex are calculated from the slope of the linear fitting. The strain at each force has been averaged over three simulations and the corresponding standard errors are reported. **c** Calculated Young's modulus (E_{SMD}) values for DNA (blue), DNA/YOYO-1 (green), and DNA–CisPt (orange) complexes. **d** Change in the number of hydrogen bonds of DNA (blue), DNA/YOYO-1 (green), and DNA/CisPt (orange) systems during the simulation time applying the maximum stress value. Source data are provided as a Source Data file

What's next

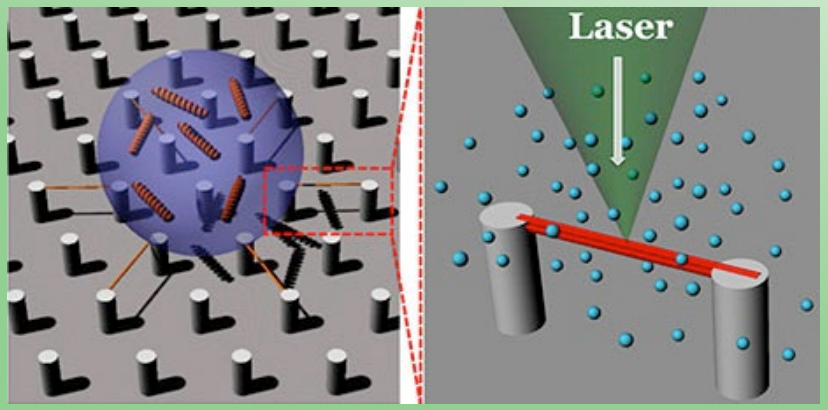

More hydrated conditions

RH>75%

Study of the effects on DNA of:

1) Epigenetic alterations
2) Heavy metals

Move to Genomic DNA

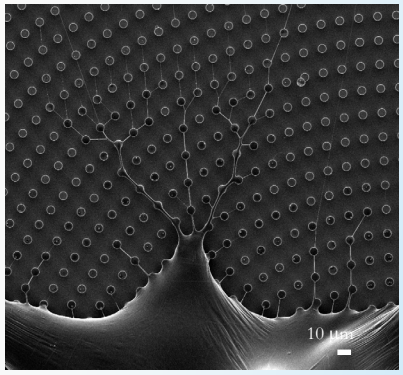

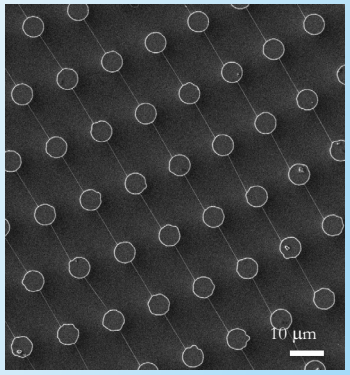

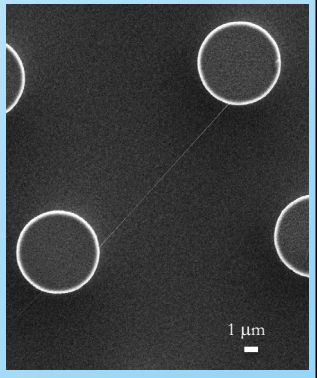

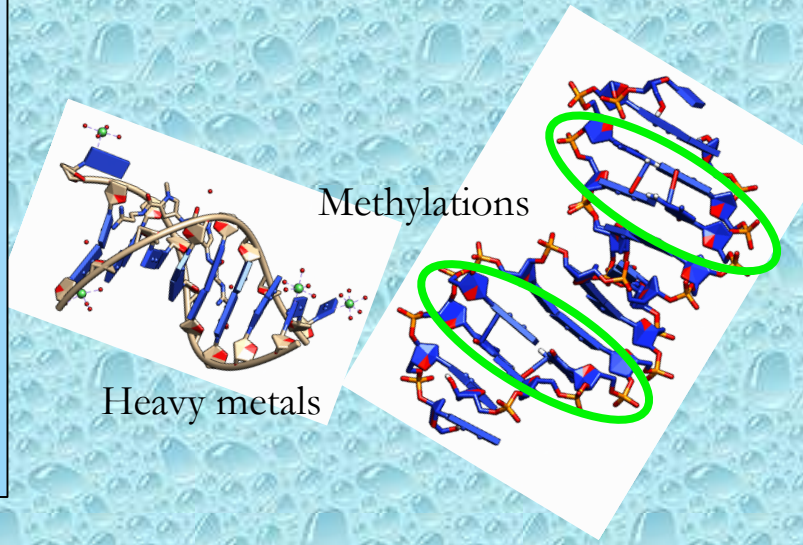

Superhydrophobic membrane Manipulation

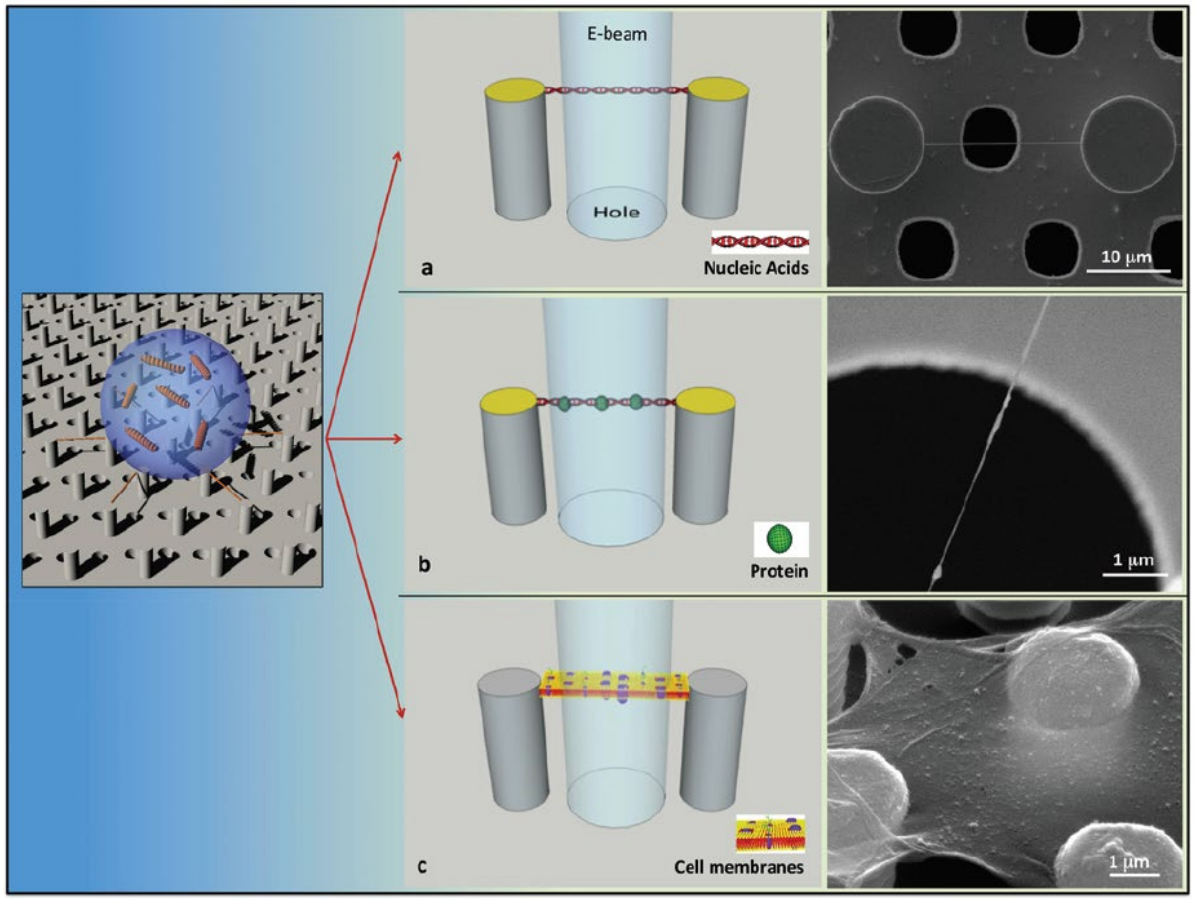

Fig. 1 General scheme and results of the evaporation process. On the left, the deposition of a droplet containing the sample of interest on a super-hydrophobic micro-patterned device is shown. (a, c) After the subsequent evaporation step, the three samples (a, DNA; b, DNA–protein complex; c, plasma membrane patch) are suspended between adjacent μ-pillars. On the right, the respective SEM pictures are reported.

Suspended Neural membrane

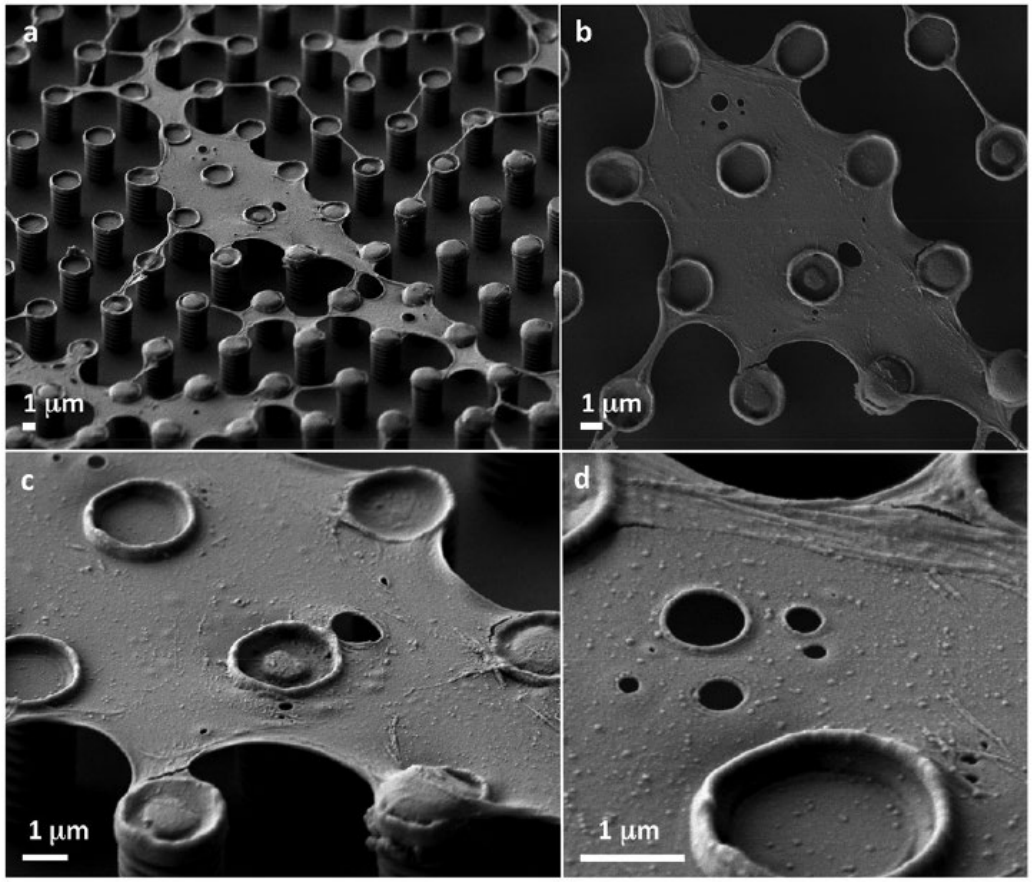

Fig. 5 SEM images of cortical neuronal membranes suspended over the SHS. (a) Low-magnification view of parts of the suspended membranes, with the substrate tilting angle of 35 degrees. (b) Top view (untilted sample) of the membrane around the central location of panel a. (c) 35 degrees tilting view at higher magnification of the same location shown in panel b. (d) 35 degrees tilting high-magnification image showing aggregates of membrane proteins.

TEM imaging after 2% Glutaraldehyde fixation
TEM Jeol JSM 1011- 100 kV

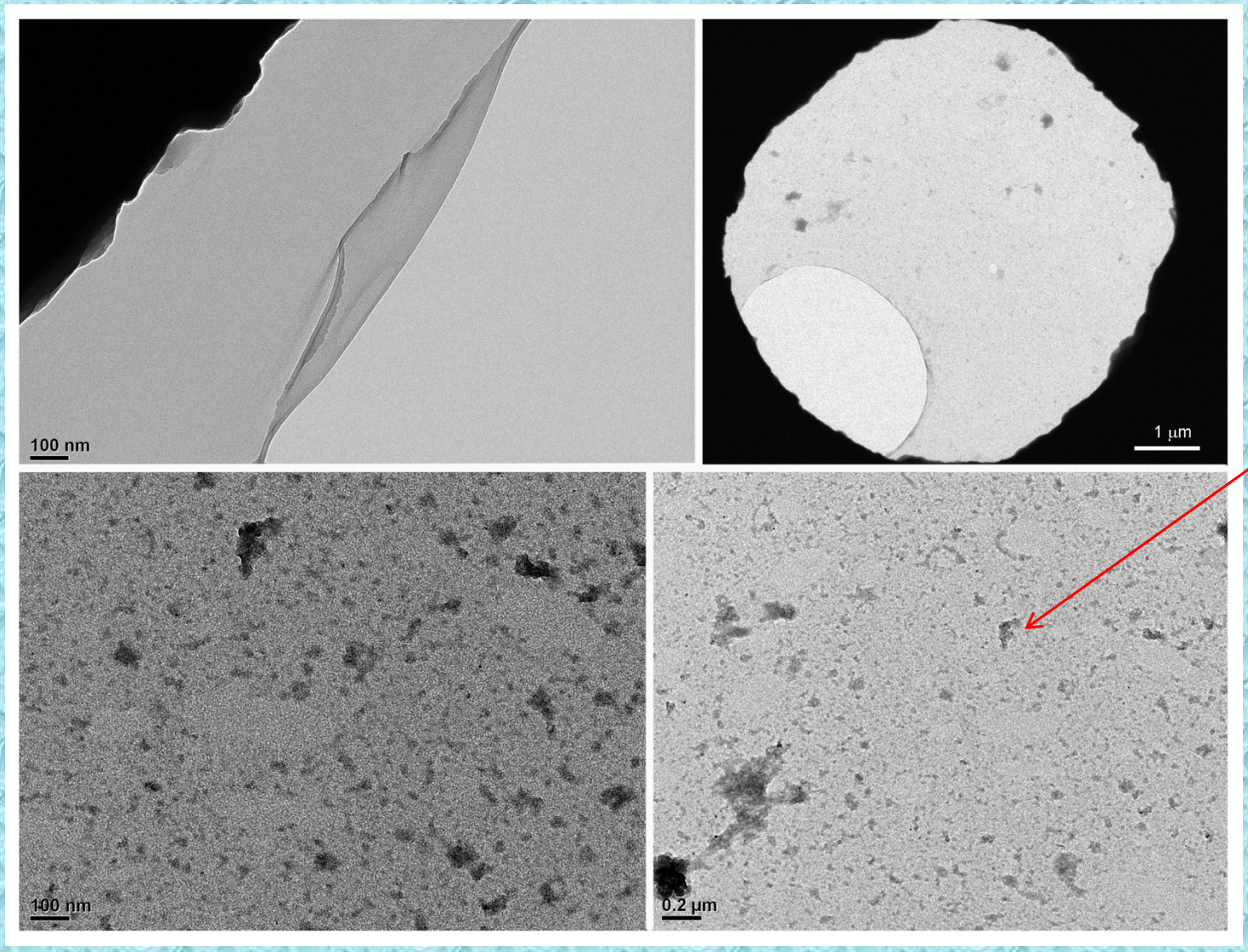

Imaging of single ion channel

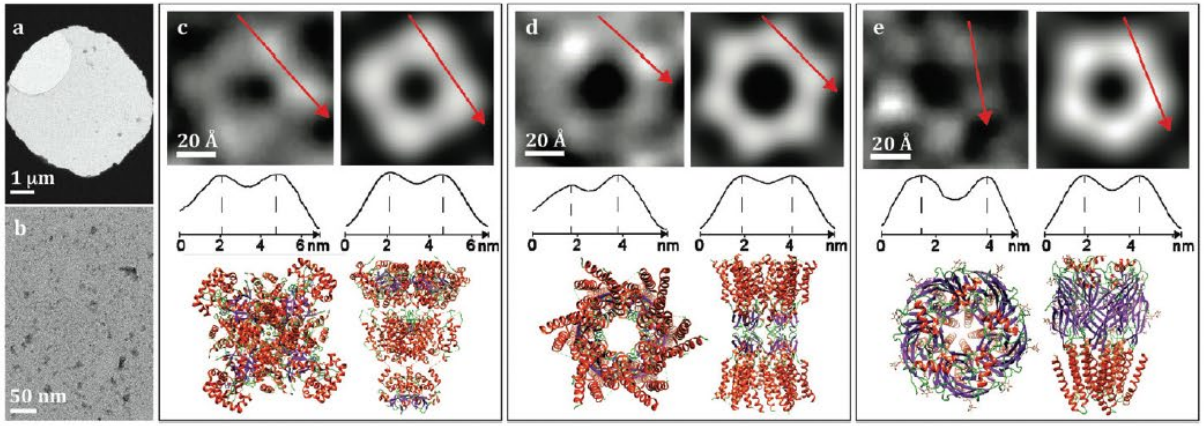

Fig. 6 TEM images of channels and receptors. Survey TEM imaging at very low (a) and intermediate (b) magnification of the suspended protein membrane. (c–e) Sequence of TEM image details, TEM image simulations, corresponding contrast profiles, and plots of structural models used for the simulations: K-channel[22] (PDB file: 3LNM) (c), Ca Gap Junction[23] (PDB file: 5ERA, d), and GABA[24] (PDB file: 4COF, e). The simulated defocus in c–e is 1 μm.

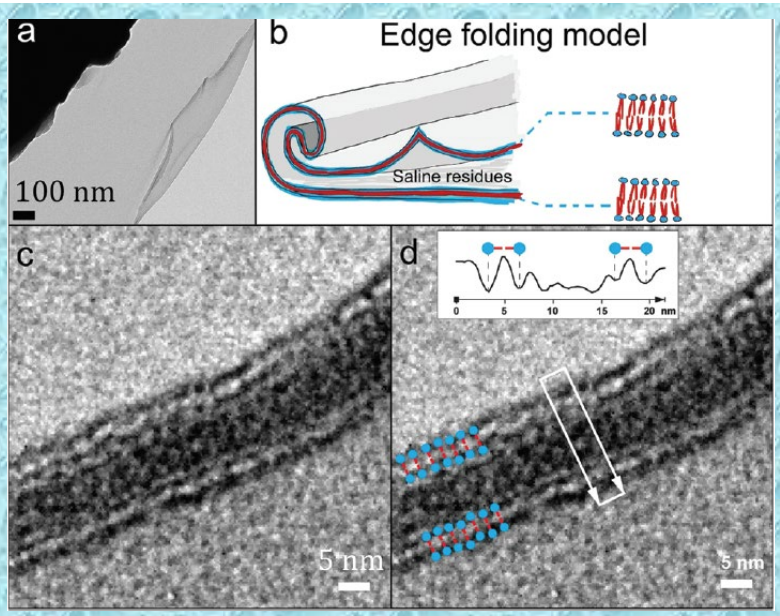

Fig. 8 Membrane cross-section analysis. The TEM cross-section of a membrane that appears broken and partially folded on itself is reported in (a). In the art style draft (b), folding is further schematized: the phospholipid bilayer is highlighted, and the polar head region and the hydrophobic tail region are represented in blue and in red respectively. In (c) and (d), high-magnification TEM cross-section image and metrology of the neuronal membrane bilayers from the contrast curve are reported.

Multiple probe measurements (TEM+AFM+nanoRaman)

RESEARCH ARTICLE

small methods
www.small-methods.com

Direct Visualization and Identification of Membrane Voltage-Gated Sodium Channels from Human iPSC-Derived Neurons by Multiple Imaging and Light Enhanced Spectroscopy

Manola Moretti, Tania Limongi, Claudia Testi, Edoardo Milanetti, Maria Teresa De Angelis, Elvira I. Parrotta, Stefania Scalise, Gianluca Santamaria, Marco Allione, Sergei Lopatin, Bruno Torre, Peng Zhang, Monica Marini, Gerardo Perozziello, Patrizio Candeloro, Candido Fabrizio Pirri, Giancarlo Ruocco, Giovanni Cuda, and Enzo Di Fabrizio**

In this study, transmission electron microscopy atomic force microscopy, and surface enhanced Raman spectroscopy are combined through a direct imaging approach, to gather structural and chemical information of complex molecular systems such as ion channels in their original plasma membrane. Customized microfabricated sample holder allows to characterize Na_v channels embedded in the original plasma membrane extracted from neuronal cells that are derived from healthy human induced pluripotent stem cells. The identification of the channels is accomplished by using two different approaches, one of them widely used in cryo-EM (the particle analysis method) and the other based on a novel Zernike Polynomial expansion of the images bitmap. This approach allows to carry out a whole series of investigations, one complementary to the other, on the same sample, preserving its state as close as possible to the original membrane configuration.

1. Introduction

Ion channels are membrane proteins playing a crucial role in cell growth and proliferation, neurotransmission, heart and muscle contraction, immune response, and water balance. Due to their broad distribution in cells and their critical role in physiological and pathological processes, ion channels represent important and potential targets for drug discovery and pharmacological safety. They have been associated with different genetic diseases, referred as channelopathies, some of which account for genetic human epilepsies.[1–6] Although the characterization of plasma membranes and ion channels

Overview of the experimental procedure protocol

ADVANCED SCIENCE NEWS
www.advancedsciencenews.com

small methods
www.small-methods.com

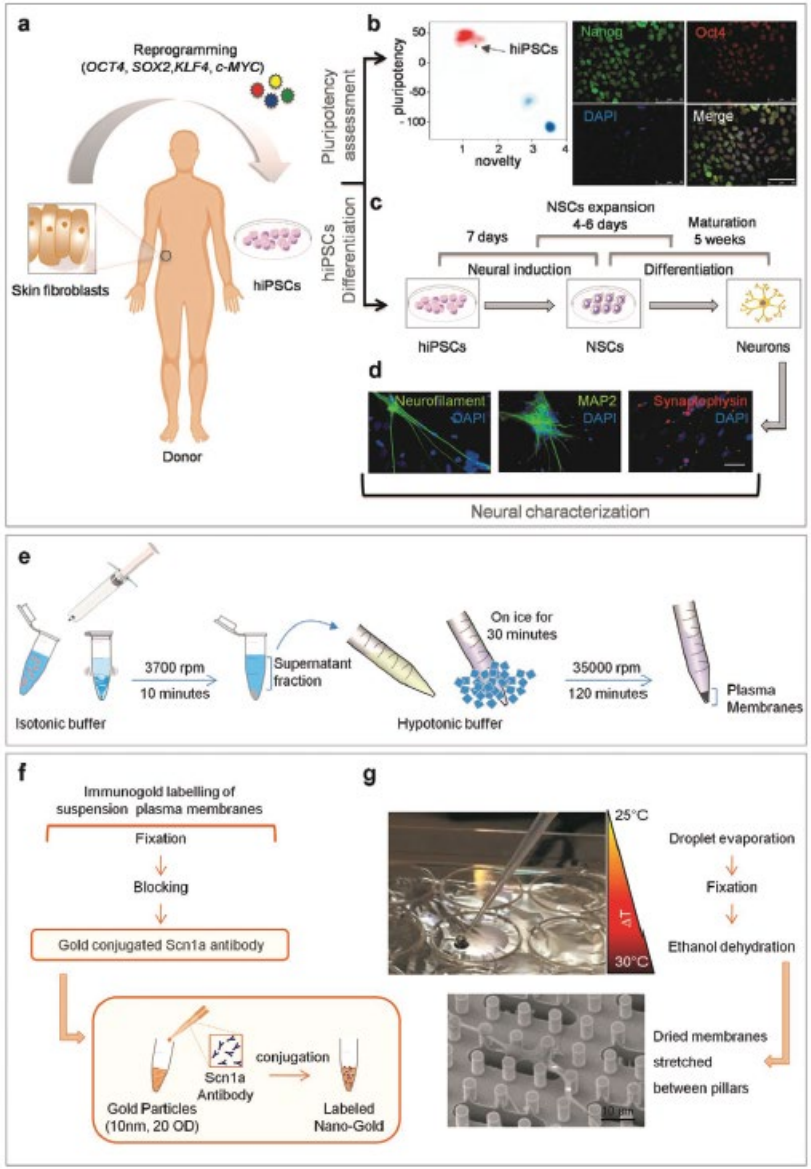

Multiple probe measurements

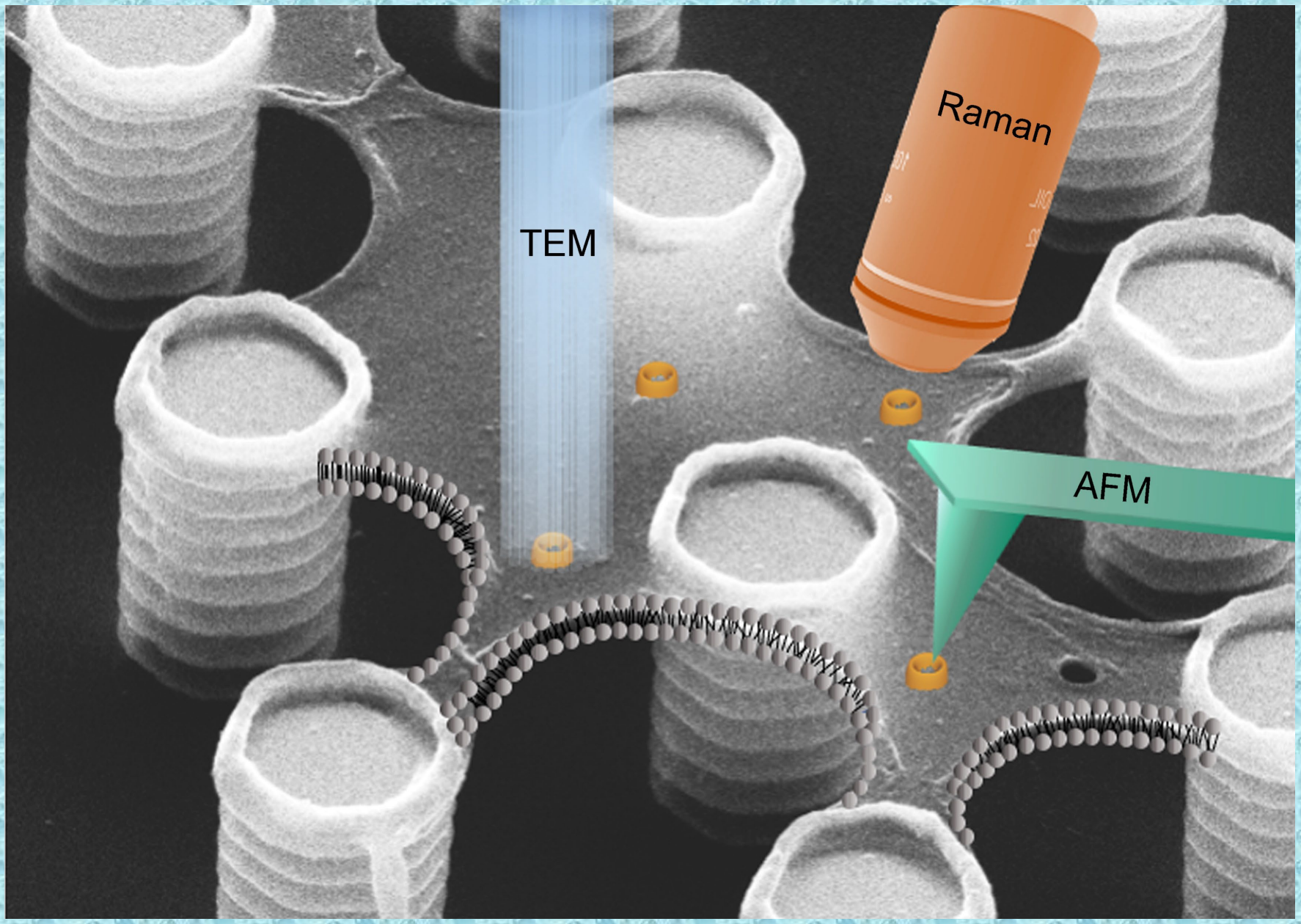

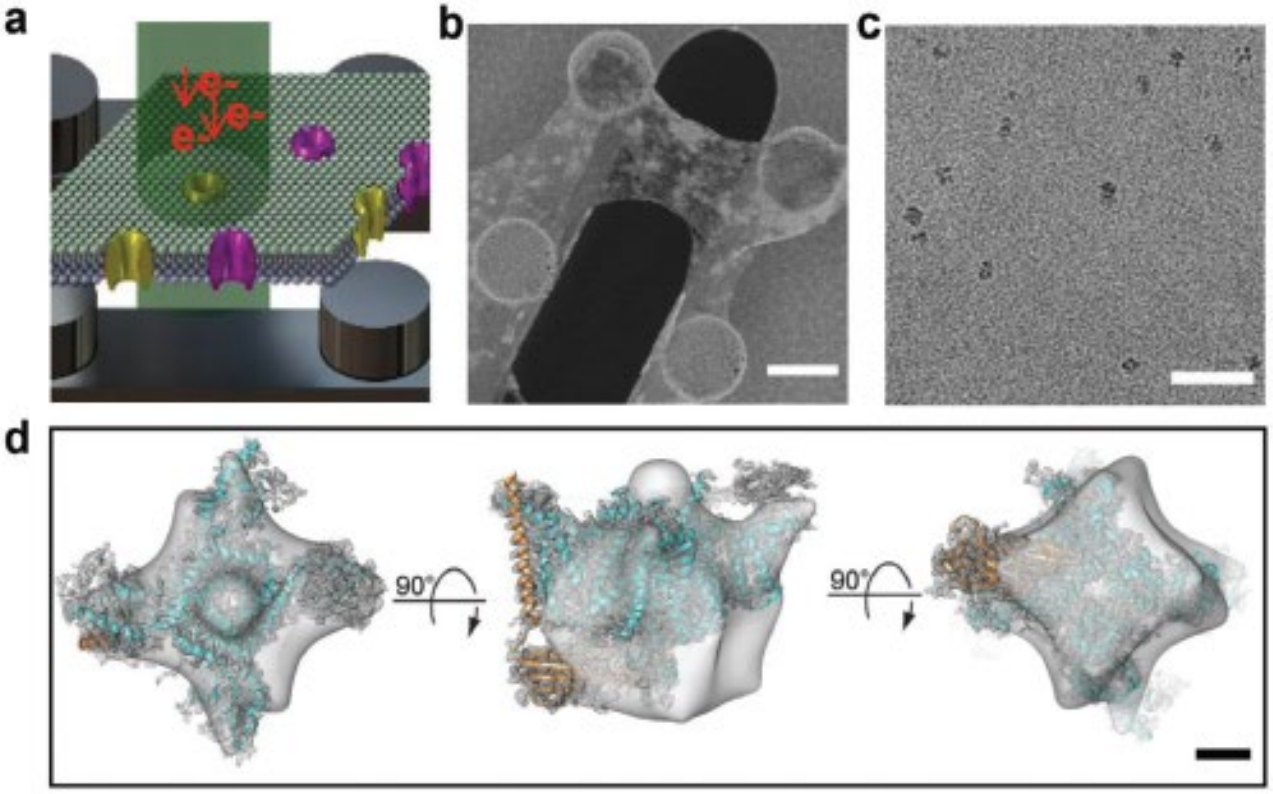
a
b
c
d
90°
90°

TEM imaging

ADVANCED SCIENCE NEWS
www.advancedsciencenews.com

small methods
www.small-methods.com

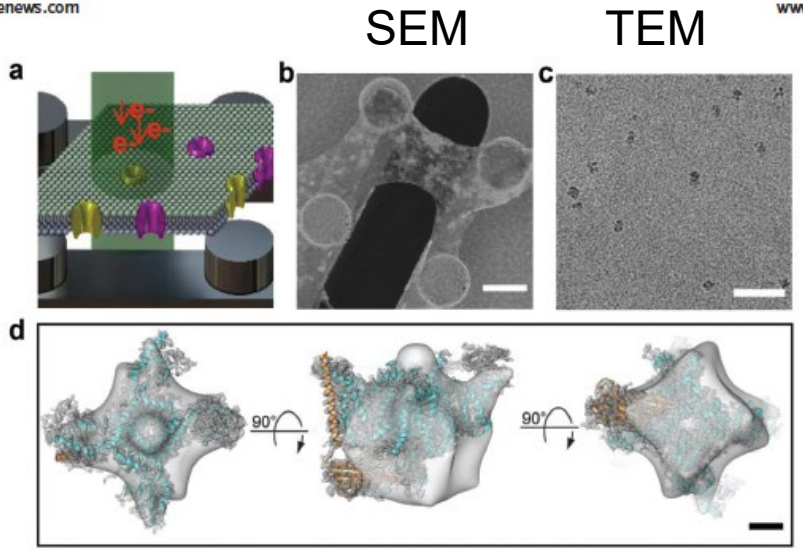

Scale bar 30 nm

Scale bar 20 Angstrom

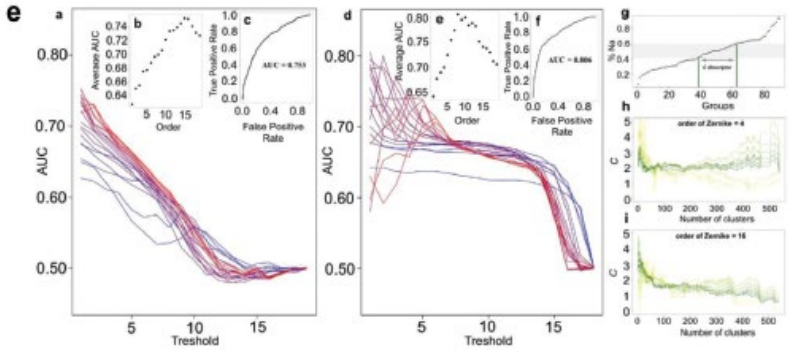

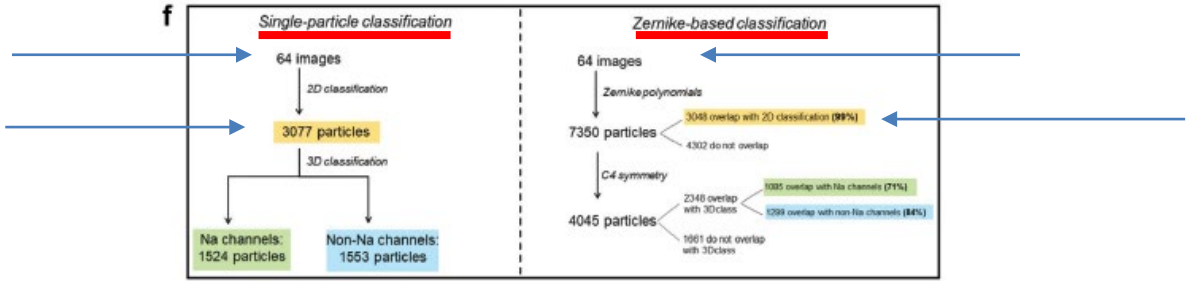

AFM measurements

ADVANCED SCIENCE NEWS
www.advancedsciencenews.com

small methods
www.small-methods.com

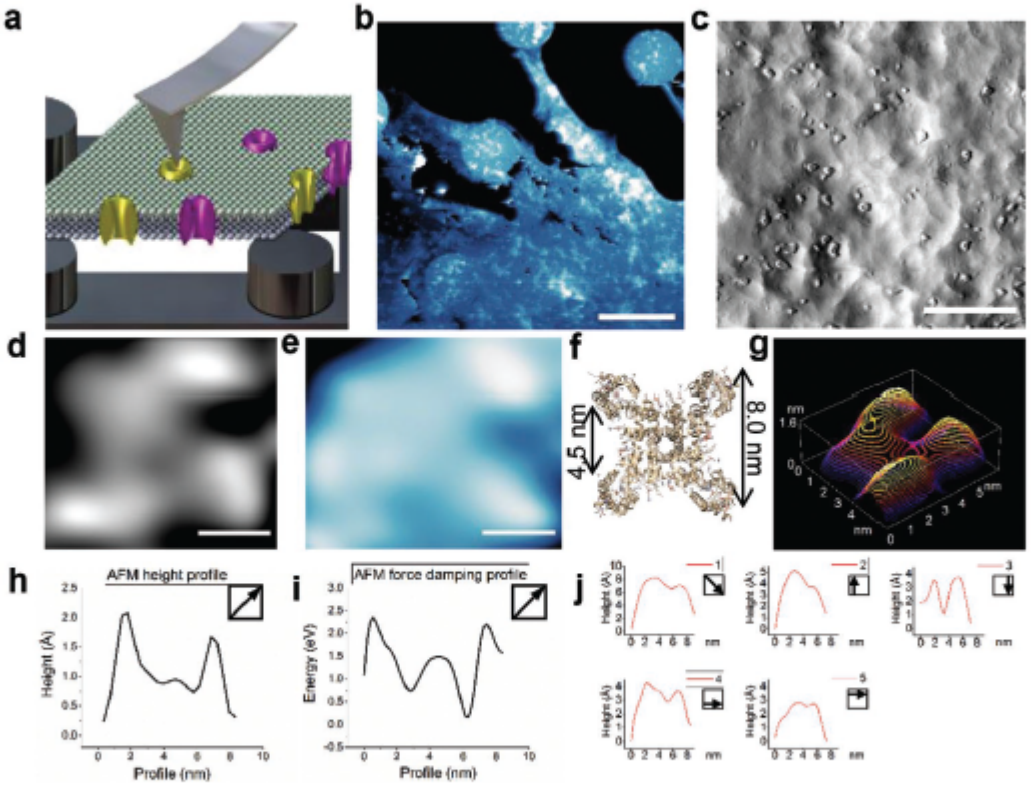

Figure 2. AFM imaging of the Na_v channel. a) Sketch of the sample characterization method where the suspended plasma membrane is investigated by AFM. b) AFM height topography of a large area of the suspended neuronal plasma membrane over the SHS. Scale bar 5 µm. c) AFM amplitude signal of the suspended neuronal membrane where different features can be localized. Scale bar 100 nm. d,e) AFM height topography and AFM force damping map of a single Na_v channel respectively. Scale bar 2 nm. f) Molecular graphic plotted with Chimera of the Na_v channel according to PDB file 5EK0 with inner and outer lengths indicated. g) 3D surface plot of topography in d, with isolines of 1 Å step size. h,i) AFM height diagonal profile and AFM force damping diagonal profile of the contrast $\Delta E_{protein}$ of the putative Na_v channel, of respectively (d) and (e). j) Profiles drawn in the AFM topography image in d, where the arrows in the inset squares indicate the position and direction of each plotted profile.

Raman spectroscopy of Na Channel

with antibody gold labeled

ADVANCED SCIENCE NEWS
www.advancedsciencenews.com

small methods
www.small-methods.com

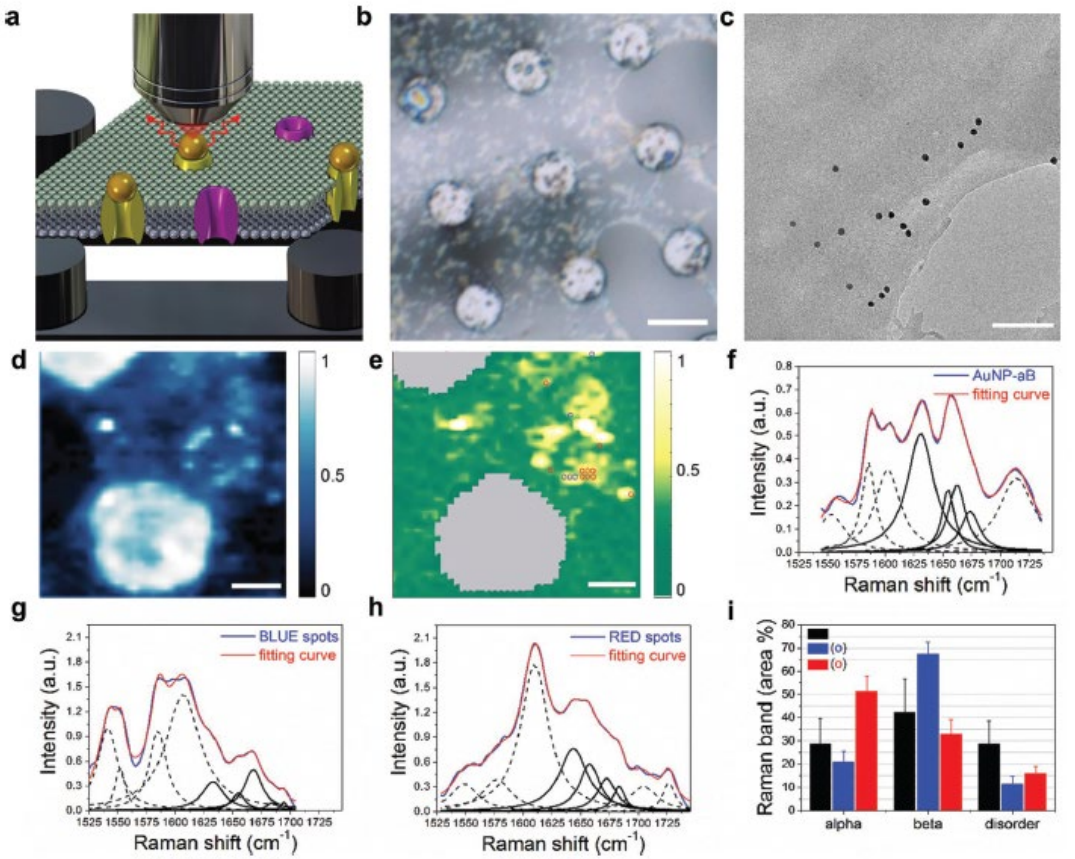

Figure 3. Raman spectroscopy of the immunogold labeled SCN1a subunit of the Na_v channel on the suspended neuronal membrane. a) Sketch of the Raman spectroscopy imaging setup, where a single Na_v channel, specifically tagged with a gold nanoparticle, is imaged. b) Optical image of a portion of the suspended neuronal membrane on the SHS. Scale bar 5 µm. c) TEM image of the neuronal membrane with gold nanoparticles tagging specifically the SCN1a subunit by immuno-labeling. Scale bar 100 nm. f–h) Raman measurements (blue curve), fitting curves (red), and specific single curves used to describe the secondary structure regions in the Amide I range (full black) for the gold nanoparticles with covalently linked antibody (AuNP-aB), and for the immuno-gold construct tagging the Na_v channels in different docking regions, indicated as blue and red spots in e, respectively (for an explanation of dotted lines fitting curves see methods). d) Optical signal arising from the nano-gold construct on the suspended neuronal membrane. Scale bar 2 µm. e, Raman spectroscopy imaging. The intensity color scale relates to the area in the range of 1500–1750 cm^{-1} (Amide I region): blue and red circles indicate the 2 sub-populations in g and h, according to PCA analysis. Scale bar 2 µm. i) Histogram of fitting results relative to α, β, and disordered secondary structures in the Amide I region for the red spots spectra (red), blue spots spectra (blue), and reference gold nanoparticles antibody tagged spectra (black).

COMMUNICATIONS BIOLOGY

ARTICLE

https://doi.org/10.1038/s42003-020-01187-7 OPEN

A droplet reactor on a super-hydrophobic surface allows control and characterization of amyloid fibril growth

Peng Zhang[1], Manola Moretti[1], Marco Allione[1], Yuansi Tian[2], Javier Ordonez-Loza[3], Davide Altamura[4], Cinzia Giannini[4], Bruno Torre[1], Gobind Das[5], Erqiang Li[6], Sigurdur T. Thoroddsen[2], S. Mani Sarathy[3], Ida Autiero[7,8], Andrea Giugni[1], Francesco Gentile[9], Natalia Malara[10], Monica Marini[11] & Enzo Di Fabrizio[1,11]✉

Whole Process for protein fibril formation

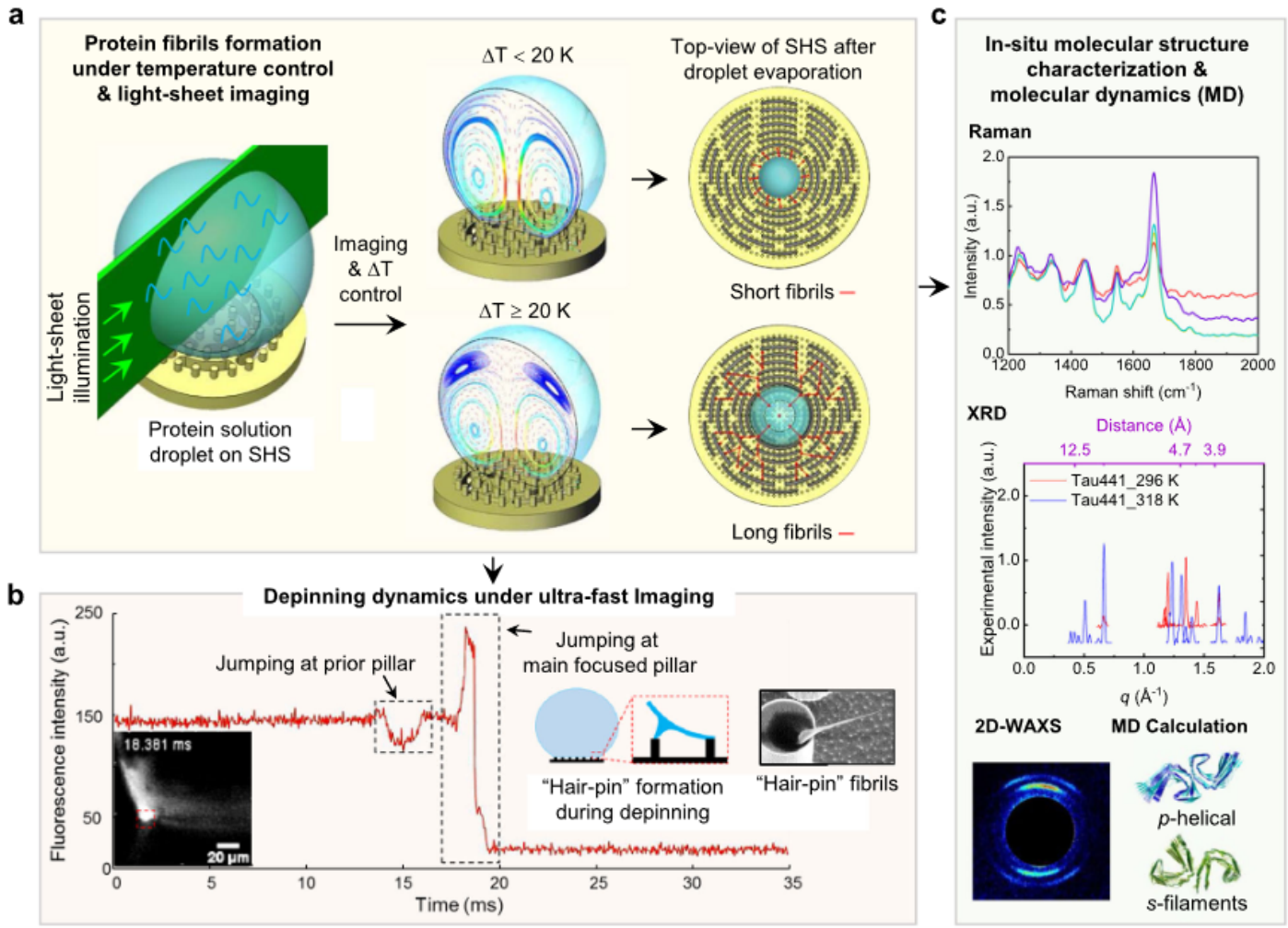

Fig. 1 Scheme of the whole process from protein fibrils formation in droplet with confined convective flow field control and study of droplet contact line depinning dynamics to protein fibrils molecular structure characterizations. a Protein fibrils formation with temperature gradient (ΔT) controlled confined convective flow field in droplet on SHS. **b** Droplet contact line depinning dynamics study with ultra-fast imaging. **c** In situ molecular structure characterizations of protein fibrils with Raman, XRD, 2D-WAXS, and molecular dynamics (MD) calculation.

Four convective lobes at 20 °C gradient temperature (ΔT=20 °C respect to the environment)

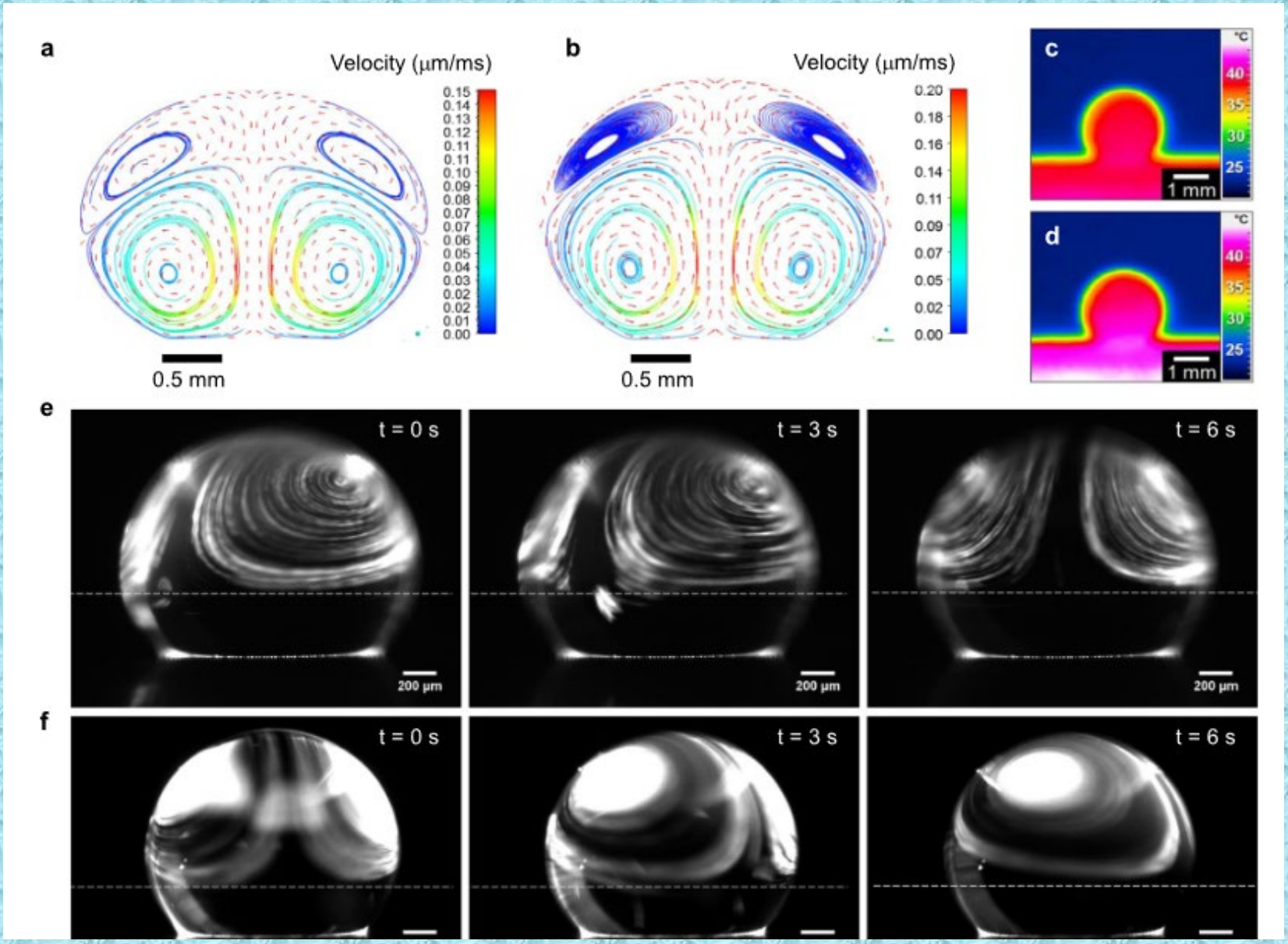

SMILEs

Confined Convective Flow in Droplet on SHS

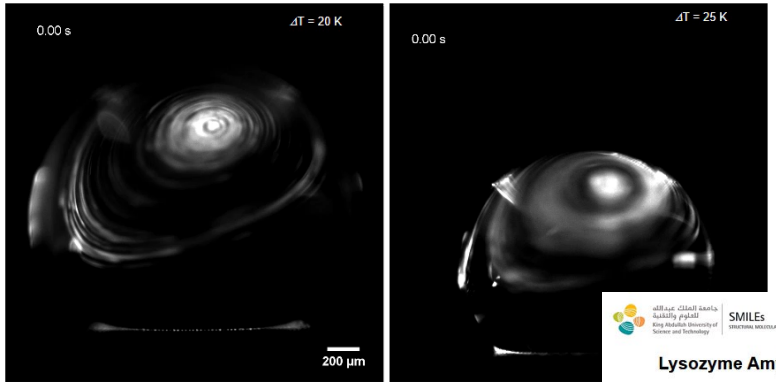

Video S2. Experimental confined convective flow in droplet on SHS with ΔT = 20 K and .

Light sheet imaging

SMILEs

Lysozyme Amyloid Fibrils Growth Driven by Confined Convective Flow in Droplet

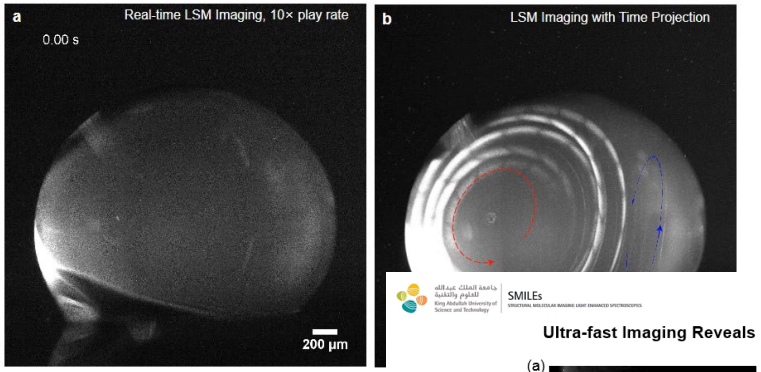

Video S3, light-sheet images of lysozyme amyloid fibrils (LAF) in aqueous solu
real-time movie. **b**, convection trajectories of LAF in droplet. The closed loops i
the circulation direction. In general, the convection lop is pairwise, as we showe
on the "back-side" of the droplet as shown with blue line.

SMILEs

Ultra-fast Imaging Reveals Droplet Depinning Dynamics

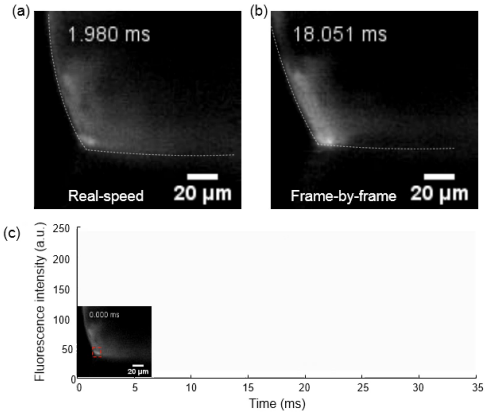

Ultra-fast imaging depinning dynamics of droplet with fluorescence bead on SHS. (a) Real-speed images of the droplet depinning process; (b) frame-by-frame playing of the depining process; (c) Fluorescence intensity measurements in contact area. The fluorescence images were filtered with a notch filter (533 nm) and acquired with an ultra-fast camera (Phantom V2511) at 30 K fps by Leica lens (2.0×9.2×1.6×).

Fast camera imaging

30,000 frame-per-second (fps) ➔

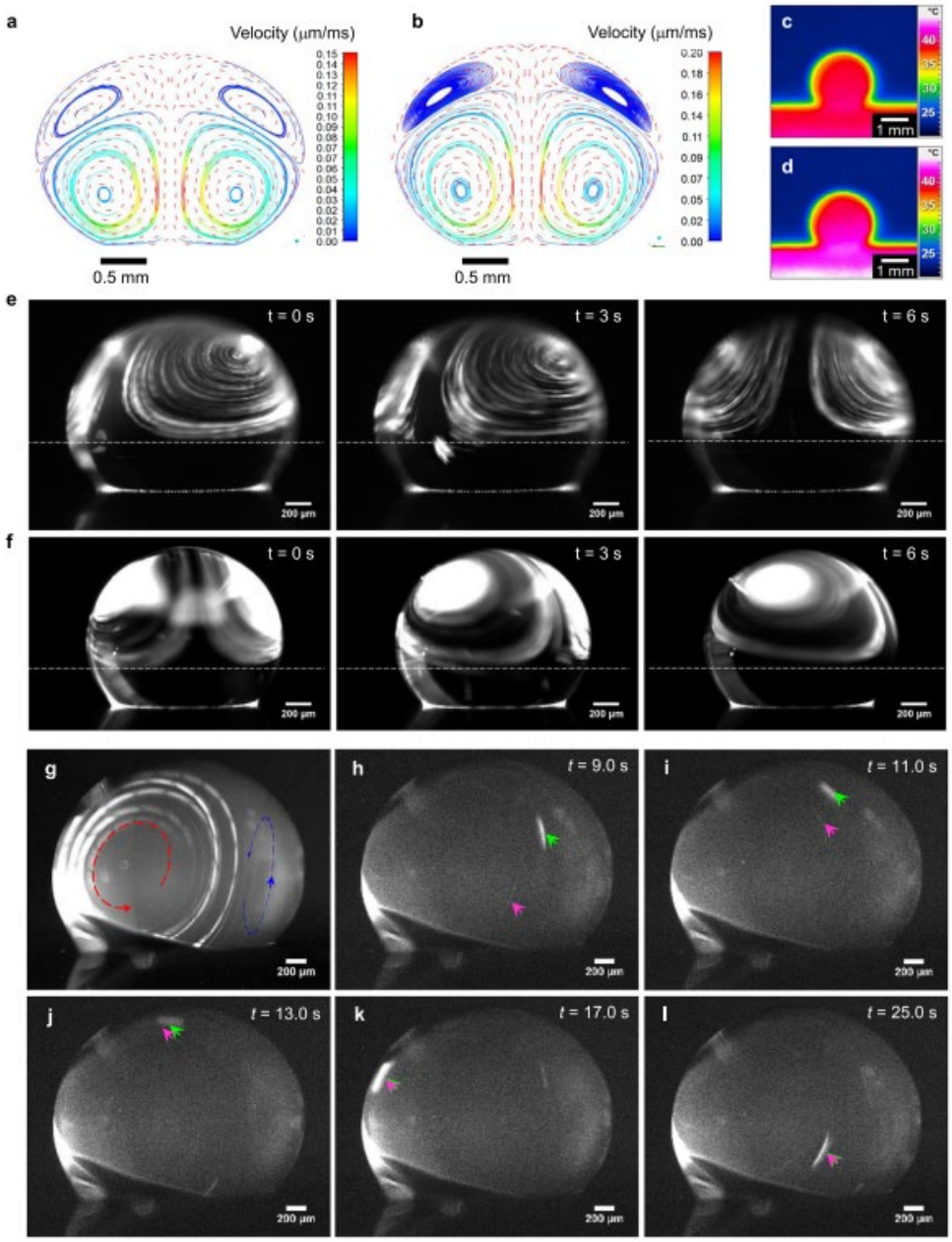

Fig. 2 Simulated and experimental convective flow in water droplet on SHS for molecules driven. a Simulated convective flow field in droplet driven by buoyancy force at $\Delta T = 20$ K and at **b**, $\Delta T = 25$ K. **c** thermal imaging of water droplet on hotplate at $\Delta T = 20$ K and at **d**, $\Delta T = 25$ K. **e** Experimental convective flow at $\Delta T = 20$ K and at **f**, $\Delta T = 25$ K. **g** Amyloid fibrils driven by confined convection flow in droplet at $\Delta T = 25$ K. The closed loops indicate the total circulation of in droplet and the red arrow indicates the circulation direction. In general, the convection loop is pairwise, as we showed previously. Here one of the loop is observed clearly, and the paired one is on the "back-side" of the droplet as shown with blue line. **h–l** Real-time tracking of a typical amyloid fibrils assembling and growing driven by confined convective flow. Time stamps indicate the different frames of the imaging flow.

Fibril aggregation

The molecule trajectories are not disturbed by the substrate, thus forming a persistent convection loop. In addition, by taking advantage of the real-time imaging system, two representative fibril aggregates (Fig. 2h–l, the green and magenta arrowed), were tracked in the convective flow. Initially, these two different sized fibrils migrate independently at large relative distance (Fig. 2h, Supplementary Note 5, Supplementary Movie 3 and Supplementary Fig. 11). Due to the convective flow loops, these two fibrils are driven closer and closer (Fig. 2i, j) until they aggregate together and form one single larger assembly (Fig. 2k, l)

Tau protein formation: wires and hairpins

(stationary and out of equilibrium formation)

stationary

Out of equilibrium

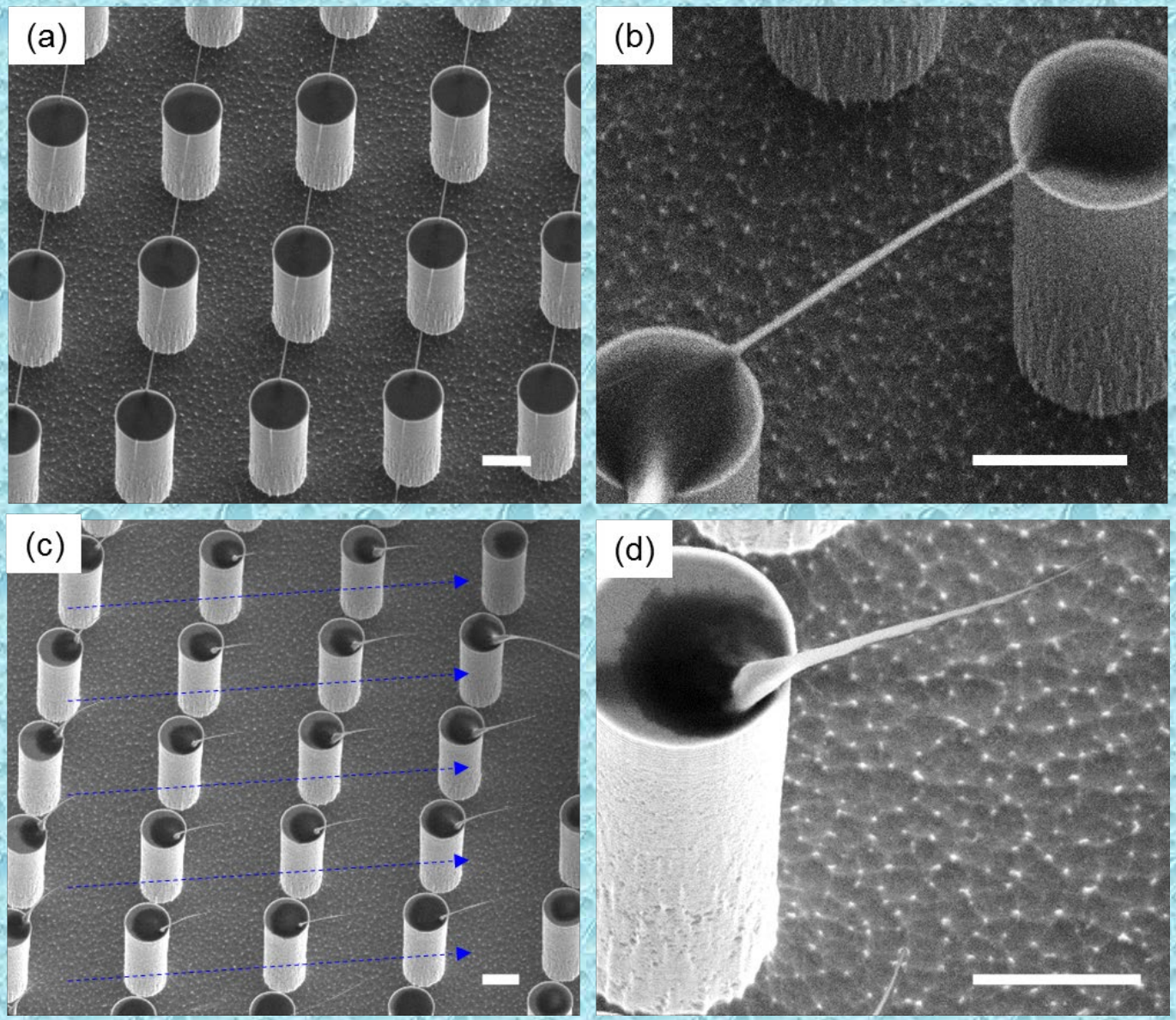

De-pinning imaging with fast camera

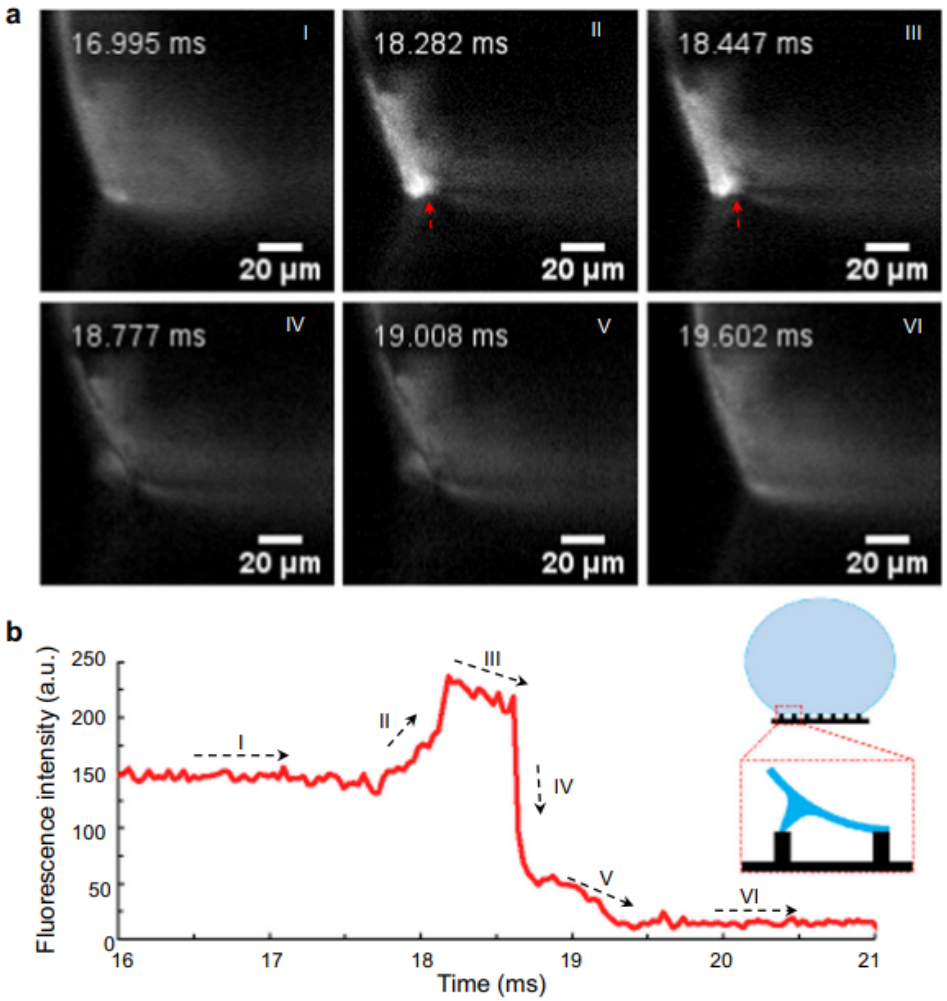

Fig. 4 Images of the droplet contact line receding on micro-pillar arrays with ultra-fast imaging technique. a Six key steps during the depining process. I, steady-state before depinning; II, transient-state during depinning by forming stretched capillary bridge between outer pillars and droplets; III, capillary bridge stretching and moving; IV, capillary bridge break and disappear, contact line pinning to new area; V, disturbance from posterior pillar; VI, steady-state after depinning. **b** Fluorescence intensity tracking corresponding to the six processes (I–VI) and the inner schematic drawing of the capillary bridge. The fluorescence images are acquired with an ultra-fast camera (Phantom V2511) at 30,000 fps by Leica lens (2.0 × 9.2 × 1.6×).

Tau441 full length fibrils on SHS characterized with XRD, WAXS, and polarized Raman

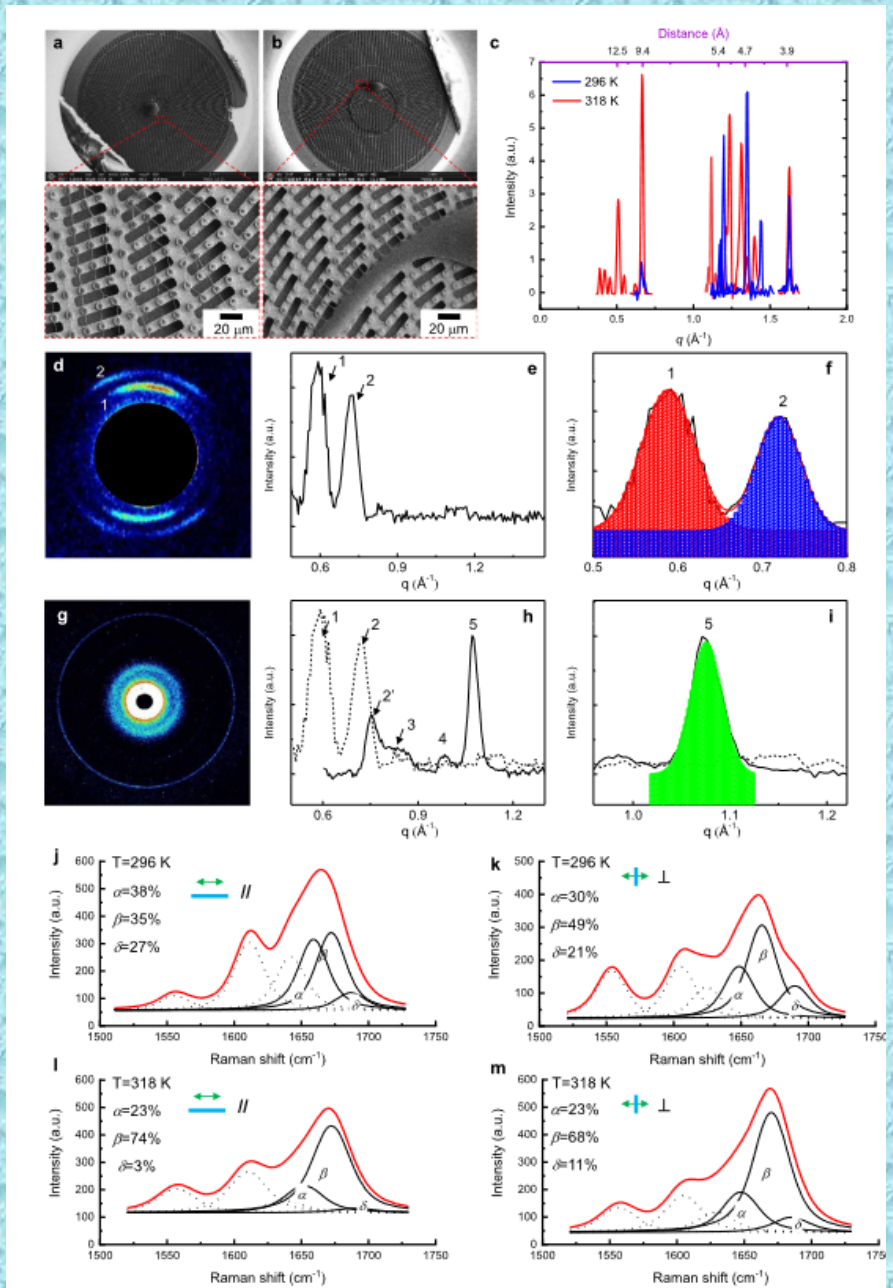

X-Ray

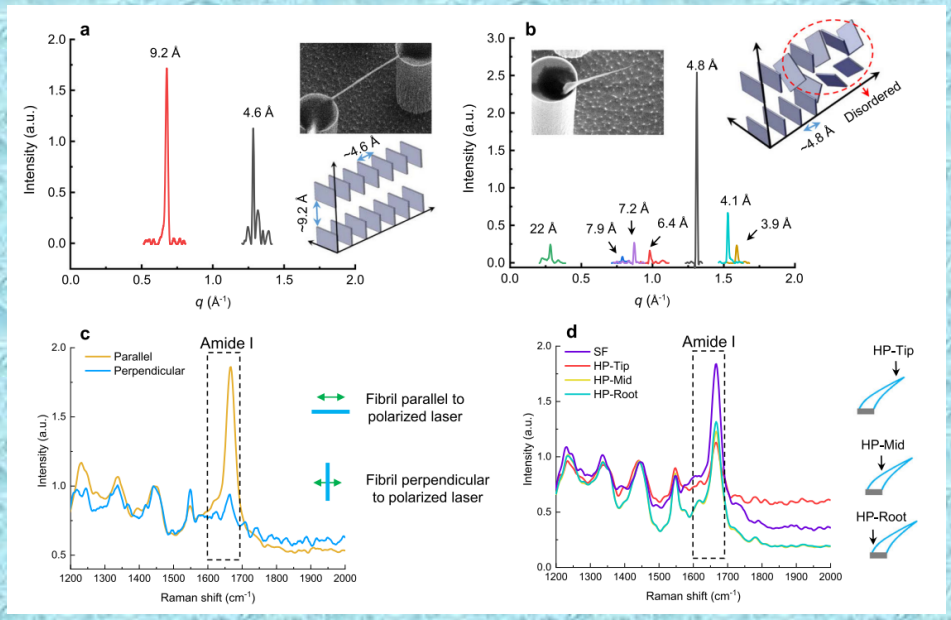

Polarized Raman

Fig. 5 Molecular structure characterizations of lysozyme amyloid fibrils. a XRD characterization of lysozyme amyloid fibrils suspended between two pillars. b XRD characterization of hair-pin (HP) type lysozyme amyloid fibrils. c Polarized Raman spectroscopy of SF. Parallel and perpendicular indicate the fibril is parallel and perpendicular (right panel diagrams) to the incident laser's polarization respectively. d Polarized Raman spectroscopy of SF and HP type lysozyme amyloid fibrils at different positions (tip position, HP-Tip; middle position, HP-Mid; root position, HP-Root)

Selected results #4

Science Advances | AAAS
SIGNIFICANT RESEARCH, GLOBAL IMPACT

Sci Adv. 2015 Sep; 1(8): e1500487. PMCID: PMC4643778
Published online 2015 Sep 4. doi: 10.1126/sciadv.1500487

Detection of single amino acid mutation in human breast cancer by disordered plasmonic self-similar chain

Maria Laura Coluccio,[1] Francesco Gentile,[1,2] Gobind Das,[3] Annalisa Nicastri,[1] Angela Mena Perri,[1] Patrizio Candeloro,[1] Gerardo Perozziello,[1] Remo Proietti Zaccaria,[4] Juan Sebastian Totero Gongora,[5] Salma Alrasheed,[3] Andrea Fratalocchi,[5] Tania Limongi,[3] Giovanni Cuda,[1] and Enzo Di Fabrizio[1,3,*]

Author information ► Article notes ► Copyright and License information ►

Abstract

Go to:

Control of the architecture and electromagnetic behavior of nanostructures offers the possibility of designing and fabricating sensors that, owing to their intrinsic behavior, provide solutions to new problems in various fields. We show detection of peptides in multicomponent mixtures derived from human samples for early diagnosis of breast cancer. The architecture of sensors is based on a matrix array where pixels constitute a plasmonic device showing a strong electric field enhancement localized in an area of a few square nanometers. The method allows detection of single point mutations in peptides composing the BRCA1 protein. The sensitivity demonstrated falls in the picomolar (10^{-12} M) range. The success of this approach is a result of accurate design and fabrication

Self-similar nanoLens

Underlying physics of local field enhancement in efficient nanolens: Cascade enhancement

Courtesy by M. Stockman

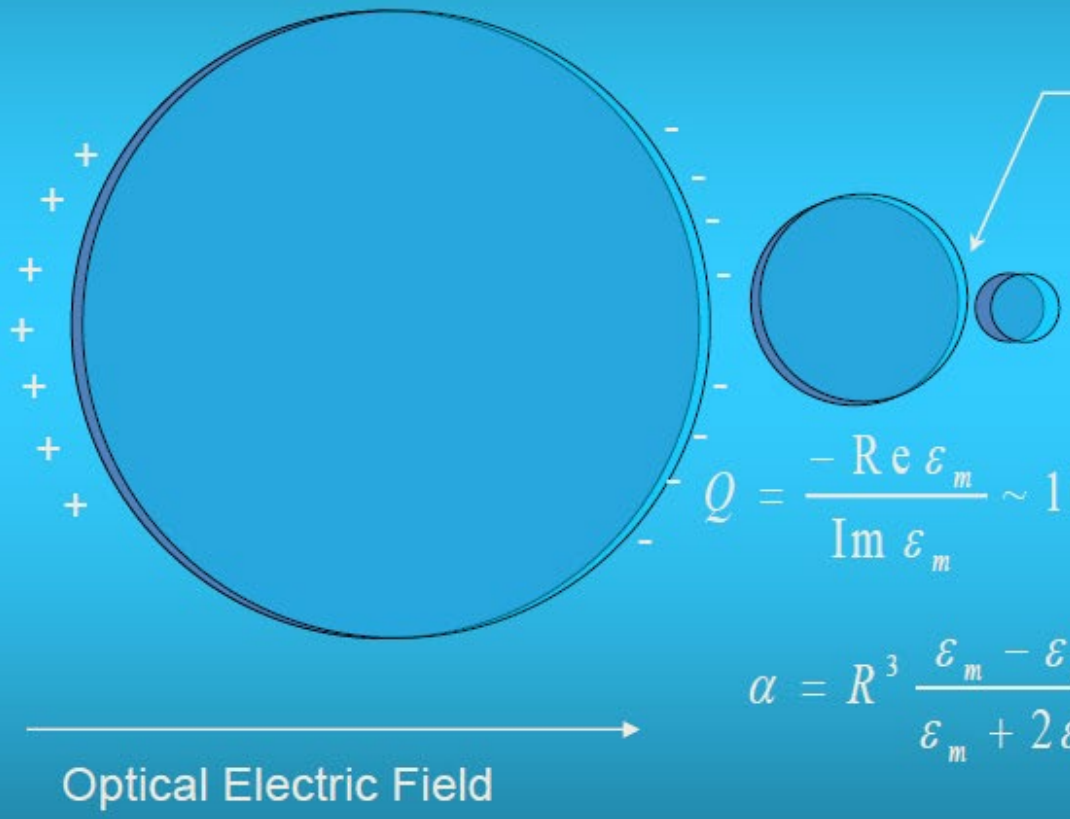

Giant local fields in the minimum gap: Nanoscale localization of optical energy

$$Q = \frac{-\mathrm{Re}\,\varepsilon_m}{\mathrm{Im}\,\varepsilon_m} \sim 10-100$$

$$\alpha = R^3 \frac{\varepsilon_m - \varepsilon_d}{\varepsilon_m + 2\varepsilon_d}$$

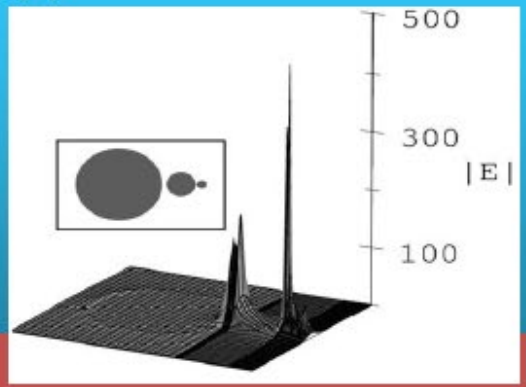

Local field in the sphere ~Q (quality factor)
The resonance of the bigger sphere not pertubed by smaller sphere (α ~Volume)
The next smaller sphere generates a local field enhanced by ~ Q^2

Effect of surface roughness

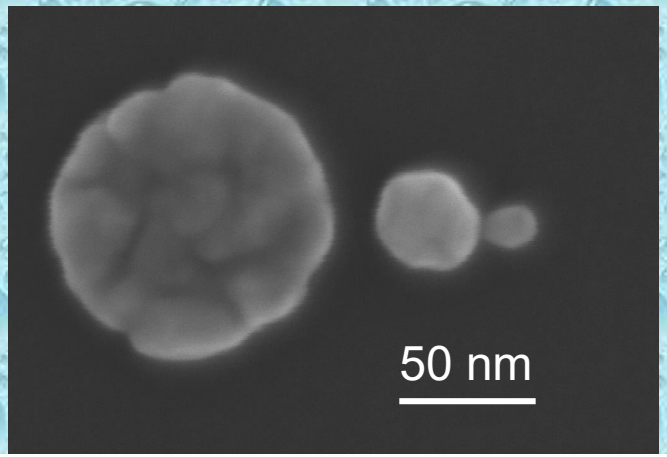

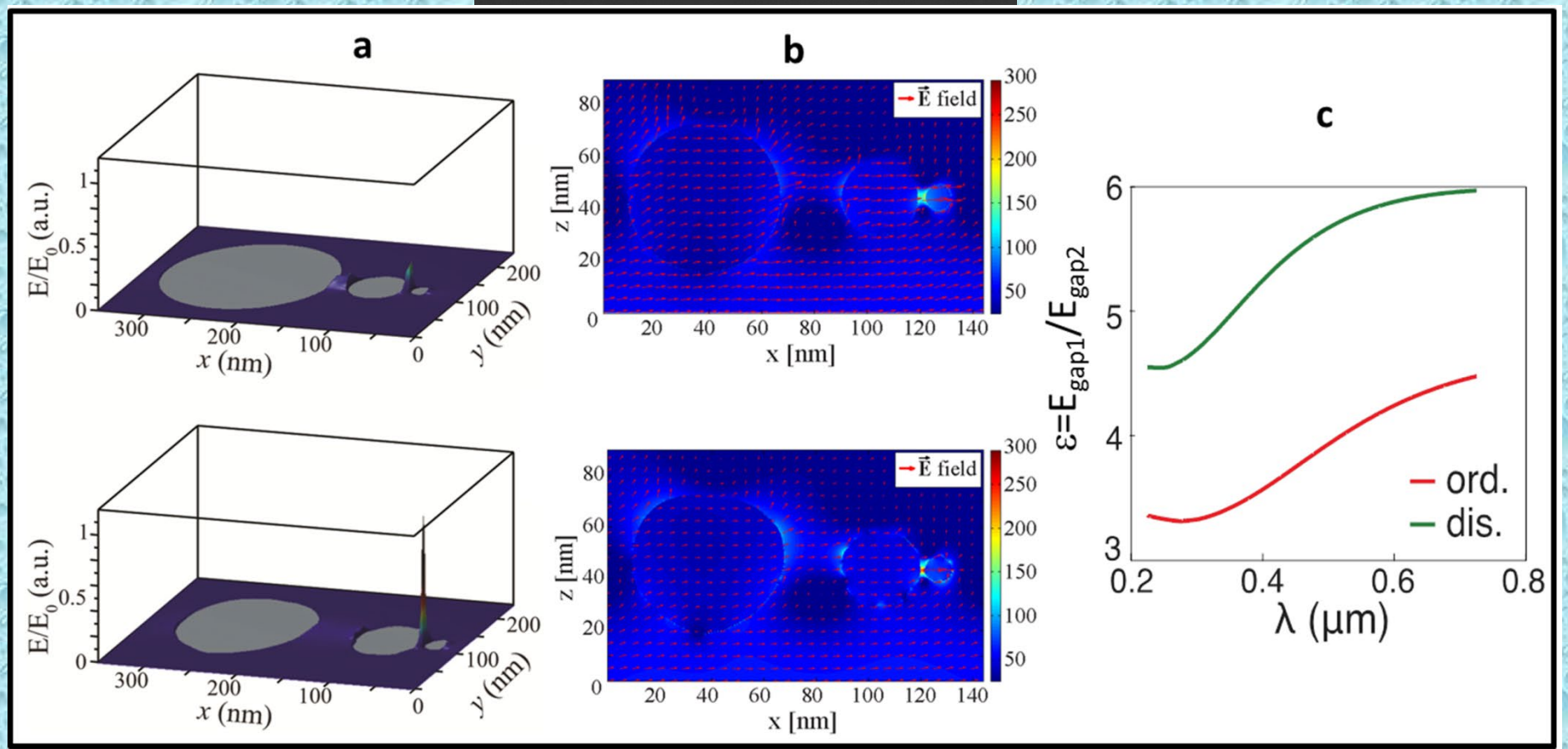

Localized hot spot and detection volume

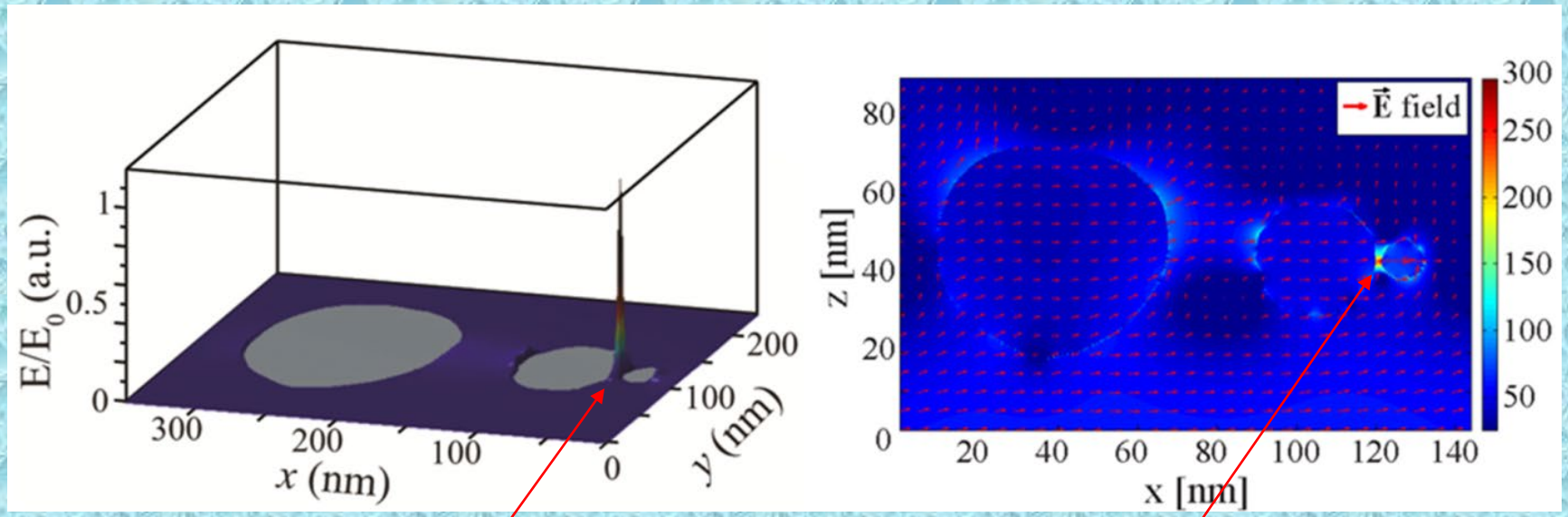

SERS sensitive volume
(outside of this volume,
no Raman effect)

SERS sensitive volume
(outside of this volume,
no Raman effect)

Fabrication process of the device

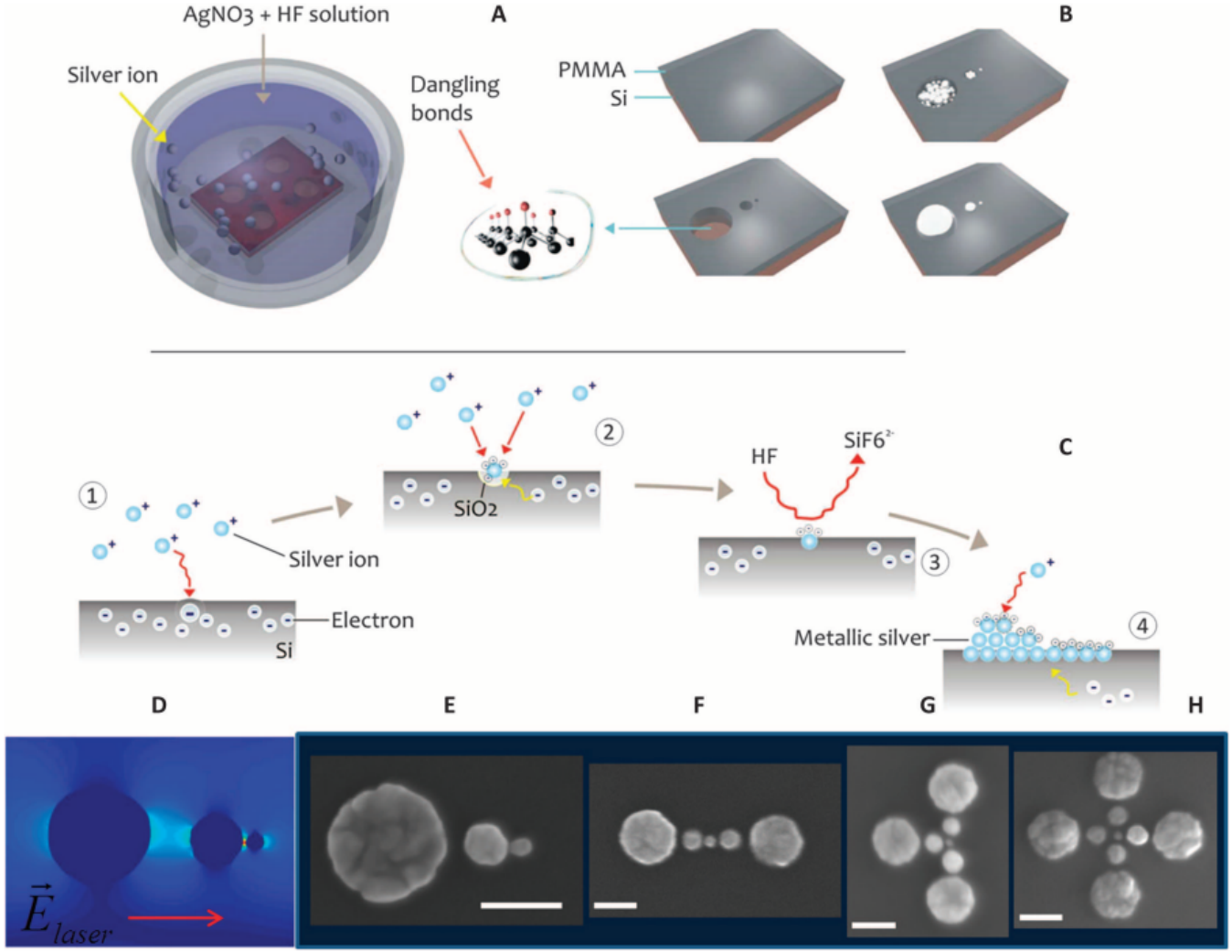

Fig. 2. Fabrication process of silver SSC. (**A**) After electron beam lithography and surface treatment with 2 M HF, the sample is immersed in HF/$AgNO_3$ aqueous solution, where Ag^+ is reduced to silver metal through a redox reaction chain. (**B**) In nanowells (reduction surface), silver growth follows a spherical symmetry and generates three spheres of appropriate diameter and interdistance. (**C**) Redox reactions inside a nanowell starting from the silicon surface. (**D**) SSC architecture and 2D map of electric field. Evidence of external laser polarization along the chain axis. The electric hotspot is localized in the smallest gap. (**E** to **H**) SEM images of silver SSCs and possible combinations in monomer, dimer, trimer, and tetramer. Scale bars, 50 nm. PMMA, polymethyl methacrylate.

Can highly localized hot spot be used for complex mixture analysis?

Our application: BRCA1 mutation with SERS in brest cancer

BRCT domain

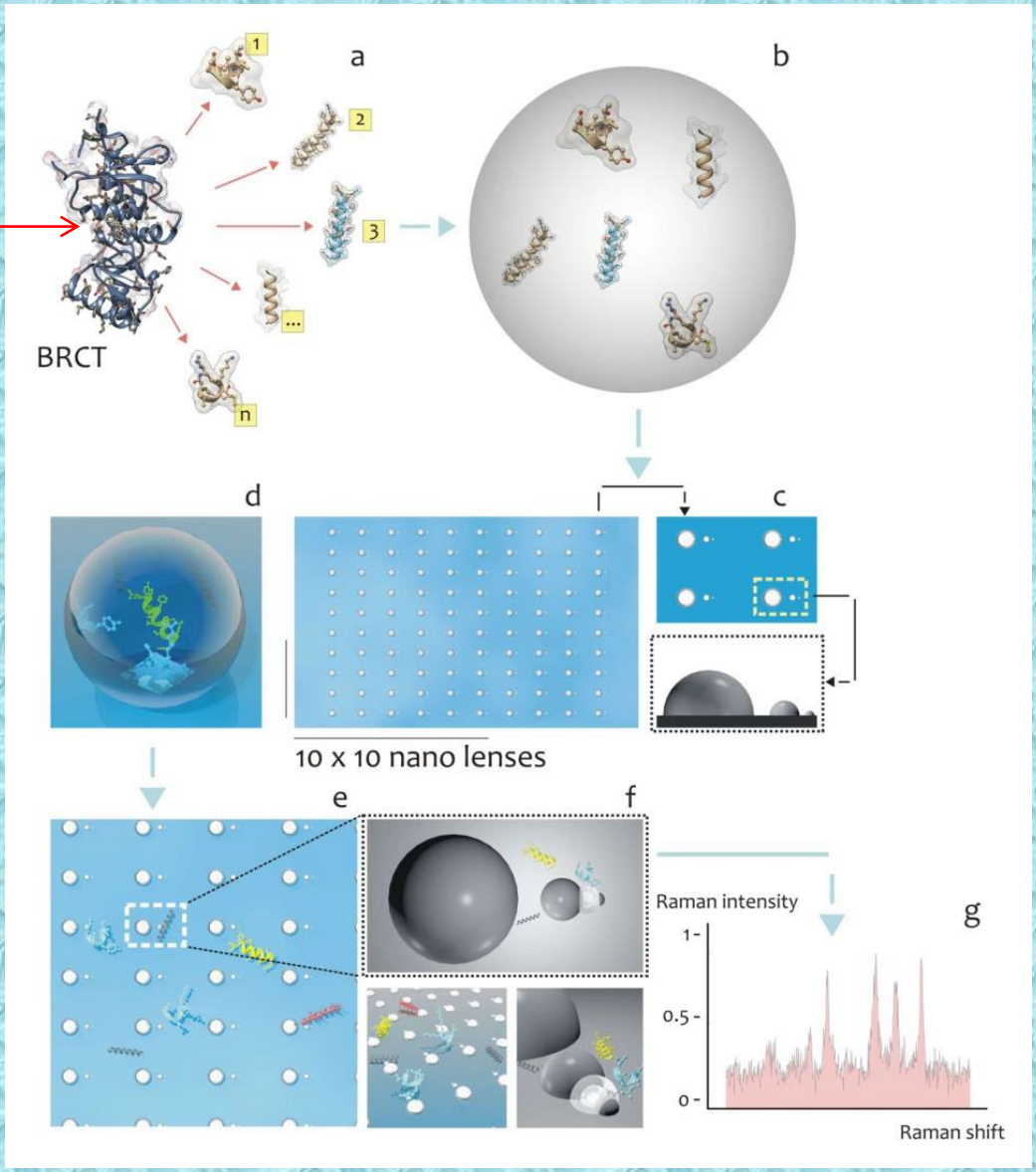

The matrix method

Figure S5 shows the position of the measurements on the 10×10 nanolens matrix in terms of measurement number (#) and row-column (r, c) coordinates of the matrix for the solution of synthetic peptides.

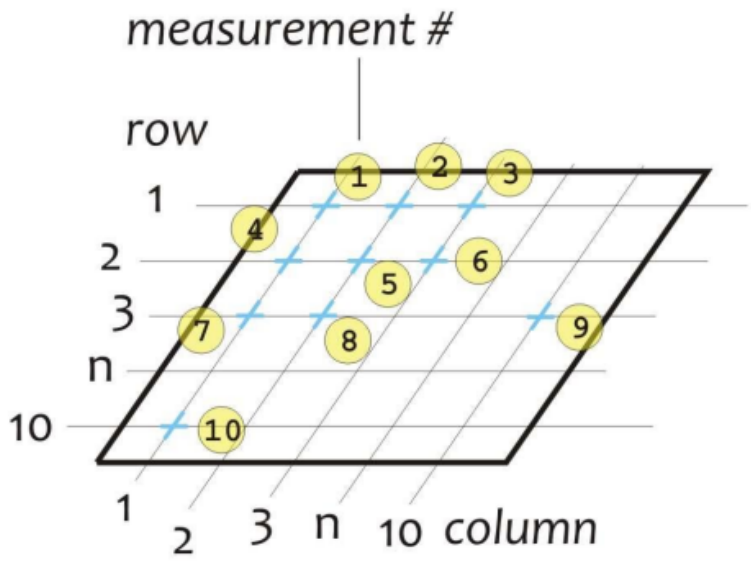

#	r, c
# 1	(1, 1)
# 2	(1, 2)
# 3	(1, 3)
# 4	(2, 1)
# 5	(2, 2)
# 6	(2, 3)
# 7	(3, 1)
# 8	(3, 2)
# 9	(3, 9)
# 10	(10, 1)

Figure S5: Nanolens matrix position of measurement points for the synthetic peptides solution.

Single pixel- fitting procedure and sub mixuture determination

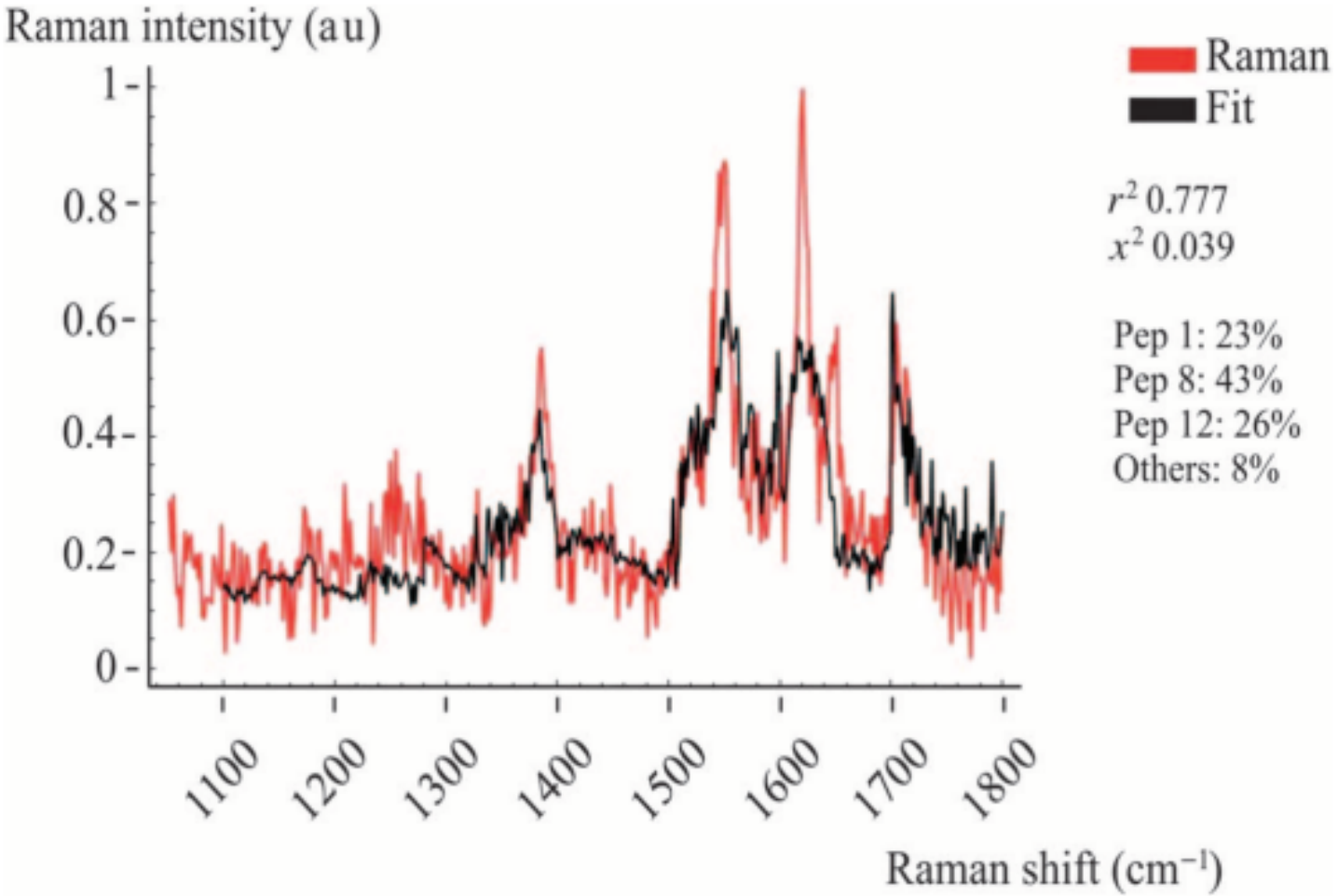

Fig. 4. Linear combination fitting procedure of peptide spectra. Raman spectra were collected in a representative pixel of the array. The fit gives a weighted composition of peptides 1, 8, and 12.

Chip architecture and readout

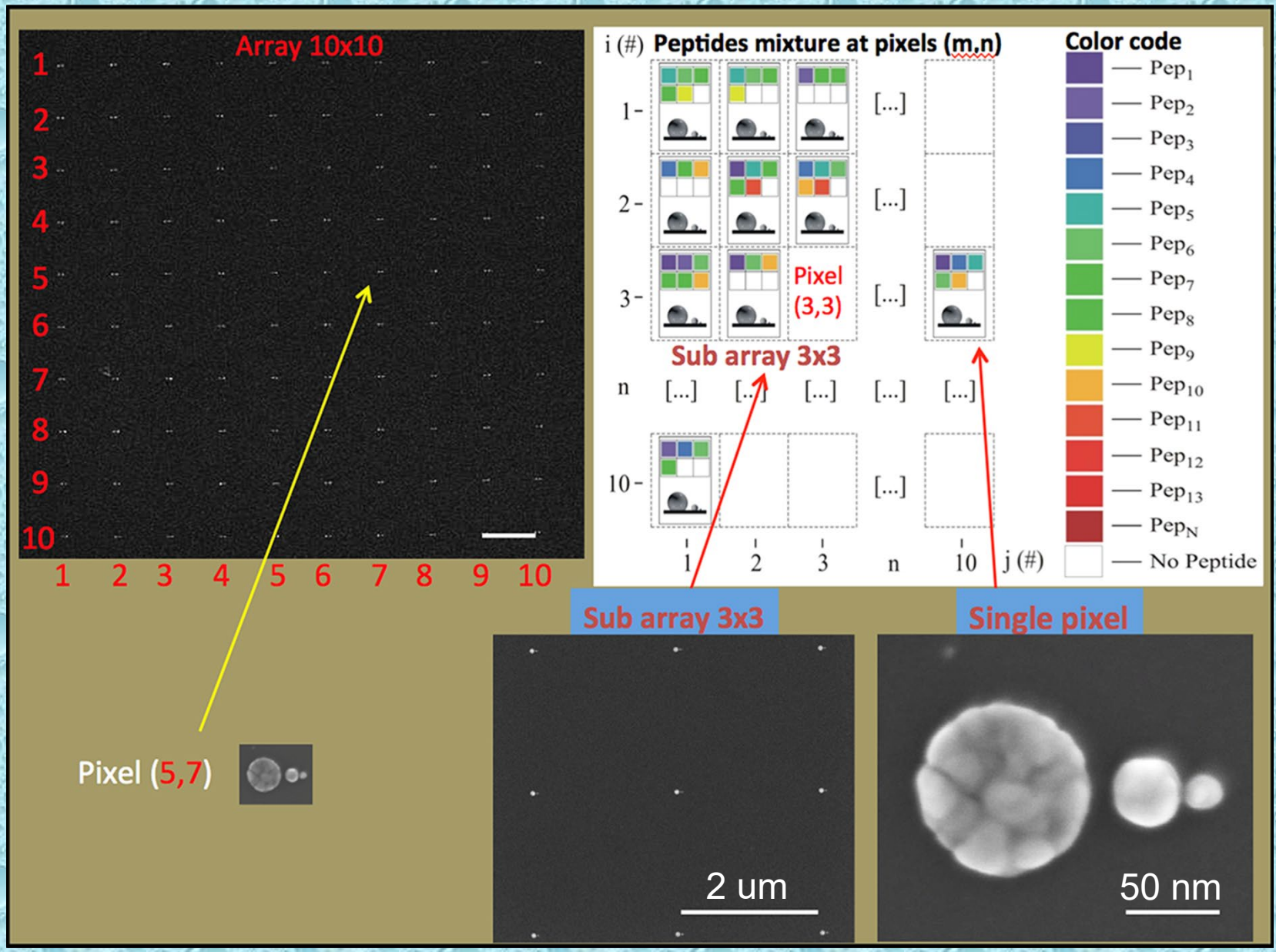

Detection of single amino acid mutation

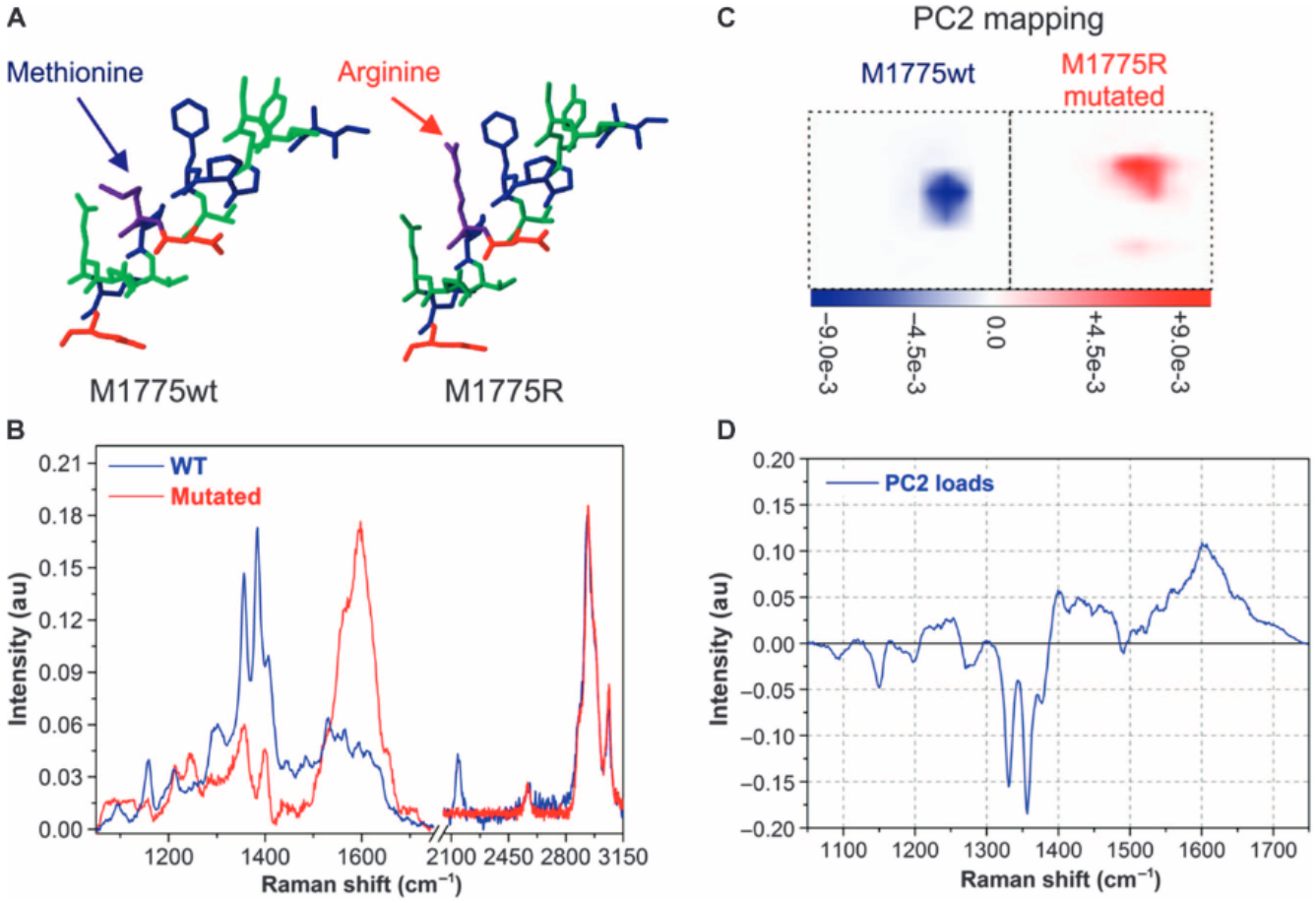

Fig. 6. Raman spectra of pure wild-type and mutated peptides. (**A** and **B**) Raman spectra (B) show a net difference between two peptides differentiated by only the exchange of one amino acid (A; a methionine with an arginine). These spectra constitute the base set for the fitting procedure. Their net difference allows identification of mutated peptides in the mixture. (**C** and **D**) The results of PCA are also shown: a 2D map of the PC2 coefficients of two pixels (C), one pixel for each peptide, where color code is proportional to the significance of the PC2 parameter over the map; the PC2 parameter load curve (D) takes into account spectral differences between the two peptides. The combination of PC2 mapping and PC2 load curve allows identification of pixels dominated by wild-type or mutated species.

Analytical results

Table 1. Fractional peptide content of M1775 (wild type) and M1775R (mutated). The point mutation (arginine replaces methionine in peptide 1) is underlined.

Number of peptides	Fractional M1775 (wild type) sequence peptides	Composition (%) (error, 8%)	Fractional M1775R (mutated) sequence peptides	Composition (%) (error, 8%)
1	ICCYGPFTNMPTDQLE	11.18	ICCYGPFTNRPTDQLE	6.36
2	APVVTREWVLD	7.85	SDPSEDRAPE	9.92
3	ADALYTNPAQARE	2.56	TSYLPRQDLE	5.91
4	TAANLHAPVILAGTPGTFT HAGTE	14.25	SARVGNIPSSTSALKVPQLK VAE	10.25
5	NLVQRVPKDVFMGVDE	7.30	ASHLPFAQNISRVKE	7.72
6	GAILVVAATDGPMPQTRE	11.76	VYILSKDE	8.76
7	GGDALIPMLKE	9.26	TFNVGSFASGKE	5.76
8	KFMKIISLAPE	11.34	RYLGAKFPGAKRFSLE	7.75
9	VIAHLVNWE	10.22	AAKAKGAMALFGEKYDE	6.98
10	RINKALDFIAE	8.25	GRQGGTLQLFRTE	4.22
11	LRAKNQITLPVILKNE	5.03	KFTALTAELTAE	7.44
12			GGRTVGAGVVAKVLS	6.38
13			RFQADTLARFE	6.15
14			FLKAGGVFTDE	6.57

Thank you all!

Be open to science not only to single discipline